IN-SITU OBSERVATION OF SURFACE AND NEAR-SURFACE MODIFICATION USING SCATTERING OF BALLISTIC PHONONS

Thesis by

Roya Maboudian

Submitted in partial fulfillment of the requirements
for the degree of Doctor of Philosophy

California Institute of Technology
Pasadena, California

1989

(Submitted June 24, 1988)

ACKNOWLEDGEMENTS

Much of this work is the result of a fruitful collaboration between the Low Temperature group and the Basic and Applied Physics group at Caltech. Therefore, I would like to thank all the members of these groups for their help. More specifically, I would like to thank:

David Goodstein, my advisor, for his support and guidance, for staying cool whenever something went wrong in the lab and I thought it was the end of the world and for, despite his busy schedule, always making himself available to talk to;

Tom Tombrello, my second advisor, for his invaluable scientific input and his encouragement whenever I needed some;

Bob Housley for giving me the idea for this experiment, for his friendly personality and for the fun hikes he took me on;

Carlo Carraro for helping me with some of the experiments, for his valuable input in figuring out what the heck the data means and for always being around to talk to;

Nils Asplund for his help in building the apparatus, for his continuous technical support, for his refreshing sense of humor and for the chocolate;

Franco Scaramuzzi for his help in the design of the cryostat and also for the good Italian food he would cook for us;

Mike Pettersen for always having an answer to my questions, for always being very considerate and also for, not so always, putting up with my sense of humor;

Alan Rice for helping me with the beam line, for staying up late to make sure the tandem did not die on me and for just being a nice guy to talk to;

Shouleh Nikzad for her company, specially during the early years of graduate school, for staying up late with me to work on the homework sets and for her kind heart and warm nature;

Mark Lysek, Jim Mercereau, Pete Sercel, Pat Stevens, Don Strayer, Thad Vreeland, Duncan Weathers, Mike Weimer and Fulin Xiong for their help at various stages of this project.

I also thank my family and friends, both in the States and back in Iran, for giving me all the love I could take. Above all, I would like to thank Baba Muktananda and Gurumayi Chidvilasananda for giving me the good fortune to enjoy the good times and to face the not-so-good times.

ABSTRACT

We have investigated the feasibility of phonon-reflection techniques as non-destructive means to probe surface and/or near-surface damage in otherwise highly perfect crystals. A UHV liquid-helium stage, suitable for phonon-reflection measurements, was installed on a beam line of a tandem van de Graaff accelerator which was used to implant MeV ions into the substrate in order to modify the subsurface region *in situ*. Here, we report our investigation on the effects of 1 MeV Ar^+ implantation in Al_2O_3 single crystals by monitoring the reflection of terahertz (THz) phonons (50 Å wavelength) from the implanted region. The results are supported by x-ray rocking measurements and Monte Carlo simulations.

Using a 15 kV ion gun on the same beam line we have also bombarded Al_2O_3 crystals coated with thin films of gold. The effects of a 7.5 keV Ar^+ irradiation on this $Au - Al_2O_3$ system are also discussed in this thesis.

The relevance of this work is discussed in connection to the observations made by other groups and also to our previous work (reported in Appendix 3) on phonon-induced desorption of He atoms as well as the Kapitza anomaly.

TABLE OF CONTENTS

1. INTRODUCTION

For some years, we have investigated problems such as the anomalous low temperature transmission of heat across various interfaces (Taborek and Goodstein 1980) (a problem called the Kapitza anomaly) and also the desorption mechanism of He thin films (Goodstein *et al.* 1985, Sinvani *et al.* 1984, Goodstein 1985), using ballistic phonons generated by heat pulses. A schematic diagram of the experiment relevant to this thesis is depicted in Fig. 1.1a. A thin metallic heater (in our case 500 Å nichrome) is evaporated on one side of a sapphire (Al_2O_3) single crystal. By Joule-heating, thermal phonons are radiated into the substrate. If the crystal has very few impurities (i.e., low phonon-defect scattering) and is at a temperature sufficiently low with respect to the Debye temperature of the solid (i.e., negligible dispersion effects as well as low phonon-phonon interaction), the phonons travel macroscopic distances without being scattered. Sapphire easily satisfies these criteria due to its very high Debye temperature (~ 1000K) (Braginsky *et al.* 1985), low isotopic impurity (0.204% due to ^{18}O), and advanced methods of single-crystalline growth (low impurity concentration). Because of the latter, it is possible to get large crystals which enable us to neglect the wall effects. The ejected phonons traverse the crystal, are reflected from the surface (usually under vacuum), and, after traversing the crystal again, are detected by means of a superconducting Sn bolometer (2000 Å thick). Using very short (30 nsec duration) heat-pulses as well as small heaters and bolometers (0.1 mm^2 area), we achieve time resolution of the order of a few tens of nsec. In this way one is able to resolve various phonon polarizations (1 longitudinal, 2 transverse and up to 6 mode-converted) due to their different paths and group velocities, and thus their arrival times (Fig. 1.1b) at the detector (Taborek and Goodstein 1979). Because of the non-ideality of the surface, some of the phonons are reflected specularly and some diffusely (normally showing up as a long tail superimposed on the specular peaks). Taking advantage of the crystalline anisotropy of sapphire, it has been shown that one can find relative positions for heater and bolometer for which diffusely scattered phonons are preferentially focussed in the direction of the bolometer and detected as a separate broad peak in a plot of signal versus time (Taborek and Goodstein 1980). A typical signal in this orientation is shown in Fig. 1.2. If one introduces liquid helium (LHe) to the outside of the reflecting surface, the diffuse peak is dramatically reduced while the specular peaks remain the same. Briefly, this arises in the following way (A.C. Anderson 1980). Considering the transmission probability (α) of phonons across any *ideal* solid-LHe interface using classical continuum mechanics, the considerably smaller speed of sound, as well as the smaller mass density of LHe compared to any other solid, would yield $\alpha \sim 0.01$ due to a large acoustic impedance mismatch. However, experimentally one observes α's of about 0.5. Based on our experiments as well as other similar experiments, it was realized that there are two transmission components. One, as expected, obeys the acoustic mismatch model (the specular peaks in our experiment). The other is anomalous (the diffuse signal, which disappears when in contact with LHe). It has been demonstrated experimentally that the anomalous component is a consequence of surface defects which, once removed, leave only the expected acoustic-mismatch result and no anomaly (Weber *et al.* 1978, Basso *et al.* 1984).

In addition, it was found that when only a few (~ 3) monolayers of He were introduced onto the reflection surface, the effect was the same as that of bulk He (Long *et al.* 1973, Guo and Maris 1974, Dietsche and Kinder 1975, Taborek and Goodstein 1980). In other words, the signal in Fig. 1.2 looked the same whether LHe or a very thin film of He was adsorbed onto the surface. For the thin film results, one source of this enhanced transmission was attributed to desorption of He atoms. We carried out some experiments to investigate this process (Sinvani *et al.* 1984, Goodstein *et al.* 1985). Some of the results are reported in Appendix 3.

Also, originally it was thought that the Kapitza anomaly happened only for a solid-LHe interface, but later it was shown that a similar process occurs for other systems (e.g., sapphire/solid Ar) as well (Taborek and Goodstein 1981). Several models have been proposed (Shiren 1981, Kinder 1981), but the exact microscopic nature of this process remains unresolved, mainly due to the as yet poor understanding of the exact mechanism of the diffuse scattering at non-ideal surfaces.

It has been shown that the low temperature thermal conductivity measurements in the boundary scattering regime are also sensitive to the nature of phonon reflection (diffuse vs. specular) at surfaces and interfaces (Pohl and Stritzker 1982, Klitsner and Pohl 1984, 1986). Pohl and Stritzker (1982) have reported such measurements on sapphire samples with a variety of surface treatments including ion bombardment in an attempt to study the causes of diffuse phonon scattering at crystal surfaces.

Due to the extreme sensitivity of our phonon-focussed diffuse peak technique, we decided to carry out a similar investigation. However, we wanted to have the capability to alter the surface region in a controlled way and under UHV conditions while simultaneously studying the scattering of phonons from such modifications. Ion beams are particularly suitable for this purpose because one is able to vary the depth at which the damage is introduced by varying their energy and also change the extent of the damage by changing the dose. This way, we hoped not only to gain some insights into the cause(s) of the Kapitza anomaly but also to investigate the potential of the ballistic phonon reflection technique as a surface probe.

This thesis is organized as follows. In Chapter 2, we describe, from a theoretical point of view, propagation, reflection and transmission of phonons across various interfaces of relevance. In Chapter 3, previous experimental investigations concerning the Kapitza anomaly are summarized, leading to the motivation for the present work. In Chapter 4, the design of the experimental apparatus is discussed. In Chapter 5, we present our data for various surface treatments. Then in Chapter 6, the accumulated data are analyzed and compared to those of the previous investigators. Finally in Chapter 7, we summarize our results and end with some concluding remarks and suggestions for further experiments.

2. PHONON BACKGROUND - THEORETICAL

In the experiments reported in this thesis, phonons injected into the sapphire single crystals have very long mean free paths (basically limited by the size of the crystal). The reasons are manifold (Herth and Weiss 1970). First, by cooling the substrate, the interaction between the thermal equilibrium phonons of the crystal and the injected phonons becomes negligible (i.e., low phonon-phonon scattering). Second, in a material like Al_2O_3 with its very large Debye temperature (~ 1000 K) (Braginsky *et al.* 1985), corresponding to the Debye frequency, f_D, of 23 THz, dispersion effects can be ignored when a material like constantan, with a lower Debye temperature (390 K, corresponding to f_D of about 8 THz) is used as a phonon generator. More specifically, it has been shown that dispersion effects in sapphire can practically be neglected for phonons with wave vectors not exceeding 1/2 of the corresponding Brillouin zone vector (Bialas and Stolz 1975). In such instances, phonons close to the zone boundary are not generated and thus one can assume that phonons of a certain polarization radiated in a certain direction have practically the same propagation velocity. Third, at the frequencies involved in these experiments, one can ignore deviations from harmonic approximation. Fourth, sapphire has a very low concentration of isotopic impurities (0.204% ^{18}O instead of ^{16}O) and other foreign impurities yielding low phonon-impurity scattering. As a result of all these, phonons in sapphire can travel macroscopic distances without undergoing much scattering and thus the propagation and reflection of phonons can be treated using the elastic continuum model.

A. PHONON PROPAGATION IN SOLIDS

The laws of propagation of elastic waves in a crystal (Federov 1968, Musgrave 1970) can be derived from the equation of motion:

$$\rho\frac{\partial^2 u_i}{\partial t^2} = \frac{\partial \sigma_{ij}}{\partial x_j} \tag{2.1}$$

where ρ is the mass density, u_i is the i-th component of the displacement, x_j is any convenient orthogonal basis and σ_{ij} is the stress tensor. Summation over repeated indices is understood in this equation and in the following ones. To obtain an equation containing only the displacement vectors, the stress tensor can be written in terms of the strain tensor, γ_{lm}:

$$\sigma_{ij} = c_{ijlm}\gamma_{lm} \tag{2.2}$$

where c_{ijlm} is the tensor of elastic constants and

$$\gamma_{lm} = \frac{1}{2}\left[\frac{\partial u_m}{\partial x_l} + \frac{\partial u_l}{\partial x_m}\right]$$

The elastic tensor has $3^4 = 81$ elements, but crystalline symmetry reduces the number that are independent. For an isotropic crystal, there are two elastic constants, whereas for example, for sapphire there are six. Using Eq.(2.2), we can rewrite Eq.(2.1) as

$$\rho\frac{\partial^2 u_i}{\partial t^2} = c_{ijlm}\frac{\partial^2 u_m}{\partial x_j \partial x_l} \tag{2.3}$$

where we have taken advantage of the symmetry of the elastic tensor in the last two indices. Considering plane monochromatic elastic waves, the displacement may be written as:

$$u_i = u_0 e_i e^{i(\vec{k}\cdot\vec{x} - \omega t)}$$

where u_0 is the amplitude of $\vec{u}$ and $\hat{e}$ is a unit polarization vector. $\vec{k}$ and ω are the wave vector and the frequency respectively. Substituting this into Eq.(2.3) yields

$$(\lambda_{ijlm}k_j k_l - \omega^2\delta_{im})e_m = 0 \tag{2.4a}$$

or

$$(\lambda_{ijlm} n_j n_l - v^2 \delta_{im}) e_m = 0 \tag{2.4b}$$

where $\lambda_{ijlm} = c_{ijlm}/\rho$ and $\vec{k} = (\omega/v)\hat{n}_{\vec{k}}$, $\hat{n}_{\vec{k}}$ being a unit vector and v being the phase velocity of the wave. Equation (2.4b) is an eigenvalue equation with eigenvalues v^2 Hence, v^2 is a root of the characteristic equation

$$\det(\lambda_{ijlm} n_j n_l - v^2 \delta_{im}) = 0 \tag{2.5}$$

This is a cubic equation in v^2 yielding in general three solutions, v_σ, $\sigma = 1, 2, 3$ corresponding to one longitudinal (L) and two transverse modes (T1,T2). Thus, given a direction in the $\vec{k}$-space ($\hat{n}$), by solving Eq.(2.4b) and (2.5), the polarization vectors and the phase velocities corresponding to the three modes can be determined.

In addition to this, the directions along which energy is transmitted are given by the energy flux-density vector, $\vec{P}$:

$$P_i = -\sigma_{ij} \frac{\partial u_j}{\partial t}$$

The time average of this vector may be written in terms of the elastic tensor as:

$$\bar{P}_i = \tfrac{1}{2} \omega c_{ijlm} k_l e_j e_m$$

Dividing this by the time-averaged energy density, $\bar{E}$, one obtains the vector for the velocity of the propagation of the energy or the group velocity vector :

$$s_{i,\sigma} = \frac{\bar{P}_i}{\bar{E}} = \frac{\lambda_{ijlm} e_j e_m n_l}{v_\sigma} \tag{2.6}$$

where σ denotes the wave polarization.

For computing group velocities, the above equation is usually used, whereas for qualitative discussions, we use the following property :

$$s_i = \frac{\partial \omega}{\partial k_i} \tag{2.7}$$

To obtain detailed information about the propagation properties of long-wavelength phonons, the most powerful and widely used technique is the construction of the phonon *constant energy surface* near the origin in $\vec{k}$-space for the three acoustic polarizations ($\sigma = L, T1, T2$). If we construct a surface which has along each wave-normal direction, $\hat{n}$, a distance from the origin equal to $1/v_\sigma(\hat{n})$ where σ denotes the polarization of the phonon, we obtain the *reciprocal phase velocity surface* or as more commonly called the *slowness surface* which has the same shape as the energy surface since:

$$|\vec{k}| = \frac{\omega(\vec{k})}{v_\sigma(\vec{k})} = \frac{constant}{v_\sigma(\hat{n})}$$

However, in a phonon-pulse experiment, what one would like to know is the distribution of phonon intensity, i.e., the normalized phonon energy flux per solid angle (called the *intensity surfaces*) (Roesch and Weiss 1976). To derive an analytic expression for these surfaces, consider the spectral flux in solid angle $d\Omega_{\vec{s}_\sigma(\vec{k})}$ in the spectral range $E(\vec{k})$ and $E(\vec{k}) + dE(\vec{k})$:

$$I(E, \hat{n}_{\vec{s}_\sigma(\vec{k})}) d\Omega_{\vec{s}_\sigma(\vec{k})} dE(\vec{k}) = dN_\sigma(\vec{k}, d^3\vec{k}) s_\sigma(\vec{k}) \hbar\omega \tag{2.8}$$

where $dN_\sigma(\vec{k}, d^3\vec{k})$ is the number of phonons with wave vectors between $\vec{k}$ and $\vec{k} + d^3\vec{k}$ given by :

$$dN_\sigma(\vec{k}, d^3\vec{k}) = D_\sigma(\vec{k}) f_\sigma(E(\vec{k})) d^3\vec{k} \tag{2.9}$$

In this equation, $D_\sigma(\vec{k})$ is the density of states in $\vec{k}$-space which is equal to $V/(2\pi)^3$, where V is the real space volume, $f_\sigma(E(\vec{k}))$ is the distribution function which in thermal equilibrium is given by the Bose-Einstein distribution. Equation (2.9) can be rewritten as:

$$dN_{\sigma}(\vec{k}, d^3\vec{k}) = \frac{V}{(2\pi)^3} f_{\sigma}(E) d^2\vec{k} dk \tag{2.10}$$

The thickness, dk, of the volume element $d^3\vec{k}$ measured along the direction of the group velocity, $s_{\sigma}(\vec{k})$ can be expressed, using Eq.(2.7), as:

$$\vec{s}_{\sigma}(\vec{k}) = \frac{1}{\hbar} \nabla_{\vec{k}} E(\vec{k}) = \frac{1}{\hbar} \frac{dE}{dk} \hat{n}_{s_{\sigma}(\vec{k})}$$

Where $\hat{n}_{s_{\sigma}(\vec{k})}$ is a unit vector along the group velocity vector and thus:

$$dk = \frac{dE}{\hbar s_{\sigma}(\vec{k})}$$

with $s_{\sigma}(\vec{k})$ defined as the magnitude of the group velocity vector. Also, according to the geometrical construction of Fig. 2.1, the area, $d^2\vec{k}$, projected onto the plane perpendicular to dk is given by:

$$d^2\vec{k} = d\Omega_{\vec{k}}\, k^2 \frac{s_{\sigma}(\vec{k})}{v_{\sigma}(\vec{k})}$$

Substituting the last two equations in Eq.(2.10) yields:

$$dN_{\sigma}(\vec{k}, d\vec{k}) = \frac{d^3\vec{r}}{(2\pi)^3} f_{\sigma}(E) \frac{\omega^2}{v^3_{\sigma}(\vec{k})} \frac{dE}{\hbar}$$

where we have also used $\vec{k} = \omega / v_{\sigma}(\vec{k})$. Then Eq.(2.8) can be written as:

$$I(E, \hat{n}_{\vec{s}_{\sigma}(\vec{k})}) = \frac{1}{\hbar} \frac{\omega^2 s_{\sigma}(\vec{k})}{v^3_{\sigma}(\vec{k})} f_{\sigma}(E) \frac{V}{(2\pi)^3} \frac{d\Omega_{\vec{k}}}{d\Omega_{\vec{s}_{\sigma}(\vec{k})}} \tag{2.11}$$

The ratio $d\Omega_{\vec{k}} / d\Omega_{\vec{s}_{\sigma}(\vec{k})}$ is called the focussing factor. In a general case, a wave packet with $\vec{k}$ vectors contained in $d\Omega_{\vec{k}}$ solid angle in $\vec{k}$-space can send energy into a solid angle $d\Omega_{\vec{s}_{\sigma}(\vec{k})}$ in real space. If $d\Omega_{\vec{k}} > d\Omega_{\vec{s}_{\sigma}(\vec{k})}$, the energy is focussed and if

$d\Omega_{\vec{k}} < d\Omega_{\vec{s}_\sigma(\vec{k})}$, the energy is spread over a larger area. It can be shown that the tendency of phonons to group in any direction depends upon the curvature of the *slowness surface* and is given by:

$$\frac{d\Omega_{\vec{k}}}{d\Omega_{\vec{s}_\sigma(\vec{k})}} \equiv \frac{1}{\left| \frac{1}{v_\sigma^3(\vec{k})}\, s_\sigma(\vec{k})\; G_\sigma(\vec{k}) \right|} \qquad (2.12)$$

where G_σ is the Gaussian curvature of the *slowness surface*. We will return to this point later in this chapter.

Because of such considerations, phonons with quite different $\vec{k}$ vectors can contribute to the flux (see Eq.(2.11)) in a chosen $\hat{n}_{\vec{s}}$ direction:

$$I(E,\hat{n}_{\vec{s}_\sigma}) = \frac{\omega^2}{\hbar}\, f_\sigma(E)\, \frac{d^3\vec{r}}{(2\pi)^3} \int_{-1}^{+1}\int_{0}^{2\pi} \frac{s_\sigma(\vec{k})}{v_\sigma^3}\, \frac{d\Omega_{\vec{k}}}{d\Omega_{\vec{s}_\sigma(\vec{k})}}\, \delta(\hat{n}_{\vec{s}} - \hat{n}_{\vec{s}(\vec{k})})\; d(\cos\theta(\vec{k}))\, d\phi(\vec{k})$$

with the definition $\int_{-1}^{+1}\int_{0}^{2\pi} \delta(\hat{n}_{\vec{s}} - \hat{n}_{\vec{s}(\vec{k})})\; d(\cos\theta(\vec{k}))\, d\phi(\vec{k}) = 1$. Normalizing the above thermal phonon intensity to the mean intensity taken over the whole solid angle yields the expression for the *intensity surface* in real space:

$$i_\sigma(\hat{n}_{\vec{s}}) = \frac{1}{1/\bar{v}_\sigma^2} \int_{-1}^{+1}\int_{0}^{2\pi} \frac{s_\sigma(\vec{k})}{v_\sigma^3(\vec{k})}\, \frac{d\Omega_{\vec{k}}}{d\Omega_{\vec{s}_\sigma(\vec{k})}}\, \delta(\hat{n}_{\vec{s}} - \hat{n}_{\vec{s}(\vec{k})})\; d(\cos\theta(\vec{k}))\, d\phi(\vec{k})$$

where

$$\frac{1}{\bar{v}_\sigma^2} = \int_{-1}^{+1}\int_{0}^{2\pi} \frac{s_\sigma(\vec{k})}{v_\sigma^3(\vec{k})}\, \frac{d\Omega_{\vec{k}}}{d\Omega_{\vec{s}_\sigma(\vec{k})}}\; d(\cos\theta(\vec{k}))\, d\phi(\vec{k}).$$

$\bar{v}_\sigma$ corresponds to an isotropic sound velocity which gives the same mean phonon intensity of polarization σ in thermal equilibrium.

Some authors refer to *group velocity surfaces* instead of *intensity surfaces*; these surfaces are defined as the surfaces in real space whose polar vector gives the magnitude of the group velocity as a function of the solid angle. The difference between these and the *intensity surfaces*, however, is only quantitative, since the structure of the singularities is determined in both cases by the Jacobian determinant $d\Omega_{\vec{k}} / d\Omega_{\vec{s}_\sigma(\vec{k})}$, given by Eq.(2.12).

I. Isotropic Medium

An isotropic solid has only two elastic constants. In such a medium and along any wave normal direction, the three orthonormal waves are pure modes. In other words, the polarization of the longitudinal wave is parallel to the wave normal and the two degenerate transverse modes can have any polarization perpendicular to the direction of propagation. This means that the *slowness surfaces*, in this case, are all spherical and that the direction of energy flow coincides with the wave normal direction. In other words, the energy flux is also uniformly distributed, corresponding to $d\Omega_{\vec{k}}/d\Omega_{\vec{s}_\sigma(\vec{k})} = 1$ in Eq.(2.12).

II. Anisotropic Solid

In general, none of the features stated for an isotropic medium occurs in a crystal; none of the orthonormal waves is purely longitudinal or purely transverse and all three waves have different velocities, except along particular symmetry directions. The convention most commonly used to classify the three polarizations is according to their phase velocities: quasi longitudinal (L) with the highest phase velocity, slow transverse (ST) with the lowest phase velocity and fast transverse (FT) with the velocity between the two. The crystal anisotropy leads to complicated propagation patterns, most easily visualizable in the *slowness surfaces* or/and the *intensity surfaces*. Unlike the case of an isotropic medium, these two surfaces do not coincide in this case, since the group velocity is not necessarily along the direction of the wave vector.

Let us consider phonon propagation in sapphire (Bialas and Stolz 1975). This solid crystallizes in the trigonal system, containing two Al_2O_3 molecules, with $\bar{3}m$ (D_{3d}) point group and $R\bar{3}C$ (D_{3d}^6) space group. In other words, the independent symmetry elements of this crystal are the three fold c-axis, the two fold a-axis and the mirror plane perpendicular to the a-axis, containing the c-axis. By convention, the c-axis is taken along the Z-axis and the a-axis is along the X-axis; the Y-axis is defined to make a right handed Cartesian coordinate system and thus it lies in the mirror plane. Sapphire has six independent elastic constants, as given by Farnell (1961).

Even though sapphire is considered the most isotropic of commonly used crystals (e.g., its two transverse speeds of sound differ only by a few percent), as we shall see below, some spectacular effects emerge from its slight anisotropy.

The *slowness surfaces* for the three polarizations are shown in Fig. 2.2 taken from Every *et al.* (1984). The longitudinal sheet of the *slowness surface* is entirely convex and hence there is very little anisotropy associated with the propagation of this phonon polarization. In contrast, the *slowness surfaces* of the two transverse modes are noticeably non-spherical. There are regions where these surfaces are convex (i.e., both of the principal curvatures are positive) and regions where they are concave (with the two principal curvatures being negative). Along the lines that separate these two regions, the Gaussian curvature, which is the product of the two principal curvatures, becomes zero, and in turn the phonon focussing factor, as defined earlier in this chapter, becomes infinite. These lines show up as phonon caustics in the *group velocity surfaces*, Fig. 2.3 (Every *et al.*, 1984). Of course, it should be kept in mind that in any real experiment, the intensities have to be integrated over a finite solid angle which then yields a finite energy flux. In any case, the *group velocity surfaces* clearly show that there is strong anisotropy in phonon propagation even in such an "isotropic" crystal as sapphire.

B. REFLECTION OF PHONONS AT A BOUNDARY

So far we have only considered the propagation of elastic waves in an infinite medium. Here, we shall consider the case when an elastic wave meets the boundary between a solid and vacuum (in part I) and between two solids and a solid and liquid He (in part II).

I. Phonon Reflection at a Solid-Vacuum Interface

In this section we first consider the situation where the impinging phonons find an ideal (flat) surface and are thus specularly reflected (part (a)) and then in part (b), the case of diffuse scattering is considered.

a. specular reflection

The translational invariance along the surface requires that upon reflection, the component of the wave vector parallel to the surface, $\vec{k}_{\|}$, must be conserved (Taborek and Goodstein 1979). What this condition leads to is depicted in Fig. 2.4. Here, cross sections of the *slowness surfaces* are shown for the three polarizations for an arbitrary crystallographic plane. The inner curve is the quasi-longitudinal mode (L) and the other two are the quasi-transverse ones (FT, ST). Given an incident wave vector, $\vec{k}_{inc}$, the intersections of these curves with the lines given by $\vec{k}_{inc,\|}=\vec{k}_{ref,\|}$ yield the permitted solutions for the outgoing waves. As can be seen from the figure, for a longitudinally polarized incident wave, one can always find three outgoing waves corresponding to the three polarizations. This is because the longitudinal mode has the largest phase velocity and thus can be phased-matched to any of the other polarizations. However, in general, this is not the case for the transverse modes. For example, considering the fast transverse mode, for $\theta<\theta_{c,(FT\rightarrow L)}\equiv arctan\ (v_{FT}/v_L)$, there can be three reflected waves, whereas for $\theta>\theta_{c,(FT\rightarrow L)}$ the condition of parallel momentum conservation cannot be satisfied by any longitudinal waves. However, the condition $k_{\|}^2+k_{\perp}^2=k_L^2=\omega^2/v_L^2$ can be satisfied for imaginary values of $k_{\perp}$ corresponding to an evanescent wave with exponentially decreasing amplitude away from the surface (known as a *Rayleigh wave*).

Algebraically, to calculate the reflected modes for a given incident wave, we adopted the following method : choose a wave vector, $\vec{k}_{inc}$ with unit amplitude by convention (this means choosing angles θ, ϕ in polar coordinates); using equations (4b), (5) and (6), calculate the three phase velocities $(\vec{v}_{inc,\sigma})$ as well as the polarization vectors $(\hat{e}_{inc,\sigma})$ and their group velocities $(\vec{s}_{inc,\sigma})$. Take one of these modes, σ_i, and by imposing the $\vec{k}_{inc,\parallel} = \vec{k}_{ref,\parallel}$ conservation condition, solve Eq.(2.4a) for the possible values of $k_{\perp}$. In general, there will be six solutions; the three positive ones correspond to the refracted waves which are not allowed at a vacuum interface. The solutions with negative values of $k_{\perp}$ represent possible reflection processes, $\vec{k}_{ref} = \{\vec{k}_{inc,\parallel}, k_{ref,\perp}\}$. The reflected wave vectors, thus obtained, are renormalized to the unity magnitude and using Eq.(2.4b), once again the phase velocities $(\vec{v}_{ref,\sigma'})$, the polarization vectors $(\hat{e}_{\sigma'})$ and the group velocities $(\vec{s}_{ref,\sigma'})$ are calculated. The same convention, as stated earlier, is used for labeling the various modes. Once the permitted solutions are found, the displacement amplitude of each mode $(u^0_{ref,\sigma'})$ is obtained using the stress-free boundary condition at the surface:

$$\sigma_{ij} \, n_j = 0$$

where $\hat{n}$ is the surface normal and σ_{ij} is the stress tensor defined in Eq.(2.2). By projecting the reflected displacement vector $(\vec{u}_{ref,\sigma'})$ onto the incident displacement vector $(\hat{e}_{inc,\sigma})$ the strength of coupling from one mode $(\sigma_{inc} \equiv \sigma)$ into another $(\sigma_{ref,i} \equiv \sigma_i')$ can be determined.

As related to the experiments reported here, we are interested in the processes that bring the injected phonons into the solid angle of the bolometer after reflection at the surface. Thus, the problem becomes finding a wave vector, $\vec{k}_{inc,\sigma}$, that originates from the heater and after reflection from the surface $(\vec{k}_{ref,\sigma'})$ has a group velocity in the direction of the bolometer. Once such a process is found by trial and error, the strength of such coupling is calculated and if non-zero, the time of flight (TOF) for it is obtained using:

$$TOF = \frac{d}{\vec{s}_{inc,\sigma} \cdot \hat{n}} + \frac{d}{\vec{s}_{ref,\sigma'} \cdot \hat{n}} \tag{2.13}$$

where d is the crystal thickness, $\hat{n}$ is the surface normal and $\vec{s}_{inc,\sigma}$, $\vec{s}_{ref,\sigma'}$ are the group velocities of the incident and reflected waves, respectively. We have written computer programs that, for a given orientation of heater and bolometer, can calculate the times of flight for all the possible reflection processes. In general, one expects up to 9 arrival times corresponding to the three incident phonon polarizations times the three possible mode conversions upon reflection at the surface.

It should be kept in mind that phonon focussing will show itself up in the reflection process as well. Suppose phonons are injected into the crystal from a point source at its center. The total integrated intensity of the specularly reflected phonons of a given polarization arriving at the back of the crystal can reveal sharp features as a consequence of bulk focussing (Northrop and Wolfe 1984). Figure 2.5 shows the results of such measurements for an X-cut sapphire (i.e., X-axis perpendicular to the surface). However, for the work reported here, only Y-cut Al_2O_3 crystals are used for which no appreciable focussing of the *specularly* reflected phonons is expected.

b. diffuse reflection

The exact nature of diffuse scattering from uncharacterized crystal surfaces, such as ours, is not known, but to get an idea of how diffuse reflection will manifest itself in our experiment, let us qualitatively consider the two following situations:

i) isotropic solid: Taborek and Goodstein (1980) have considered the case of an isotropic medium (i.e., $s(\vec{k}) \parallel \vec{k}$) with the following simplifying assumptions. A constant fraction, η, of the radiation incident on the surface is reradiated uniformly into all solid angles and the rest, $(1-\eta)$, is reflected specularly. In addition to this, they assumed that the heater and bolometer are very small and very close together (coincident points). In this case, as shown in Fig. 2.6, the diffuse signal, which is the rate at which phonons are scattered back into the bolometer, is essentially the result of two competing geometrical effects. For long times, the area of the annulus on the reflecting surface that contributes to the signal becomes larger, but the intensity of the beam reaching the bolometer decreases as two powers of the inverse distance. Thus, they showed that for a delta-function heater pulse $Q(t) = Q_0 \delta(t)$, the diffuse signal rises abruptly to its maximum value of $\pi\eta Q_0 v/h^3$ (h being the thickness of the crystal) at $t = 2h/c$, the arrival time of the specularly reflected pulse, and then decays as t^{-5}. In other words, the diffuse scattering contribution shows up as a long-decaying tail superimposed onto the sharp specular peak.

ii) anisotropic solids: The above argument holds reasonably well in an anisotropic medium as well. However, due to crystalline anisotropy, one gets some additional structures (Maris 1971). For example, Fig. 2.7 shows a reflection signal in a Y-cut sapphire crystal. The specular peaks (along with their diffusive tails) are labeled accordingly. However, there is an additional peak which does not coincide with any of the specular peaks. As it turned out, this signal is produced as a consequence of the phonon focussing in this crystal. To understand this, consider the projection of the group velocity surfaces for the two transverse modes (FT and ST) onto the $[1\,\bar{1}\,0\,1]$ crystallographic face of sapphire (i.e., Y-axis normal to the surface). This is represented in Fig. 2.8a. What this shows is that if a heater, positioned at the center of the graph, is pulsed, the injected phonons, though randomly distributed in $\vec{k}$-space, become focussed preferentially along the focussing caustics leading to high intensity regions on the reflection surface. Now, (as similarly done in the previous section) every point on this caustic can be considered as a point source in itself, with a fraction η of its energy radiating diffusely (randomly distributed $\vec{k}$ vectors) and $(1-\eta)$ fraction reflected specularly. The fraction that is diffusely scattered, while traversing the crystal, is refocussed along the phonon caustics. If the bolometer happens to be along one of these high focussing directions, there is an additional channel for the injected phonons to reach the bolometer. To find out what the orientation of the heater and the bolometer should be in order for such a process to occur, we can take advantage of the inversion symmetry of sapphire and treat the problem in the following way: consider two sets of caustics, one corresponding to the heater and the other corresponding to the bolometer and displace them with respect to each other. One can see that if the bolometer and the heater are displaced along the X-axis by a few millimeters, a large part of the high focussing regions for the two devices will overlap giving rise to the additional peak observed in Fig. 2.8b. However, if they are displaced along the Z-axis, there is not as much overlap between the two caustics and thus not a very strong big bump.

II. Phonon Propagation across Two Media

Peter Kapitza, while studying the transport of heat in superfluid ^{4}He, observed a large temperature drop, ΔT, across the interface between his copper heater and the liquid He (Kapitza 1941). Since then, a similar phenomenon has been observed between two solids as well. In this context, one defines a so-called thermal boundary resistance, R_k:

$$R_k \equiv \Delta T \,/\, \dot{Q} \tag{2.14}$$

where $\dot{Q}$ is the heat flux per unit area of the interface. The source of this interfacial resistance is attributed to the reflection and transmission of thermal phonons at the interface. The most widely-known theory to treat this situation is known as the Acoustic Mismatch Theory (AM). Below, in part (a), we briefly review this theory for the case of phonon transport across two solids and in part (b), across a solid and LHe.

a. acoustic mismatch theory for solid-solid interface

The following simplifying assumptions are built into the AM model (Little 1959). The two materials are non-metallic so that heat is carried only by phonons. The temperature is sufficiently low such that only acoustic phonons are present and that there is no dispersion effect. Both solids are perfect so that phonons are scattered only by the interface. The two media are also isotropic in which case the phonon velocity ($\vec{v}(\vec{k})$) is independent of the direction of propagation and is along the direction of the wave vector, $\vec{k}$. The interface is assumed ideal and thus the displacement and the stress are continuous across the interface.

In such system, let us consider a phonon impinging on the interface from material 1, shown schematically in Fig. 2.9 (A.C. Anderson 1980). This gives rise to two reflected and two transmitted waves corresponding to the two possible polarizations. The conservation of parallel momentum leads to an acoustic Snell's law written as:

$$\frac{\sin\theta_0}{v_0} = \frac{\sin\theta_{1L}}{v_{1L}} = \frac{\sin\theta_{1T}}{v_{1T}} = \frac{\sin\theta_{2L}}{v_{2L}} = \frac{\sin\theta_{2T}}{v_{2T}} \tag{2.15}$$

where subscript 1 denotes the reflected wave, 2 the refracted wave, L the longitudinal mode and T the transverse polarization.

As a consequence of this, total internal reflection is possible for a phonon impinging on the interface from the medium with the lower sound velocity. We shall return to this point latter on.

By imposing the boundary condition (i.e., continuity of the normal and the tangential components of stress and displacement), the amplitude, u, of each outgoing wave can be obtained in terms of the incident amplitude, u_0. These in turn can be related to the probability coefficient, $\alpha(\theta)$, for the transmission of the phonon energy across the interface:

$$\alpha_i(\theta) = \frac{\rho_2 v_{2T} u_{2T}^2 \cos\theta_{2T}}{\rho_1 v_{1i} u_{1i}^2 \cos\theta_0} + \frac{\rho_2 v_{2L} u_{2L}^2 \cos\theta_{2L}}{\rho_1 v_{1i} u_{1i}^2 \cos\theta_0} \tag{2.16}$$

for each of the three incident modes, i. In the above equation, ρ_1 is the mass density of the medium 1 and ρ_2 is that of medium 2. Then a summation is performed over the three phonon modes, all the incident directions and all the phonon frequencies to obtain the net heat flux, $\dot{Q}$, carried across the interface. For $\Delta T \left[\equiv \frac{T_2-T_1}{2}\right] \ll T \left[\equiv \frac{T_2+T_1}{2}\right]$ where T_1 and T_2 are the temperatures in media 1 and 2, respectively, one can show that R_k as defined in Eq.(2.14) is given by:

$$R_k = \frac{1}{4b_1 \bar{\alpha}_{12} T^3} \qquad (2.17)$$

where:

$$b_1 = \frac{\pi^2 K_B^4}{120\hbar^3} \sum_i \frac{1}{v_{1i}^2}$$

and

$$\bar{\alpha}_{12} = \frac{\sum_i <\alpha_{1i}>_\theta v_{1i}^{-2}}{\sum_i v_{1i}^{-2}}$$

with i denoting the phonon polarization and $<\alpha_{1i}>_\theta$ being the angle-averaged phonon transmission coefficient for the i-th mode.

Let us look at a more specific situation. Consider the case of sapphire-gold interface. The transmission coefficient as defined by Eq.(2.16) is largely determined by the acoustic impedances $\rho_1 v_1$ and $\rho_2 v_2$ of the two materials. For near normal incidence, Eq.(2.16) reduces to:

$$\alpha_i(0) = \frac{4(\rho_1 v_{1i})(\rho_2 v_{2i})}{(\rho_1 v_{1i} + \rho_2 v_{2i})^2} \qquad (2.18)$$

For Al_2O_3, $\rho \sim 3.986$g/cc, $v_L \sim 11$ km/s and $v_T \sim 6$ km/s, whereas for gold, $\rho \sim 19.3$ g/cc, $v'_L \sim 3.24$ km/s and $v'_T \sim 1.2$ km/s yielding transmission coefficients for near normal incidence of $\alpha_L(0) \sim 0.97$ and $\alpha_T(0) \sim 0.99$.

For phonons impinging on the interface from the gold side, there exist critical angles for transmission corresponding to various incident and transmitted polarizations. Using Eq.(2.15), they are:

$$\theta_{c(L\to L)} = \sin^{-1}\left[\frac{v'_L}{v_L}\right] \sim 17°$$

$$\theta_{c(L\to T)} = \sin^{-1}\left[\frac{v'_L}{v_T}\right] \sim 33°$$

$$\theta_{c(T\to L)} = \sin^{-1}\left[\frac{v'_T}{v_L}\right] \sim 6.3°$$

and:

$$\theta_{c(T\to T)} = \sin^{-1}\left[\frac{v'_T}{v_T}\right] \sim 11.5°.$$

b. acoustic mismatch theory for solid-LHe interface

Some of the assumptions made for the solid-solid interface are modified in this case due to the fact that the liquid cannot support shear waves and hence only longitudinal phonons can exist in the liquid side (Khalatnikov 1965). Also, the boundary condition becomes the continuity of the normal components of stress and displacement. With these, one can derive similar relationships as in equations (15), (16) and (17). Instead, let us make some back of the envelope calculations. (For a more extensive treatment of this problem, we refer the reader to a review article by Wyatt (1980)). The transmission coefficient for near normal incidence, as given by Eq.(2.18), for sapphire-LHe interface is roughly $\alpha(0) \sim 0.01$ where the parameters for LHe are $\rho \sim 0.14$ g/cc and $v' \sim 0.24$ km/s.

Thus, one would expect almost all the phonons impinging on this interface to be reflected.

One can also write the acoustic Snell's law for this situation using Eq.(2.15). The critical angles for transmission of longitudinal and transverse waves are given by:

$$\theta_{cL} = \sin^{-1}\left[\frac{v'}{v_L}\right] \sim 1.25°$$

and:

$$\theta_{cT} = \sin^{-1}\left[\frac{v'}{v_T}\right] \sim 2.3°$$

Thus only phonons from the LHe side within θ_{cL} can generate longitudinal phonons in sapphire and those within θ_{cT} can generate transverse phonons. Conversely, phonons from the solid are transmitted into the LHe within these critical angles.

The AM theory, though it explains why there is a temperature drop across an interface, dramatically fails when its predictions are quantitatively compared to the experimental values. For example, instead of $\alpha \sim 0.01$, the measured values are about 0.5! In other words, the question was no longer why there was a temperature drop across a solid-LHe interface, but why it was so small. Therefore, the question of the Kapitza Anomalous Resistance was changed to that of the Kapitza Anomalous Conductance.

3. PHONON BACKGROUND - EXPERIMENTAL

The motivation for this work came about from an investigation by several groups of the cause(s) of enhanced transmission of heat across a solid and liquid He, a problem known as the Kapitza Anomalous Conductance (Wyatt 1980).

The measurements of heat conduction across a solid-liquid helium (LHe) interface were originally made by passing a heat current ($\dot{Q}$) down a rod which was in vacuum except for the end face, which was in LHe (Challis 1974). A temperature discontinuity (ΔT) was found across the interface and a thermal boundary conductance (Y_K) was defined as:

$$\frac{\dot{Q}}{A} = Y_K \Delta T$$

where A is the area of the interface. ΔT is kept small compared with the ambient temperature and thus the temperature dependence of Y_K can be measured. As discussed in Ch. 2, Sec. B, based on the acoustic mismatch (AM) theory, one expected Y_K to be proportional to T^3 (i.e., it should increase with the equilibrium density of phonons). However, experimentally it was found to depend on higher powers of T. Also, the magnitude of Y_K was always much greater than the predicted value based on the AM theory and thus it was referred to as the anomalous Kapitza conductance. Later, more refined experiments showed that for low phonon frequencies (≤ 1 GHz) the acoustic mismatch theory is obeyed (Keen *et al.* 1965, Sabisky and Anderson 1975). In these experiments, the phonons were generated piezo-electrically where the maximum phonon frequency is limited to a few GHz.

A more powerful technique to probe this process is the direct measurement of the reflection of ballistic phonons from a solid-LHe interface by using the so-called heat pulse technique (Von Gutfeld 1968). The basic principle behind this technique is shown in Fig. 1.1. A pulse of thermal phonons propagates ballistically through a very pure crystal at low temperatures. At the far surface which is either in vacuum or in LHe, a part or all of the phonons are reflected, and after traversing the crystal again, their arrival time is measured. For a typical solid, one expects up to 9 peaks at the detector corresponding to the three incident phonon polarizations times the three possible mode-conversions upon reflection at the surface. However, some of these peaks are too close to each other to be resolved temporally by the detector. With this technique, one is able to extend the frequency range of the phonons to a few THz (at higher frequencies one has to worry about dispersion effects as well as diffusion). For further discussion of the expected behavior, we refer the reader to Ch. 2 and for a more complete description of the experimental setup, to Ch. 4.

Guo and Maris (1972) reported such measurements for the first time on a silicon crystal. They observed a higher transmission coefficient to LHe for transversely polarized phonons than for the longitudinal modes, in contrast to the predictions of the AM theory. Also the transmission coefficient for the transverse mode was found to be the highest for near normal incidence.

A major improvement in the technique was made by using smaller phonon generators and detectors. Due to the lower thermal time constants of their devices, Taborek and Goodstein (1979, 1980) obtained phonon reflection signals for sapphire single crystals with considerably better temporal resolution than ever before. They observed that the specularly reflected phonons remained unaffected by the introduction of LHe on the reflection surface whereas the diffuse contribution, which normally showed up as long decaying tails superimposed on the specular peaks, was almost entirely transmitted to the LHe. Also, by taking advantage of the crystalline anisotropy of sapphire, they were able to find an orientation for the phonon generator and detector such that the diffusely scattered phonons from the vacuum interface were preferentially focussed in the direction of the detector and showed up as a separate peak on the time of flight signal. This possibility was discussed in Ch. 2, Sec. B. They then observed that by introducing LHe to the reflection surface, the diffuse peak was diminished while the specular peaks remained essentially unchanged (Fig. 1.2). In this way, they showed that the Kapitza anomalous conductance was associated with the diffusely scattered portion of the thermal energy and that to understand the anomaly, one had to understand the causes of the diffuse scattering of phonons. *The specular reflection is a consequence of the translational invariance of the interface and thus the cause of the diffuse scattering must lie in whatever spoils this invariance.*

In addition to the above observation, Taborek and Goodstein (1981) repeated the above measurements for other noble gases (Ar, Ne, etc.) and observed the same behavior (i.e., transmission of the diffusely scattered phonons to the other medium). This way, they showed that the Kapitza anomaly was not a peculiar property of the helium system.

The reflection of phonons was also studied by several groups as a function of He film thickness (Long *et al.* 1973, Guo and Maris 1974, Dietsche and Kinder 1975, Sinvani *et al.* 1984, Goodstein *et al.* 1985, Goodstein 1985). It was observed that the anomalous transmission to helium saturates by the time only a few (~3) monolayers of helium were adsorbed on the reflection surface. For the thin film results, one possible mechanism of the enhanced heat transmission was attributed to the desorption of He atoms. Helium, due to its light mass, has a low binding energy ($E_B \sim 50$ K) to the surface and thus the phonon spectrum, generated in these measurements (corresponding to a Planck distribution with a characteristic temperature of 20 K), has in its tail phonons with enough energy ($\hbar\omega > E_B$) to excite an adsorbed He atom to the continuum. Also, He has an appreciable heat capacity at low temperatures and thus the impinging phonons can raise the temperature of the film leading to some thermal desorption. Some experiments concerning this issue were carried out in our laboratory (Sinvani *et al.* 1984, Goodstein *et al.* 1985); we refer the reader to Appendix 3 for the results.

Weber *et al.* (1978) and Basso *et al.* (1984) showed in two decisive experiments that the Kapitza anomaly was associated with the non-ideality of the interface. In one experiment, the surface of a LiF crystal was cleaved *in situ* under UHV conditions. In this case, the reflection signal from the LHe interface was identical to that of vacuum (i.e., no anomaly). In other series of experiments, the surface of Si was laser annealed under UHV conditions and, after this, again reflection of phonons obeyed the acoustic mismatch theory. Then, a very thin layer (a monolayer) of water or gold was evaporated onto the annealed surface and with this, the anomaly returned (Koester *et al.* 1986, Basso *et al.* 1986).

Many models have been proposed to explain the anomaly. Perhaps, the most obvious one is to consider a rough solid-LHe interface (Shiren 1981). Let the ideal interface be located at $z = z_0$; then the rough surface can be described by superimposing a small amplitude corrugation onto the ideal flat surface:

$$z(x,y) = z_0 + \zeta(x,y).$$

First order perturbation calculations lead to a scattering amplitude for the phonons which is proportional to the spectral density of surface roughness, $G(K_{\parallel})$, evaluated at $\vec{k}_{\parallel} = \vec{k}_{scatt,\parallel} - \vec{k}_{inc,\parallel}$, where $\vec{k}_{inc}$ denotes the wavevector of the incident wave and $\vec{k}_{scatt}$ that of the scattered wave. A flat surface has spectral density of roughness $G(k_{\parallel}) = \delta(k_{\parallel})$, thus leading to conservation of parallel momentum, that is, to the AM theory. Shiren carried out these calculations using an exponentially decaying roughness correlation function:

$$R(x,y) \equiv <\zeta(0,0)\zeta(x,y)> = <\zeta_0^2> e^{-\sqrt{x^2+y^2}/l}$$

where l is the roughness correlation length. Then, by adjusting the parameters ζ_0 and l, he was able to fit remarkably well the Kapitza resistance data for a $Cu-{}^4He$ and $Cu-{}^3He$ interface over a wide range of temperatures and pressures. While his description of the surface roughness is arbitrary, what makes the theory appealing is that in principle, if one could experimentally determine the surface profile by some other means, there would be no free parameters in the calculation of the Kapitza resistance.

Another proposed model is that of localized surface excitations (Kinder 1981). Disordered *normal* (i.e., non ideal) surfaces are assumed to have localized defects that can form a broad distribution of low lying excitations. Phonons can couple to these excitations through the phonon strain field which perturbs the potential of the localized states. This is analogous to the two-level-system (TLS) model proposed to explain the low temperature anomalies observed in glasses (P.W. Anderson *et al.* 1972). The basic idea is that the phonons from the solid side are absorbed by these so-called two level systems. If the reflection surface is under vacuum, the excited states can only relax by phonon reemission into the solid. However, in the presence of LHe, phonons are preferentially radiated into LHe. This is because He has a much lower sound velocity and thus a much higher density of states than any solid. What these two level systems are is not specified. Also, though these localized centers may be associated with the surface roughness, this does not have to be the case. For instance, subsurface damage can lead to this behavior as well.

Despite both the experimental and the theoretical progress in the topic, the origin of the diffuse phonon scattering and thus the Kapitza anomaly is still not understood. Whether it is merely due to surface roughness or it is connected with some localized defects (TLS) (or both or neither) needs more systematic investigations.

Another technique that has been shown to be very sensitive to the condition of the surface is the measurement of the low temperature thermal conductivity (Pohl and Stritzker 1982, Klitsner and Pohl 1984, 1986). In this case, the crystal is normally in the shape of a rod. At one end, a known amount of heat is injected into the rod while the other end is thermally anchored (e.g., by being in contact with LHe). Several thermometers are placed at various places on the walls such that the temperature profile and, in turn, the thermal conductivity can be measured. As stated in Ch. 2, at temperatures low with respect to the Debye temperature of a solid, the phonon mean free path becomes macroscopically large and is basically limited by the size of the sample. In this boundary scattering regime, the injected phonons hit the walls of the sample many times before they reach the thermometer and thus the effect of the surface quality on the phonons is amplified at each traversal. The thermal conductivity is given by:

$$K = c\, l\, v$$

where c is the specific heat, l is the phonon mean free path and v is the speed of sound. At low temperatures, where l is limited by the size of the sample, the thermal conductivity becomes proportional to the specific heat and thus it has a T^3 temperature dependence. This is called the Casimir limit. In this derivation, it is assumed that the phonons are thermalized by colliding with the surface (i.e., the spectral distribution of the scattered phonons is characteristic of the temperature of the surface element by which they are scattered). This is the case for a rough surface whereas, for a smooth surface, the phonons are reflected specularly yielding a longer effective mean free path and thus a larger thermal conductivity.

To address the question of whether the diffuse scattering arises by surface roughness or by damaged layers underneath the surface, Pohl and Strizker (1982) chose ion beams to modify the surface and near-surface regions and then investigated the effect by low temperature thermal conductivity measurements. Ion beams offer the advantage that by changing their energy, the depth at which the damage is introduced can be varied and by changing the dose, the extent of the modification can be monitored. In one case, 350 keV Xe^+ ions (at a dose of $5\text{x}10^{15}$ ions/cm^2) were implanted in a sapphire single crystal with smooth walls at room temperature. They estimated the depth of the damaged region to be about 500 $\text{Å} \pm 150\,\text{Å}$. With this treatment, they claimed that without roughening the surface, they had introduced a thin disordered layer underneath the surface. They, then, observed that the thermal conductivity of the sample in the temperature range of 0.2 K to 2.0 K was reduced to that of a sandblasted sapphire rod (i.e., roughened walls). Therefore, they concluded that they had shown for the first time that the diffuse scattering can be caused by disordering a thin layer near the surface.

They also studied the effect of a thin gold film (100 Å) deposited on a virgin sapphire crystal. It was found that this film similarly caused enhancement of diffuse scattering (as shown by reduction in thermal conductivity). However, the effect was not as strong as in the ion implantation case. Then the gold covered sample was irradiated by 80 keV Xe^+ ions ($5x10^{14}$ ions/cm^2). In this case, the penetration depth of the ions was estimated to be about 100 Å and thus very few of them reached the sapphire surface (i.e., the damage was largely confined to the gold film). With this treatment, they observed further reduction in the thermal conductivity resembling the results of the 350 keV Xe^+ implantation as well as the sandblasted crystal (in the 0.2 K to 2.0 K temperature range).

However, the above measurements had several draw-backs. In the temperature range where the experiments were carried out, the phonon wavelengths were between 1000 Å and 1 μ and thus it was very difficult to distinguish unambiguously between surface and near surface modifications. This is very important in view of the fact that the beam energies used in their experiments could have potentially led to some surface modifications. When bombarding the crystal with the 350 keV Xe^+ beam, the authors reported that they had to cover the surface (see Ch. 4, Sec. D) with a thin gold film and after the ion bombardment, they noted some sputtering of the gold film. Therefore, the effect of the ion beam was not just to introduce a disorder layer underneath the surface, but also to alter the surface characteristics. As a consequence, the change in the thermal conductivity could not unambiguously be attributed to the damage region inside the target. In addition, the modifications were not done *in situ* and under UHV conditions. Therefore, it was not clear whether the observations made were due to the ion beam modifications or due to the adsorbates condensed on the surface while transferring the crystal to the cryostat. All these factors made their conclusions ambiguous.

The approach we took was to build a UHV cryostat suitable for phonon reflection measurements such that it could be mounted on a tandem van de Graaff accelerator along with a keV sputtering setup with two objections in mind; first was to gain some insights into the Kapitza effect. Second was, given the extreme sensitivity of our phonon-focussed diffuse peak, to investigate the potentials of this technique as a surface probe.

With this apparatus, the ion beams with energies ranging from a few keV to a few MeV can be obtained to modify the crystal *in situ*. In the low energy (keV) case, one mainly alters the surface characteristics (by sputtering) whereas using the higher energy (MeV) beams, the damage introduced is inside the material, leaving the surface essentially unchanged. Therefore, one is more decisively able to separate out the near surface damage from surface damage and simultaneously investigate the effect on the reflection of the phonons, using our sensitive phonon-focussed peak as the probe. Also, the phonon spectrum, used in phonon reflection experiments, is Planck distribution with the frequency at its maximum of about 1 THz, corresponding to a wavelength of 50 Å for transverse polarization and 100 Å for longitudinal mode. This is at least an order of magnitude smaller than the ones used in the thermal conductivity measurements of Pohl and Stritzker (1982) leading in our case to a better resolution of the ion beam modification.

4. EXPERIMENTAL SETUP

A. UHV CHAMBER

Since the main objective of the experiment was to modify the reflection surface *in situ* (by ion beams) and simultaneously study the effect on the reflection of phonons, it was essential to have a UHV apparatus. With the base pressure of 10^{-10} Torr, the monolayer readsorption time is about 2½ hours, long enough to carry out our measurements after any modification. As far as the design was concerned, what this meant was that only materials with very low vapor pressures could be used in the construction (Espe 1957). This limited us to mainly using stainless steel, copper, aluminum and teflon, and in addition all the oxidizable surfaces had to be gold- plated.

I. Cryostat

A schematic diagram of the design is presented in Fig. 4.1. The liquid helium (LHe) dewar is suspended from the top plate. To reduce the heat input to the dewar due to room-temperature radiation (White 1979), the cryostat is surrounded by a liquid nitrogen (LN_2) reservoir in conjunction with a LN_2 radiation shield (the nitrogen tank holds about 5 liters of LN_2 and lasts for about 15 hours corresponding to 15 watts of heat input). The cryostat holds about 2 liters of LHe and lasts for 4 hours corresponding to 350 mW of heat input. The main source of this loss is the thermal conduction from room temperature along the stainless steel tubing used to hold the dewar. In a more conventional cryostat, the top of the LHe dewar is thermally anchored to the LN_2 reservoir to reduce this loss. However, in our case, as it turned out, with the LN_2 dewar cold, the base pressure is reduced by more than an order magnitude by cryopumping. If the LHe bath is anchored to the LN_2 pot and thus cooled by the LN_2 dewar, the crystal, being in contact in the former, would get dirtier, by acting as a cryopumping surface. Thus we decided to sacrifice running time for a cleaner substrate. The cryopumping ability is rather essential in this system because, due to our fragile phonon generators and detectors, we are unable to bake the chamber, which is vital for UHV.

To facilitate the transfer of LHe, a guiding tube is inserted in the reservoir as shown in Fig. 4.1. This way, the transfer tube sits on top of this tube and thus LHe is transferred directly in the lower compartment where the crystal sits. This is a crucial step in our design. The upper part of the LHe chamber is made of stainless steel (easier to machine) and is connected, via a ¼″ stainless tubing, to the lower part of the reservoir (also made of stainless steel). Due to the poor thermal conductivity of stainless steel, the upper and lower parts are thermally isolated and thus, without the guiding tube (i.e., with the LHe transfer tube suspended in the upper chamber), it is very difficult to collect any LHe.

II. Crystal

The crystal is mounted, using indium o-rings, on an oxygen-free high-conductivity (OFHC) copper block, which, in turn, is in direct contact with the LHe bath. In the original design, there were holes on this copper block which would allow the crystal to be also in direct contact with the bath, as is shown in Fig. 4.2a. However, due to sizable difference in thermal contraction of Cu and Al_2O_3, we encountered many low temperature leaks at this joint. Thus we modified the design as shown in Fig. 4.2b. This way, all the joints which have to be leak-tight are between similar materials, sealed by In o-rings. This way, one can leak check the cryostat and as the last step mount the crystal, thus keeping it as clean as possible. Also when changing crystals, there is no need to break any leak-tight joints. Of course, with this design we have to cool the bath further to get to the operating temperature of our superconducting bolometers as will be discussed later; but this did not introduce any difficulties.

The sapphire crystals used in the experiments reported in this thesis are all Y-cut with the Z (3-fold symmetry)-axis and the X (2-fold)-symmetry axis in the plane of the surface (for further details, see Ch. 2). Previous investigators (Taborek and Goodstein 1979 and 1980) had used mechanically polished Al_2O_3 crystals obtained from the Union

Carbide Corporation where Czrolski's growth technique is used. To obtain a better quality surface, we purchased some premium quality (HEMEX) crystals from the Crystal System Inc., where heat exchanger growth technique is implemented and also where it is possible to get chemi-mechanically polished surfaces. In the mechanical polishing technique, loose abrasive particles of alumina, silicon carbide, or diamond (typically less than $3\mu m$ in diameter) are used to polish the crystal. The material is removed with successively smaller abrasive particles. In each step, the damage introduced by the previously used larger-size abrasive must be completely removed. The subsurface damage remaining after the last mechanically polishing step can be reduced by polishing with colloidal silica in alkaline aqueous solution and thus with this technique (chemi-mechanical polishing), the subsurface damage is expected to be confined to a much thinner region (about 10Å) than in the case of purely mechanical polishing. However, the reflection signal from these crystals was considerably weaker, leading us to believe that the bulk crystals are of poorer quality than the ones grown by Union Carbide Corp. (at least as far as the propagation of THz phonons is concerned). This may be connected with the higher concentration of F^+ centers in the crystals grown by Crystal System Inc. as reported by Wei and Smith (1972). Therefore, the crystals used for ion beam experiments have the following characteristics. They are grown by Union Carbide Corp. but are chemi-mechanically polished by Crystal System Inc.

III. Pumping

Once everything is mounted on the top plate and the electrical connections to the devices are made and checked, the plate is inserted on top of the chamber permanently located on the tandem van de Graaff accelerator shown in Fig. 4.3. The Au-sealed valve between the accelerator and the chamber allows us to work independently on either side. To pump down the chamber, we first use the two sorption pumps in series to get the pressure in the micron range. Then we use a turbo-molecular pump to get to the region of 10^{-4} Torr or less. The final step is to use a 60 l/s ion pump which allows us to reach easily 10^{-7} Torr range. Due to our fragile bolometers, heaters and In o-rings, we are unable to bake this setup. Instead, we take advantage of cryopumping capabilities of our cold surfaces. By transferring LN_2, the pressure is reduced to 10^{-8} Torr or better while the crystal is maintained at about 300 K. Then to precool the LHe dewar, LN_2 is poured in it and once its temperature reaches 77 K, we siphon out the remaining LN_2 and transfer LHe. Since our operating temperature is about 3.7 K, the superconducting transition temperature of Sn (0.5 K below the condensation temperature of LHe at atmospheric pressure), we need to pump on the He bath. A schematic diagram of the pumping station is shown in Fig. 4.4. Using the vacuum regulator valve, we are able to thermoregulate the bath to about 1 mK, sufficient for our applications. Once at 3.7 K, the pressure in the vacuum space is better than 10^{-10} Torr, as read on the ion pump current meter.

B. DEVICES

Based on our calculations of the time-of-flight of phonons reflected from the far side of a 1 cm-thick Al_2O_3 crystal, we need temporal resolution of the order of few tens of nsec in order to be able to resolve different phonon polarizations. The time resolution in detecting the arrival of a pulse of phonons depends on the width of the electrical input pulse (30 nsec minimum), the resolution of the electronic circuitry (10 nsec) and the thermal relaxation times of heaters and bolometers. The last factor can be made of the order of the other times (10 nsec) by making the devices small (0.1 mm^2 area).

I. Phonon Generators

The phonon generators are thin metallic heaters. They are made of constantan or nichrome, 500 Å thick by 0.25x0.35 mm^2. We tried several methods of fabricating these devices, but the following technique seemed to be the best, the criteria being to keep the surface as clean as possible before the evaporation and to get several heaters made as fast as possible.

After finding out what geometry is desirable, the mask shown in Fig. 4.5c is made (out of brass) which fits in the crystal holder located in the evaporation bell jar. When it is time for evaporation, the crystal is cleaned by placing it in a hot (200°C) solution of phosphoric acid for about 20 min (Brewer *et al.* 1980). Then it is thoroughly washed with deionized water and rinsed with acetone and ethanol. After the crystal is washed and its cleanliness is inspected under an optical microscope, it is placed on top of the mask and aligned properly with it and then both are put in a diffusion-pumped bell jar. Once at 10^{-6} Torr, we evaporate a nichrome film whose thickness is monitored using a standard quartz crystal (Sloan monitor). After depositing 500 Å, we evaporate 2000 Å of Cu on top of the nichrome. Then the crystal is taken out of the bell jar and a 1μ-thick film of photoresist is applied onto it in a dark room. Then using an optical microscope, the heater pattern (shown in Fig. 4.6a) is exposed and developed (i.e., the photoresist is removed from the region where the heater is to be). Then using $FeCl_3$ solution, the copper is etched away from the developed region without appreciably affecting the nichrome. The electrical contacts are made using pressed indium contacts on the copper flaps. By adjusting the length of the nichrome film, we are able to trim the resistance to $50 \pm 1\ \Omega$ and thus match it to the characteristic impedance of our transmission lines and our pulse generator setup, as will be discussed later in more detail. With this technique, we are able to make 18 devices in a 4 mm^2 area.

To calculate the response time of the heater, consider a step function of voltage across the heater causing power dissipation at a rate W (in Watts/area). The temperature of the heater, T_h, as a function of time, is determined by the conservation of energy:

$$W = \rho\, d\, c\, dT_h/dt + \xi (T_h^4 - T_0^4) \qquad (4.1)$$

where the first term corresponds to the power used in raising the temperature of the heater (c being the heat capacity of the film per unit mass and d is the film thickness) and the second term takes into account the power gone into phonon radiation (ξ being the effective Stephan-Boltzmann constant for the phonons and T_0 the bath temperature). At steady state, the heater temperature is

$$T_s = (W/\xi + T_0^4)^{1/4} \tag{4.2}$$

For 2 W input power and $\xi = 1.47\text{x}10^{-5}$ W/ K^4, we find that the heater temperature, being initially at $T_0 \sim 3.7$ K, is raised to 19 K. Using Eq.(4.1), the initial temperature rise, when T_h is very close to T_0, is roughly $W/c(T_0) \sim 5\text{x}10^{11}$ K/sec where $c \sim 10^{-4}$ J/gK for nichrome at T_0. Here, we have used the bulk density of nichrome, 8.2 g/cc and the heater dimensions of 0.1 mm^2 x 500Å. As T_h approaches T_s, Eq.(4.1) can be linearized yielding an exponential approach to T_s with time constant $\tau = R_k(T_s)c(T_s)$ where R_k (the Kapitza Resistance between the heater and the crystal) is $\sim 1/4\xi T_s^3$. This gives $\tau \sim 10$ nsec. When the pulse is switched off, Eq.(4.1) reduces to:

$$c\ dT_h/dt = -\xi(T_h^4 - T_0^4) \tag{4.3}$$

The time scale for the initial cool-down (for $T_s \gg T_0$) is given by $R_k(T_s)\,c\,(T_s)/4$ and as T_h approaches T_0, there will be an exponential behavior with $\tau \sim R_k(T_0)\,c\,(T_0) \sim 10$ nsec. Thus we see that the time taken by the heater to reach the steady state is a few tens of nsec, comparable to the other time constants involved in the measurements and sufficient to resolve various phonon polarizations. In an ideal situation, the heater produces a Bose-Einstein distribution of phonons whose maximum is at 19 K corresponding to 1 THz. This means 100 Å wavelength for longitudinal and 50 Å for transverse modes. It should be kept in mind that in the above statement it is assumed that the film is completely thermalized before radiating into the crystal. Though roughly a good approximation, several authors have questioned this point (Perrin and Budd 1972). The main argument is twofold. In one case, since phonon-phonon interaction is inversely proportional to the frequency, the low frequency phonons escape the film before they get a chance to thermalize. On the other hand, the high frequency phonons should be more sensitive to the detailed structure of the heater/substrate interface. However, in our temperature range, grey-body (emissivity, ξ, less than 1) radiation is not a bad assumption (Herth and Weiss 1970).

II. Phonon Detectors

Our detectors are superconducting tin bolometers. The principle behind their operation is very simple. Figure 4.7 shows a plot of resistance vs. temperature for a typical bolometer. Now, if the ambient temperature is adjusted such that the bolometer is in the middle of its superconducting transition temperature range, a change in the temperature ΔT (due to the impinging phonons, say) is reflected in a change in resistance; this in turn is detected as a voltage increase across the device by passing a biasing current through it. Let us briefly consider the response of a bolometer to a step-like heat input for $t > 0$ (Maul and Strandberg 1969). The change in voltage would then be given by:

$$\Delta v = \Delta(iR) = i\,\Delta R + R\,\Delta i \tag{4.4}$$

where the second term is non-zero due to the finite load impedance. In the above equation, the resistance, R, and in turn the biasing point, is a function of temperature, biasing current and magnetic field :

$$\Delta R = \alpha R\,\Delta T + \beta R\,\Delta i + \gamma R\,\Delta H \tag{4.5}$$

where:

$$\alpha = 1/R\,\partial R/\partial T,\quad \beta = 1/R\,\partial R/\partial i,\text{and}\quad \gamma = 1/R\,\partial R/\partial H$$

It can be seen that the sensitivity of the bolometer can be optimized by making $\partial R/\partial T$ and therefore the normal resistance as high as possible by making the device either longer or thinner. In the former case, the trade-off is an increase in the thermal time constant as well as the spatial and temporal resolution of the device. The latter will be addressed later in this section. However within our capabilities, the solution we chose was to use a serpentine-shaped bolometer depicted in Fig. 4.6b. The dimensions are 20 μ x 2.5 mm x 2000 Å yielding a room temperature resistance of about 200 Ω and LHe resistance of about 20 Ω. A typical biasing current was ~100 μA and in the experiments carried out on the tandem van de Graaff beam line, no magnetic field was used. As done for the heater, we can similarly write down the equations of conservation of energy for the bolometer, but instead we refer the reader for a more extensive treatment of this problem to the work by Axan (1984). However it must be stated that the thermal time constant of these bolometers is about a few tens of nsecs, comparable to other characteristic times in this system.

The way these devices are fabricated is worth discussing here. As for the heaters, there are two main criteria. One is to have the substrate as clean as possible before evaporating the films. The other is to be able to make as many devices as possible on the surface so that we can do several experiments on various parts of the crystal without having to go through the time consuming process of device fabrication.

Previously, the bolometers were made in the following way. After washing the substrate, the crystal was covered with a thin coating of a positive photo-resist (Shipley 350-J). To get a good pattern with sharp edges, the photoresist needed to be baked at 100°C for about half an hour in a convection oven and then soaked in a solution of chlorobenzene for roughly 20 minutes. Using the mask-fabrication facilities in the Electrical Engineering Department, we had made two bolometer masks; one was a positive mask meaning that the whole mask was black except the snake pattern of Fig. 4.6b. The other mask was the opposite. The photoresist covered crystal was then placed under an optical microscope and using the positive mask, we would expose and then develop the bolometer pattern on the photoresist. What this meant was that, at that stage, the whole surface was still covered with the photo-resist except where the bolometer was to be placed. Then the crystal would be placed in an evaporation bell jar and once the pressure was in the 10^{-6} range, we would evaporate 2000 Å of Sn. Then, we would take the crystal out of the bell jar and immerse it in acetone. What this would do was to dissolve the photoresist and along with it the Sn film on top of it, except, of course, where there was no photoresist (i.e., where the bolometer was to be). Then the bolometer would be inspected under the microscope and if it looked reasonably good, two indium dots would be pressed to its two ends which would be used to make electrical connections to the device. There were many serious draw-backs to this technique; the most serious one was the fact that after cleaning the substrate we would put a film of photoresist on it (i.e., making it dirty again). Also, even after the developing step, there would be residual photoresist left on the surface that would lead to bolometers with broken arms (i.e., an open circuit). Because of these and some other not well understood problems, the success rate for making working bolometers was very low and thus we decided to modify the procedure. After months of hard work, we arrived at the following method which worked very well.

After figuring out where the bolometers are to be with respect to the crystal orientation and the heaters, a mask similar to that for the heaters (Fig. 4.5b) is machined. Then after cleaning the crystal as well as possible, we align it with the mask and then place it in the evaporation bell jar. Once the pressure is in the 10^{-6} Torr range, the Mo boat, containing the Sn shots, is outgassed and once the pressure is back to its original value, Sn is evaporated. We found out that it is very important to flash evaporate the Sn because, otherwise, the film comes out grainy looking (i.e., not a smooth film). Then the crystal is taken out of the bell jar and the Sn film is inspected under the microscope. The next step is to cover the surface with photoresist and treat it in the same way as described earlier in this section. Next the evaporated Sn strips are exposed to the negative bolometer pattern and developed. Then using a dilute mixture of HCl, HNO_3 and H_2O_2 in ethylene glycol, the pattern is etched away, leaving behind the snake-patterned bolometer. Next, using acetone, the photo-resist is washed away. At this stage, indium dots are immediately pressed onto the two ends of the bolometer as stated earlier. We would like to mention that we have had problems with this kind of contacts. If there is a long delay between the evaporation and making of the contacts, due to the oxidation of the film, the contacts become electrically noisy. In addition to this, another issue manifested itself in one of our attempts to make more sensitive bolometers by making them thinner. A few days after making indium contacts to several 500 Å thick bolometers, we noticed that their resistances had changed from a kΩ to several MΩ! After investigating them (see the SEM pictures in Fig. 4.8), it was realized that indium diffuses into Sn and vice versa leading to thinning of the Sn film around the indium dots and a huge resistance. This problem presumably also exists for the 2000 Å bolometers as well, but it happens on a longer time scale. Therefore, we decided to go back to using the thicker bolometers and also to use 50-50 In-Sn alloy for the contacts. In any case, with this technique we are able to make 18 bolometers in a 4 cm^2 area where there are already 15 heaters.

C. ELECTRONICS

After the devices are made, we connect to them, via the pressed indium dots, two pairs of twisted copper wire (40 gauge) as shown in Fig. 4.6a. They are in turn soldered to the 50 Ω miniature coaxial cables whose inner conductors are made of copper-clad-steel and outer conductor out of stainless steel. Copper-clad-steel is a good compromise between plain copper (low attenuation of the signal but high thermal loss) and plain steel (low thermal loss but high attenuation). The cables are run along the LHe and LN_2 outer parts for some thermal anchoring. To bring the cables out of the vacuum chamber, we use UHV feedthroughs with 50 Ω characteristic impedance, which are welded to the top plate. The mating connectors between our miniature size cables and these feedthroughs are home-made. When out of the chamber, to make sure that different pieces are well matched to each other, a time domain reflectometer (TDR) was connected to the device. Basically, TDR, with 50 Ω input impedance, puts out a step function with very short rise time (a few nsec) which propagates down the cable. If everything is 50 Ω, the wave doesn't come back. Otherwise, there will be a reflected step from whose arrival time at the reflectometer, the position of the the mismatch can be figured out and from its sign one can find out whether it is inductive or capacitive coupling, etc.. Using this, our heater circuitry is checked and normally is very well matched, and so is the bolometer line, except that the resistance of the bolometer is $\simeq 200\Omega$ at room temperature. Thus we get some reflection there.

A schematic diagram of the electronic instrumentation is shown in Fig. 4.9. A 50 Ω pulse generator produces rectangular pulses of 10 V maximum amplitude across the heater with 5 nsec rise time and a variable width $t_p \geq 30$ nsec. It also provides a synchronous reference signal *prior* to the leading edge of the pulse which in turn is used to trigger the data-acquisition electronics and also an oscilloscope. The heater pulses can be attenuated using an attenuator, if so desired. The rising and falling edges of the heater pulse create inductive spikes in the bolometer circuitry which are used as fiducial timing marks for the ejection of the phonons to the crystal. The necessary bias current for the bolometer is provided by a voltage source in series with a large resistor (normally 10 V with 100 kΩ yielding 100 μA biasing current). The dc offset voltage produced by this current is eliminated using a 8.5 μF capacitor which combined with the 50 Ω input impedance of the preamplifier forms a high-pass filter with a time constant of 400 μsec and 3 db point at 380 Hz. This allows the signals from the bolometer, lasting for $\simeq 10\mu$sec to be recovered with minimal distortion. The preamplifier has a rise time of 5 nsec (bandwidth $\simeq$ 70 MHz) and is normally set for x100 magnification. The output of the preamplifier goes to a Tektronix oscilloscope (with 1 nsec time resolution) such that we can visually inspect the signal while adjusting various parameter (such as the bath temperature). Also the preamplifier output goes to a box-car integrator for signal averaging. The output of the box-car is recorded on a X-Y recorder. The minimum window of the boxcar is 5 nsec which is sufficient for resolving the signal. For a typical signal, with a repetition rate of 100 kHz for heater pulses, it takes about 5 minutes to acquire the signal, corresponding to a signal to noise improvement of 60.

D. BEAM LINE

I. Tandem van de Graaff

The 1 MeV Ar^+ beam is obtained from the 1.5 MeV JN van de Graaff (Fig. 4.10). The positive beam is extracted from the RF oscillator source of the JN, run through the tandem and then energy and charge selected using an Alpha Scientific, Inc. Model 3193 gaussmeter at the 90°-bending magnet downstream of the high energy end of the tandem. Energy selection is reported to be good to a few keV. After energy selection, the beam is deflected by a switching magnet into a diffusion-pumped beam line with a base pressure of approximately $2x10^{-7}$ Torr. The beam line is equipped with a magnetic quadrupole for focusing and magnetic deflectors for steering the beam. Finally via an in-line LN_2 cold trap, the beam enters the experimental chamber. The cold trap enables us to maintain better than two orders of magnitude pressure difference between the chamber (10^{-9}Torr or better) and the beam line ($\geq 10^{-7}$ Torr).

Even though there are several viewing ports along the beam line, in order to check the beam (its alignment, uniformity, etc.) right before it hits the crystal we put a magnetically operated shutter right in front of the crystal (Fig. 4.1). When the shutter is in normal position (closed), the beam intercepts a 1 cm-diameter quartz crystal (covered with a film of Au to avoid charging problems). The beam causes the quartz to fluoresce and we can see the beam spot using the mirror (shown in Fig. 4.3) and make the required adjustments. When the beam was ready, by applying a magnetic field, the shutter is opened and the beam strikes the crystal. The beam spot is 6 mm-diameter maximum, sufficient for our purposes.

Current integration is achieved by evaporating a film of gold (750 Å) covering about 1½″ in diameter of the surface. Using pressed indium dots, 40-gauge copper wires are connected to the film. The leads are, then, run along the cold surfaces and taken out of the chamber using a multi-pin electrically floating connector welded to the top-plate. This way, the gold film is maintained electrically isolated. Then, the wires are hooked up to the current integration system.

Due to the tight geometry in the chamber, it is not possible to place a secondary electron suppression grid in front of the target and therefore, the measured integrated charge, as it is, is an over estimate (since the ejected electrons had the effect of being registered as a positive charge on the target). To account for this, in a separate run, we tried to estimate the contribution of the secondary electrons in the following way. The crystal is placed in a different chamber, where there is a secondary electron suppression grid. Then the current on it is measured alternately with the grid grounded and with the grid held at -600 V. The measured current with the grid negatively biased is about a factor of 6 less than that with the grid grounded. Thus, the integrated charge and in turn the dose have to be renormalized by this factor.

II. Sputtering Setup

The keV Ar sputtering beam is obtained using a home-made sputtering setup. Basically, the gas is ionized using an RF oscillator and accelerated along the source tube to the voltage set by the high voltage power supply (15 kV ion gun). The beam is then extracted from the source and, using a 90°-bending magnet, is deflected into the beam line (Fig. 4.3). The rest of the path is the same as for the MeV beam.

We wanted to use a beam of as low an energy as possible. The main reason is that we would like to limit the damage introduced by the beam to a very thin region. However, the beam optics was not designed for handling beams of very low energies, making it very difficult to get a stable beam. A comfortable beam energy, that was found by trial and error, was about 5 keV. In the keV range, we used the experimental values for secondary electron emission yield (Baragiola *et al.* 1979) to correct for the fact that we had no suppression grid.

5. EXPERIMENTAL DATA

A. PHONON REFLECTION MEASUREMENTS

As discussed earlier (Ch. 3), previous phonon reflection measurements showed that mainly the diffusely scattered phonons are associated with the Kapitza anomalous conductance and thus to understand this anomaly, one is to understand the mechanism(s) of diffuse scattering at an interface. To study this systematically, we decided to use ion beams to modify the surface and/or near-surface region *in situ* and simultaneously study the effect(s) on the reflection of phonons using our phonon-focussed diffuse peak as the probe. To investigate the influence of ion beam irradiation on the specular peaks as well as on the diffuse component, we chose an orientation for the heater and bolometer such that the main contribution to the diffuse scattering would show up as a separate peak (i.e., the geometry used in Fig. 2.7). As discussed in Ch. 2, Sec. B, the origin of this diffuse peak is related to the anisotropy of sapphire. Figure 2.8a shows the ballistic phonon image for a Y-cut sapphire crystal where the heavier lines indicate regions of higher intensity. Now, if the heater and the bolometer are displaced by about 2 mm or less along the X-axis, as shown in Fig. 2.8b, a large part of these high intensity regions intercept. In other words, the phonons emanating from the heater that travel along these focussing directions and arrive at the far surface on the bolometer caustics, are preferentially refocussed in the direction of the bolometer arriving at the detector as a separate broad peak. A large portion of these phonons comes from the region of the reflection surface within the circle in Fig. 2.8b, because that is where the highest intensity regions cross. Therefore, to study the effect of ion implantation on diffuse scattering, the ions must be introduced at a distance along the c-axis of about 7.5 to 8 mm from where the specular peaks come from (shown in Fig. 2.8b). However, the ion beam can only scan about ±3 mm about the center, not enough to affect the region where the main contribution to the diffuse peak comes from. As a result, we chose to use two sets of devices, as shown in Fig. 5.1. This way, the ion beam influences the specular peaks of H_0–B_0 set and the diffuse peak of H_1–B_1. This turned out to be an advantage because each signal can be normalized to the part that is not changing. For example, the specular peaks on the H_0–B_0 set, that the ion beam is expected to affect, can be normalized to the diffuse component of the signal, where no modification is expected to occur. The set H_2–B_2 served two purposes. First, there is an ambiguity as far as the direction of the c-axis is concerned. In other words, one does not know *a priori* whether it is H_1–B_1 set whose diffuse contribution comes from the central region or it is H_2–B_2 set. It is not possible to find the direction of the c-axis by optical techniques, but it is with the x-rays. However, we did not find anybody who was willing to make an attempt at this. Therefore, the first time a crystal is used, one needs to have two sets of devices equally spaced about the center along the c-axis. After this question is resolved and for example H_1–B_1 set is found to be the right set, it is still helpful to have the H_2–B_2 set. In this case, neither the specular nor the diffuse signal should be affected by the ion beam and thus this set can be used as a diagnostic.

As shown in Fig. 5.1b, the reflection surface is covered by a thin gold film (~750Å). The reason is that sapphire is an insulator; as a consequence, the gold film can be used to measure the total integrated charge and thus the total implanted dose. In addition to this, without the gold film, the crystal charges up. In the case of MeV beam energies, the crystal does not charge up to a high enough potential to affect the beam appreciably, but for the low energy (keV) beams, the crystal would merely charge up and repel the ion beam. Several approaches can be taken to deal with this problem. One is to neutralize the beam before it hits the crystal, for instance by ejecting electrons from a hot filament. However, the capture cross section for this process is quite low. The second approach is to neutralize the crystal (or keep it from charging up) by supplying electrons to it. Though plausible, this is rather hard to implement. The main problem is a rather tight geometry of the cryostat (see Fig. 4.1). The only relatively close place where a filament can be put is near to the mirror shown in that figure. However, the filament has to be off-centered such that it does not shadow the incident ion beam. With all the grounded surfaces around (e.g., the LN_2 radiation shields, the walls, etc.), it is not trivial to find a configuration to assure that the ejected electrons will make it to the crystal surface. Instead of this, we decided to study the effect of the keV ion beam on a gold film overlaid on sapphire (Fig. 5.1b). The basic justification is that, due to an almost perfect acoustic match between gold and sapphire, almost all the phonons incident on the interface are expected to cross the interface and be reflected from the gold surface. Thus the effect of low energy ion bombardment of the gold film (and its subsequent sputtering) can be studied by phonon reflection technique. It should be mentioned that we, of course, could have used some other metals such as Al or Cu but Au, being a noble metal, is preferable since in this case some of the subsequent problems such as the oxidation of the film are minimized.

The remainder of this section is organized as follows. In part (I), the effect of the gold film on the reflection signal is presented. With the ion beams, we have explored two regimes. In part (II), the results of the runs where the sapphire crystal was bombarded by 1 MeV Ar^+ are given. In this case, the major part of the ion-beam modification occurs inside the material (about 5000 Å) while leaving the surface unaltered. Then, in part (III), the effects of 7.5 keV Ar^+ sputtering beam are presented. In this instance, the modification is at the surface (about 80 Å).

I. Gold Film

For all the measurements reported in this thesis, the thickness of the gold film is about 750 Å. After cleaning the crystal as thoroughly as possible, the crystal is immediately placed in a UHV evaporation bell jar with the base pressure of 10^{-9} Torr or better. Gold shots of 99.999% purity are used. Right before the evaporation, the gold is outgassed to drive off some of the adsorbates from its surface. Once the pressure is back to its original value, the gold is deposited onto the sapphire crystal. The pressure normally rises to about a few 10^{-8} Torr during the evaporation. The film thickness is determined by the frequency shift of a quartz Sloan thickness monitor. The gold films obtained this way look very shiny; most definitely, they are polycrystalline with grain sizes of about a few 100 Å.

The lower curve in Fig. 5.2 shows the reflection signal from the bare surface. Comparing this signal with the one presented in Fig. 2.7, one sees that the diffuse scattering peak in the former case is appreciably smaller than that in the latter figure. We attribute this to the higher quality of our present sapphire surfaces (i.e., a chemi-mechanically polished surface in opposed to the purely mechanically polished crystal of Fig. 2.7). This confirms our earlier observations that this diffuse component is highly sensitive to the surface quality and thus a good probe for it. The upper curve in Fig. 5.2 shows the reflection signal with the gold film overlaid onto the surface. As can be seen, the specular peaks remain essentially unchanged. In contrast to this, the diffuse peak is substantially suppressed, resembling the effect of LHe and other noble gases.

II. 1 MeV Ar^+ Implantation

Figure 5.3a shows the effect of ion implantation on the specular peaks ($H_0 - B_0$ set) and Fig. 5.3b shows the effect on the diffuse signal ($H_1 - B_1$). The basic trend is the suppression of the specular peaks along with enhancement of the diffuse component. The effect on the specular peaks saturated by a dose of about 8×10^{13} Ar^+/cm^2 in comparison to the saturation dose of 6×10^{14} Ar^+/cm^2 for the diffuse peak.

To find out whether the diffusely scattered phonons are getting to the gold surface, argon atoms were adsorbed on the surface. Figure 5.4 shows that in contrast to the previous observation (Fig. 3.7), the signal remains essentially unaltered.

The crystal was afterwards inspected. In the region where the ion beam struck the gold-sapphire system, the gold film had become very cloudy looking. When it was investigated further under an optical microscope, it was found (Fig. 5.5a) that the region was full of what appeared to be bubbles! Then it was inspected with an SEM (Fig. 5.5b) and our conjecture about the bubbles was correct; however the SEM was not equipped with an x-ray analyzer and thus the exact nature of these bubbles remains unknown.

III. 7.5 keV Ar$^+$ Sputtering

As discussed earlier in this section, ion beams in this energy range lead to sputtering of the gold film. This process continues till all the gold is removed, at which stage the bare sapphire merely charges up and repels the beam. However, before this happens, the ion beam damage is extended to the crystal and thus in addition to the sputtering of the gold film, one is also studying the damage introduced in sapphire. Figure 5.6a shows the effect of the sputtering beam on the specular peaks ($H_0 - B_0$ set) and Fig. 5.6b shows the effect on the diffuse peak. The specular peaks are almost completely gone and the diffuse peak is considerably enhanced. The effect on the specular peaks seems to saturate when about half of the film is sputtered whereas the enhancement of the diffuse peak continues till all the gold is removed.

We then introduced argon atoms onto the reflection surface. As shown in Fig. 5.7, there is no substantial change in the specular peaks, but the diffuse component of the signal is dramatically suppressed, indicating that the modification is at the surface, or better yet, that the phonons leading to the diffuse peak see the surface.

The crystal was inspected afterwards using an optical microscope. No structural change was observed. However, one can still see gold spots left on the surface.

B. X-RAY ROCKING MEASUREMENTS

To get some further information about the effects of the ion beams on sapphire, the irradiated crystals were studied with the X-ray rocking (XRC) technique. We refer the reader to Appendix 1 for a short review of this technique.

I. 1 MeV Ar^+ Irradiated Crystal

Figure 5.8 shows the diffracted x-ray intensity as a function of the angle (here, 0° is taken to be the Bragg angle, θ_B). The dots (.) represent the rocking curve for a virgin crystal. It is rather sharp, symmetric with respect to the Bragg angle and the diffracted intensity at θ_B is very high (~85%), indicating a high quality crystal. The pluses (+) are the x-ray rocking results from the 1 MeV Ar^+ implanted crystal. We see additional structure on the negative tail of the Bragg peak. The structure remained after the gold film was removed indicating that the XRC was not influenced by the presence of the gold film. In the next chapter, we will present our attempts to obtain strain and damage profiles giving rise to the observed structure.

II. 7.5 keV Ar^+ Irradiated Crystal

In this case, the x-ray rocking curve we measured is indistinguishable from that of the virgin crystal. This is attributed to the negligible thickness of the induced damage, too thin to have any effect on the x-ray beam.

C. RUTHERFORD BACKSCATTERING (RBS) MEASUREMENTS

Since this is a rather standard technique, we do not review the principle behind its operation. The interested reader can consult the cited reference (Chu *et al.* 1978).

I. Gold-Covered Crystal

Figure 5.9a shows the RBS data from a gold-covered virgin sapphire crystal. The width of the gold peak is consistent with the 750 Å film thickness. The oxygen and aluminum plateaus are accordingly labeled. The small peak close to the Al plateau seems to be real and is attributed to the existence of Al at the surface (i.e., there are pinholes in the Au film). The small peak superimposed on the tail of the Au peak is not understood. It is plausible that it is Mo, of which our evaporation boats are made, or some other contaminant.

II. 1 MeV Ar^+ Implanted Crystal

Figure 5.9b shows the RBS results from the 1 MeV Ar^+ irradiated crystal. The basic features are the same as in Fig. 5.9a; especially the width of the gold peak is essentially the same, indicating that by implantation, no sputtering of the gold film has occurred. Also, this indicates that no appreciable diffusion of the gold into the sapphire crystal has occurred. We were hoping that by this technique, we could measure the argon dose. However, we did not find any trace of an argon peak. As it turned out, the argon beam goes deep enough inside the sapphire that its peak is washed out by the Al plateau.

III. 7.5 keV Ar^+ Irradiated Crystal

Figure 5.9c shows the RBS run on this crystal. The gold peak is not completely gone, indicating some residual gold left (compare with Fig. 5.9a while noting the logarithmic scale). There exists an Ar peak, pointing to the fact that, while sputtering the gold film, the beam penetrated into the sapphire crystal.

6. DATA ANALYSIS

A. SIGNAL PROCESSING

I. Deconvolution Technique

To be able to study the effects of various modifications more systematically and also more quantitatively, the long decaying background onto which the reflection signal is superimposed had to be subtracted out. The source of this background is attributed, by several authors (Horstman and Wolter 1977), to bulk scattering and is thought to have a t^{-2} dependence. However, our attempt to fit this functional form to the signal failed dramatically. An exponential fit seemed to be much better, but there was no justification for why the background should have this kind of behavior. Thus, we decided to simply fit a cubic SPLINE to the two ends of this background, where it is expected to be free of the influence of the reflection signal, and then interpolate the curve in between. This way, we were able to subtract this background as shown in Fig. 6.1a and 6.1b. Remarkably, it turned out that, as far as the subsequent analysis is concerned (section B below), the SPLINE and the exponential fit were found to give results in agreement within about 2%.

The next step was to deconvolve the various reflection peaks which proved to be a much harder task. The detected widths of these peaks are consequences of several processes: some diffuse scattering from the surface falling into the solid angle subtended by the bolometer, bulk scattering, electronics, etc. making it difficult to deconvolve these peaks reliably. Instead, we made the assumption that all the peaks have the same line shape and used the longitudinal peak, which is unaffected by other peaks, as a model. This permitted us to deconvolve the three overlapping specular peaks (2 transverse and one mode converted), thus segregating out the diffuse contribution. From this, one can see (Fig. 6.1b) that basically the height of the fast transverse (FT) mode and the diffuse peak are unaffected by the other peaks. Thus we took either the height of the FT mode or that of the diffuse contribution as a fixed standard while making the various modifications. For example, for H_0–B_0 set of Fig. 5.1, the height of the FT mode, which is expected to vary, is normalized to that of the diffuse peak and vice versa for H_1–B_1 set.

II. Error Analysis

To be able to compare with each other the reflection signals taken at various stages of a given surface modification, one needs to be sure that a given change in the signal is due to the modification and not an artifact of the experimental setup. In the phonon reflection measurements reported in the previous chapter, the biasing current through the bolometer is kept constant; the bath temperature (i.e., the operating temperature for the bolometers - see Fig. 4.7) is varied while the time of flight (TOF) signal is monitored on an oscilloscope. The criteria for choosing an operating point are a) a relatively large signal, b) linearity and stability of the signal (i.e., being in the linear region of the bolometer transition curve). Once the point is chosen, the TOF signal is recorded. After making some surface modifications, the signal is to be recorded again. However, the bath temperature is not stable over extended periods of time and thus the operating temperature has to be adjusted. Therefore, one source of error, E_1, has to do with our ability (or inability) to reproduce the biasing point of the bolometers. This issue was investigated by purposely changing the operating temperature and simultaneously monitoring the reflection signal. It was found that the uncertainty in the operating point led, at maximum, to about 8% error in the measured signal heights. The other source of error, E_2, is associated with the accuracy in reading a data point (this also involves the estimated uncertainty in the background subtraction). Of course, this is the main contribution when the signal is very small. These two sources of error are taken to be statistically independent and thus the total error is

$$E_{total} = \sqrt{E_1^2 + E_2^2}$$

B. DATA

With the signal processing technique discussed in the previous chapter, we were able to analyze the data accumulated from the various runs in the following way.

I. Gold Film Results

Based on the above data analysis, it is found that about 35% of the diffuse peak disappears into the gold film. At first, this may not seem to be very much, especially when one compares this to the effect of LHe on this peak (Fig. 1.2). In the latter case, our analysis shows that about 85% of the diffuse peak is lost in the LHe. However, this is not a fair comparison. One must remember that due to the superior polish of our present crystal, the magnitude of the diffuse component from this crystal-vacuum interface is considerably smaller (compare Fig.5.2 to Fig. 1.2). In other words, in the present case, there are noticeably fewer phonons that find the surface non-ideal and are, thus, diffusely scattered. As a consequence, when in contact with LHe, there are fewer phonons that are transmitted to the liquid side and thus, the effect, though the same, looks less impressive. Of course, to check the above conjecture, all that is needed is to introduce LHe onto the reflection surface of the present crystal and then compare it directly with the previous results. However, in our new cryostat, this is not possible to do. Since there is a common vacuum for the LHe chamber and the reflection surface (Fig. 4.1), by introducing even just enough He gas to form a few monolayers of He on the surface, the pressure in the vacuum space will be so high as to evaporate off all the liquid He in the LHe chamber (due to the high thermal conductivity of He gas). Instead, we can resort to our observations when adsorbing argon on the surface. As we reported earlier, on the mechanically polished surface, the effect of argon adsorption was identical to that of LHe. In other words, about 85% of the diffuse peak is lost in presence of argon. However, in the present crystal, when argon is introduced, only about 37% of the diffuse peak disappears, exactly as in the case of Au, within the error bars. Thus, if we normalize the gold results with this factor, we see that indeed the effect of gold is strikingly similar to that of solid argon (Taborek and Goodstein 1981), solid hydrogen (Buechner and Maris 1975), solid He and, of course, liquid He (Taborek and Goodstein 1980).

This is a very interesting observation in its own right, especially in view of the fact that the gold film adheres poorly to the surface and is easily peeled off. In spite of this, phonons with characteristic wavelength of 50 Å are easily transmitted across. In the case of the specular peaks, the phonons traverse the gold film, are reflected from the gold-vacuum interface and after crossing the gold-sapphire interface, end up as specular peaks without much degradation. In contrast, the phonons that are diffusely scattered from the sapphire-vacuum interface are lost in presence of the gold film. It is reasonable to assume that the specularly reflected phonons correspond to the long (with respect to the characteristic wavelength of the surface roughness) wavelength portion of the phonon spectrum whereas the diffuse signal constitutes the shorter wavelength part of the spectrum (this hypothesis can be checked by using monochromatic sources and detectors for phonons- a major improvement to our experimental capabilities). The phonon mean free path, being inversely proportional to the phonon frequency, causes a preferential attenuation of the high frequency (diffuse) phonons. However, these phonons, once thermalized, must radiate back into the crystal and be detected by the bolometer. The conservation of energy implies that the same amount of heat must be arriving at the detector regardless of the phonon temperature. Thus, the absence of the diffuse peak cannot be explained by the thermalization process unless either one of the followings takes place. One is that during the thermalization, the heat is transported in the gold film far enough (millimeters) such that it misses the bolometer caustic when it gets back to the crystal and thus is not refocussed in the direction of the bolometer. The other one is that the bolometers are more sensitive to the high frequency (THz) phonons and less so to the lower frequency (100GHz) ones. The investigation of the bolometer spectral sensitivity would shed some light on this matter. Again, this would require the use of monochromatic sources of phonons (Kinder 1985).

II. 1 MeV Ar^+ Implantation Results

The total integrated charge is converted to the implanted dose by assuming a uniformly distributed beam over the mirror opening (see Fig. 4.1 and 4.3) with the radius of about 3 mm. Figure 6.2a shows the behavior of the fast transverse mode (normalized to the unaffected diffuse peak) as a function of the implanted dose. Similarly, in Fig. 6.2b, the height of the diffuse peak (normalized to the unaffected FT peak) is plotted. The basic trend is that by implantation the diffuse contribution increases while the specular peaks are suppressed. The effect saturates by a dose of about 8×10^{13} ions/cm^2 for the specular peaks and at a dose of 6×10^{14} ions/cm^2 for the diffuse peak (with the effect of secondary electron ejection, as discussed in Ch. 4, Sec. D, taken into account).

To estimate the ion beam range and the extent of the damage, we used the TRIM (see Appendix 2) Monte Carlo simulation. Figure 6.3a shows that the ions penetrate into the target with a mean range of 5000 Å and a straggling of 1200 Å. Figure 6.3b shows the TRIM results for the target-atoms displacements. With this information and for the first time, we tried to reproduce the strain and damage profiles that gave rise to the observed structure on the x-ray rocking curve measurements of the 1 MeV Ar^+ implanted crystal (Fig. 5.8). By assuming a linear relationship between strain and the displacement density (as given by TRIM), we were able to reproduce the x-ray results relatively well for $\Delta\theta \leq 0.2°$. The dashed curve in Fig. 6.3b shows the strain distribution that gave rise to diffracted x-ray intensity shown by the solid line in Fig. 5.8. However, we are still puzzled by the long-decaying tail on the Bragg signal. Based on the kinematical model described in Appendix 1 (Eq.(A1.1)), this tail corresponds to regions of higher strain than one deduces from the TRIM simulations (assuming a linear relation between strain and displacement density). It is possible that this tail is associated with the bubbles we reported about in Ch. 5, Sec A. These bubbles might be the implanted argon. Considering the dose and the fact that argon, having a higher atomic number than aluminum or oxygen, is a stronger scatterer for x-rays, it is plausible that it would lead to the diffuse background on the x-ray rocking curve (note the strength of this background). So far, this technique has been most extensively used to study radiation damage in semiconductors (Wie *et al.* 1985a) and less so in insulators (Wie *et al.* 1985b). Due to this lack of information on insulators, the exact cause of this tail would require a more systematic investigation.

Both the TRIM simulation (Fig. 6.3b) and the x-ray rocking curve measurements indicate that target-atom displacements have occurred all the way to the surface. Therefore, the concern was whether the change in the phonon signal was due to the modifications occurring at the surface or deeper inside (Qui *et al.* 1982). However, as was shown in Fig. 5.4, when we introduced thermal neutral argon atoms to the surface creating an adsorbed film, no change in the diffuse signal was observed, leading us to believe that phonons were responding to the modifications inside the material; thus, we have shown unambiguously that the diffuse scattering is not necessarily associated with the surface. This observation is also consistent with the Rutherford backscattering results (Fig. 5.9b) where we observed no detectable change in the thickness of the gold film with respect to that of the untreated substrate.

III. 7.5 keV Ar^+ Sputtering Results

As stated in Appendix 2, the TRIM simulation can be used to estimate the sputtering yields. In the case of 7.5 keV Ar^+ bombardment of gold, this yield was calculated to be about 8 (consistent with Fig. A2.2). With this, one can convert the measured total integrated charge (assuming a uniformly irradiated area of 6 mm in diameter and after correcting for secondary electron emission; see Ch. 4 Sec. D) to the thickness of the gold film removed.

Figure 6.4 shows the results of 7.5 keV Ar^+ sputtering of the gold film. Figure 6.4a is a plot of the height of the FT mode as a function of the amount of gold removed and Fig. 6.4b shows the behavior of the diffuse peak. The basic trend is similar to that of the MeV implantation: an abrupt decline in specular reflection along with a more gradual increase of the diffuse component. However, the effect is quantitatively different, in the sense that it seems to be more pronounced than in the case of the MeV implantation. We shall return to this point in the next section.

Figure 6.5a shows the TRIM simulation for the 7.5 keV Ar^+ beam impinging on Au alone and Fig. 6.5b shows how, as the gold film gets thinner (by sputtering), the damage is extended into sapphire. The mean range of the beam is about 50 Å with straggling of 30 Å. Thus, while removing the gold, the beam is damaging the crystal to a depth of about 80 Å, comparable to the wavelength of the incident phonons and thus permanently altering the reflectivity of the surface.

As can be seen in Fig. 6.4a, the decline in the specular peaks is saturated when only about 300 Å of the gold is removed, long before the damage reaches the surface of the crystal. This is, however, plausible; due to an almost perfect acoustical mismatch between gold and sapphire at near normal incidence, there is practically no reflection at the $Au-Al_2O_3$ interface and thus most of the specular peaks are expected to originate by reflection at the surface of the gold film. That surface has presumably been made rough enough by the time 300 Å have been sputtered away.

Also, we pointed out in the previous chapter that adsorption of a film of argon onto the 7.5 keV Ar^+ irradiated surface led to a dramatic suppression of the diffuse peak (Fig. 5.7), confirming our idea that the effect in this case is a surface phenomenon (and also our use of adsorbed Ar as a diagnostic). Also, this observation shows that the Kapitza anomaly still exists on a clean (contaminant free) but a rough (damaged) surface.

IV. Comparison of the Data

As we mentioned before, the results of 7.5 keV Ar^+ bombardment, though qualitatively similar, are quantitatively different from the observations we made in the case of 1 MeV Ar^+ implantation. In the former case, the specular peaks are almost completely gone in contrast to a factor 2 reduction in the deep implantation case. The most natural way of looking at this difference is perhaps the following. In the case of 1 MeV Ar^+

implantation, as the TRIM calculations predicted and the thermal argon adsorption experiment strikingly confirmed, the damage is mainly confined to the bulk of the crystal, leaving the surface essentially unaltered. As a consequence, the phonons that can make their way through the damaged region can still specularly reflect from the unaltered surface and, provided that they can again cross the damaged region, they are detected at the bolometer as specular peaks. In contrast, the 7.5 keV Ar^+ sputtering beam dramatically alters the surface characteristics, as evident from the argon adsorption results. Therefore, the phonons do not see any flat surface to reflect specularly from.

When considering the specular peaks, the above comparison is justified because, as mentioned earlier, the gold film does not have any appreciable effect on the specular peaks. However, this is not the case for the diffuse signal. One must remember that the 7.5 keV beam removes the gold film as well as damaging the target and thus the enhancement of the diffuse peak is partly due to the damage introduced by the beam and partly due to the removal of the gold film. The cross (x) in Fig. 6.4b shows the height of the diffuse peak for the uncoated virgin surface. The difference between the values marked with the circle (o) and the cross (x) is to be attributed to the effect of the sputtering beam and is in fact comparable to the results of 1 MeV implantation (Fig. 6.2b). Thus, once the effect of the gold film removal is taken into account, the increase in the diffuse peak resembles that of the 1 MeV implantation. It would be very interesting to repeat the keV measurements on a bare sapphire (after solving the charging problem) where we do not have the complications of the gold film and can directly compare the results with the 1 MeV case.

As we mentioned in Ch. 4, Pohl and Stritzker (1982) have measured the low temperature thermal conductivity of sapphire in the temperature range of 0.06 to 2.0 K, corresponding to phonon wavelengths of about 1.7 μ to 500 Å for transverse polarization. In this regime, the phonon mean free path is much longer than the size of the crystal and therefore the thermal conductivity will sensitively depend upon whether the phonons are specularly or diffusely reflected at the surface of the sample. They observed that a 350 keV Xe^+ beam at a dose of $5x10^{15}$ ions/cm^2 as well as an 80 keV Xe^+ beam at a dose of $5x10^{14}$ ions/cm^2 led to an enhancement in diffuse phonon scattering between 0.3 and 2 K, resembling closely their results on a sand-blasted crystal. Even though they did not implant the ions *in situ* and only studied the effect at one dose, their observation is in general agreement with ours. However, the wavelength of our phonons is about 50 Å (~ 19 K) and therefore we probed modifications (on the surface or deeper inside) in a completely different length scale. On a more quantitative level, due to the higher frequencies of the phonons used in this investigation, we were able to resolve the surface modification (7.5 keV Ar^+ - extended up to 80 Å inside the target) from the near surface damage (1 MeV Ar^+ beam - damage peaked at about 5500 Å). As a consequence, in the former case, our results quantitatively agree with those of Pohl and Stritzker (i.e., a complete suppression of the specular peaks), whereas in the latter we see a reduction in the specular reflection that saturates at only about ½ of that of the undamaged crystal. In contrast, Pohl and Stritzker, due to their long wavelength phonons, did not observe any difference between the 350 keV Xe^+ and the 80 keV Xe^+ bombardments.

We have not succeeded in formulating a quantitative model to account for the data. This is mainly due to the fact that we lack quantitative information about the nature of the damage. Qualitatively speaking, the ion beam produces many interstitials, displaced atoms, strain, etc. Even at this qualitative level, our picture of the induced damage is not complete. For instance, the long decaying tail on the x-ray rocking measurements for the 1 MeV implanted crystal remains unexplained. Crudely speaking, the ion beam changes the elastic properties of the damaged region; but, due to the complicated nature of the induced damage, we did not find any theory that would realistically treat this problem.

7. CONCLUSION

In summary, this work has its origin in an effort to investigate anomalous transmission of heat across a solid-LHe interface, a problem known as the Kapitza Anomalous Conductance. In this laboratory, the so-called ballistic-phonon reflection technique was used to study this problem. This way, it was observed that the diffusely scattered phonons are associated with this enhanced transmission.

It was also shown that when only a few monolayers of helium are introduced to the reflection surface, the heat transmission is as efficient as that with bulk helium. As for the thin film results, one possible mechanism of this enhanced heat transmission was attributed to desorption of He atoms. We, then, investigated this possibility as reported in Appendix 3. It was observed that, at low coverages (less than one monolayer), the desorption is dominated by the so-called direct process (*phonoatomic effect*), in which substrate phonons directly desorb the He atoms. However, for higher coverages, the thermal process sets in. The study of the angular distribution of the desorbed atoms in the low coverage limit (the phonoatomic regime) yielded results that contradict the assumption of an *ideal* interface.

We saw earlier that the Kapitza anomaly is associated with the diffusely scattered phonons (i.e., the part of the phonon spectrum that does not see a flat interface). Thus, as both the phonon reflection measurements and the desorption studies indicate, the results are highly influenced by the non-ideality of the interface. Therefore, the acoustic mismatch theory, being based on the assumption of an ideal interface, is not in general applicable to a real surface.

As far as the connection between desorption and the Kapitza anomaly is concerned, we have made some suggestions for future experiments (Appendix 3) to test the following conjecture. In the regime where the Kapitza anomaly sets in (film thickness of about a monolayer or more), the thermal process is the dominant component of desorption. Therefore, it is this process that governs the enhanced transmission of heat in thin He films.

The above observations brought up two questions. The first is why a non ideal interface is much more efficient in transmission of heat. The second is why phonons are so sensitive to surface characteristics. For instance, it is surprising that phonons with 50 Å characteristic wavelengths can see even a submonolayer of He or other more strongly bound adsorbates such as water. With these questions in mind and given the experimental capabilities of our laboratory, we decided to try to investigate the first question and, given the extreme sensitivity of the phonons, try to find out whether this technique can be used as a surface probe. Also, we wanted to know if these phonons are equally sensitive to bulk and subsurface modifications. Thus we set out to answer these questions.

The approach we took was to use ion beams to modify the surface or near surface regions and simultaneously investigate the effects on the reflection phonons. The advantage ion beams offer is that by changing their energy, one is able to vary the depth at which the modification is introduced and by changing their dose, one can control the extent of the modification. The design of the experimental setup, the results and data analysis were reported in Ch. 4, 5 and 6.

We would like to suggest some future experiments as a natural continuation of the present work. These would require some modifications of the experimental setup. The addition of the capability to laser anneal the surface *in situ* would enable one to make an *ideal* surface which is the best starting point for any experiment that wants to probe the effects of surface and near surface modifications (for this, sapphire may not be the most suitable substrate, due to its high thermal conductivity). In conjunction with the above, the ability to evaporate various elements such as gold *in situ* would allow one, starting from an interface that presumably obeys the acoustic mismatch model, to study the onset of the Kapitza anomaly as a function of the contaminants, the beam dose and/or energy.

We believe we have shown that the ballistic phonon reflection technique is sensitive to surface (keV results), subsurface (MeV results) and interface (Au-Al_2O_3 results) characteristics. The obvious advantage of such a technique is that it is non-destructive. Also, it can successfully be applied to various regions within the material of interest. However, while implementing this project, we became aware of several serious drawbacks. First of all, it is technically difficult (e.g., bolometry). However, if there is enough interest, one can overcome many of these inconveniences. More serious is the fact that this technique can only be used for highly perfect, rather large (millimeter size) single crystals. Also, one can only investigate the phenomena at low temperatures. Even in a situation when all of the above problems are circumvented, there remains a critical issue that paradoxically enough resides in the extreme sensitivity of this technique. Basically, these phonons respond to any non-ideality associated with near surface or surface regions. As a consequence, without some complementary information, it appears impossible to interpret the results.

As for the first question, what is the mechanism of the Kapitza anomaly, we have not been able to resolve the issue. We feel that this is partly due to the poor theoretical treatment of phonon scattering off various defects and also due to the lack of detailed information about the exact nature of these imperfections. Also we wonder if the search for *the* mechanism of the Kapitza anomaly is a well posed question. It is conceivable that, due to the multiple nature of the surface imperfections (e.g., adsorbates, geometrical roughness, reconstructions, dislocations, contaminants, etc.), there are several possible mechanisms for the anomaly, with each process contributing according to the specifics of a given experimental condition.

APPENDIX 1. X-RAY ROCKING TECHNIQUE

This technique has been used by previous authors (Wie *et al.* 1985a, 1985b) to measure strain /damage profile induced by ion implantation. For an extensive review, we refer the reader to the listed references (Vreeland and Paine 1986). Here, we briefly present the experimental setup and the principle behind the technique (Speriosu 1981).

A schematic diagram of the setup is shown in Fig. A1.1. The beam emerging from the x-ray source (a conventional electron-bombarded metal target) is a broad-band spherical wave. Single-crystal surfaces of high quality (in this case, (100) face of GaAs) are used to partially polarize the beam and make it monochromatic. To eliminate the K_{α_2} line, adjustable slits are placed between the monochromator and the crystal. This way, only the K_{α_1} line of Fe (the metal target set in the source) reaches the crystal. The sample holder is mounted on a goniometer, enabling the crystal to be "rocked" about ±1.5° maximum from the Bragg angle in steps of 10^{-4} degrees. At every pre-programmed step, the diffracted intensity is measured and stored for further analysis using a data acquisition system. The reflecting power is defined as the ratio of the diffracted intensity to the incident intensity at the sample surface.

If the lattice is strained, the Bragg peak is shifted. In the case of symmetric reflection (i.e., reflection off planes parallel to the surface), the angle shift is related to the perpendicular strain $\varepsilon^{\perp}$ via:

$$\Delta\theta \rightarrow \Delta\theta - \varepsilon^{\perp}\tan\theta_B \qquad \text{(A1.1)}$$

where $$\Delta\theta \equiv \theta - \theta_B ,$$

θ_B is the Bragg angle and $\varepsilon^{\perp}$ is the perpendicular strain.

In ion implanted crystals, a significant fraction of atoms may be dispaced from their lattice positions leading to a change in structure factor. One way to take this into account is to assume that the statistical distribution of atomic displacements from the lattice sites has a Gaussian form. This leads to a mean structure factor:

$$\langle F_H \rangle = e^{-W} F_H^0$$

where F_H^0 is the structure factor of the undamaged crystal for the surface designated by H miller indices and W is the Debye-Waller factor given by:

$$W = -8\pi^2/\lambda^2 \sin^2\theta_B \, U^2$$

where U is the standard deviation of displacements and λ is the wavelength of the x-ray (= 1.936 Å).

Strain and damage distributions are represented by a set of discrete laminae oriented parallel to the surface. Each lamina has its own uniform strain, $\varepsilon^{\perp}$, and random displacement standard deviation, U. The total diffracted amplitude is then the sum of coherently interfering wave fields from the layers (taking proper account of phase and normal absorption).

If the damaged region is sufficiently thin or its structure factor is small, the general equation for the diffracted wave reduces to a much simpler form (the kinematical limit). This is a good approximation for reflecting powers less than 6%.

Although the above arguments are very crude, they have been successfully used to map out the radiation induced damage mainly in semiconductors and in a few insulators. The main problem with this technique is that, due to the lack of any phase information in the diffracted wave, the strain and damage profile are not unique. As a consequence, one needs to have some independent information about the effect of the ion beams by some other means.

APPENDIX 2. ION BEAMS

When an energetic ion enters a solid, it loses energy by electronic and nuclear collisions with target atoms. The amount of energy transferred per unit distance, dE/dx, is referred to as the *stopping power*. Figure A2.1 shows a rough schematic of the stopping power as a function of the energy (Sigmund 1977). The parameter ε is defined as:

$$\varepsilon = \frac{M_2 E}{M_1 + M_2} \frac{a}{Z_1 Z_2 e^2} \tag{A2.1}$$

where $$a \sim 0.885 a_0 [Z_1^{2/3} + Z_2^{2/3}]^{-1/2}$$

with $$a_0 = 0.529\,\text{Å}.$$

The subscript 1 denotes the projectile and 2 the target. M is the mass and Z is the atomic number. As depicted in Fig. A2.1, there exist two broad peaks which can be attributed to two distinct curves describing two different mechanisms of energy loss. The curve at higher energies is referred to as the *electronic stopping power* and the one at lower energies is the *nuclear stopping power*.

At high energies (ε>>1), energy loss to electrons is the dominant process for slowing down the ion: for high velocities ($v \gg e^2/\hbar$ for protons and even higher for heavier particles) the Bethe formula is valid and at lower velocities, $v \lesssim z_1^{2/3} e^2/\hbar$, an estimate by Lindhard and Sharff has proven useful.

At yet lower velocities, nuclear stopping dominates (with its maximum around $\varepsilon = ½$). In this regime, the incident ion undergoes screened Rutherford collisions with the target atoms. The ion suffers an energy loss along with an angular deflection. If the energy transferred to the target atoms exceeds the lattice binding energy, the collision results in a direct displacement of the recoiling atom. The incident ion continues to travel through the solid loosing energy to the target atoms, until it eventually comes to rest. In turn, the recoiling atoms transfer their energies to their neighboring atoms by colliding with them. This way, the energy lost by the incident ion continues to dissipate. This process lasts until, in some region surrounding the path of the incident ion, atoms of the solid are set in motion with isotropically directed trajectories. This region is referred to as a *collision cascade*. The radius and lifetime of this region depend upon the nuclear stopping power. When the trajectory of an atom in the cascade is directed toward the surface of the target, it can leave the surface as a sputtered atom, provided it has enough energy to overcome the surface binding energy. The *sputtering yield*, S, is defined as the number of target atoms removed per incident ion. This is proportional to the nuclear stopping power and inversely proportional to the surface binding energy of the target (Sigmund 1969). As an example, we have shown, in Fig. A2.2, the sputtering yield for gold due to incident Ar^+ ions (Anderson and Bay 1981).

Experimentally, non-negligible sputtering of insulating targets by high energy (MeV/amu) ions has been observed. In this regime (electronic stopping), the ions, as stated earlier, scatter off atomic electrons, leaving behind a track of excited atoms or ions. For target sputtering to occur, some fraction of this deposited energy must end up as kinetic energy of the target atoms, leading to subsequent ejection of some of them (see Griffith 1979, and Cooper 1981)

After the passage of the ion, if the solid remains permanently altered from its original configuration, it is said to be *radiation damaged*. Sputtering and formation of tracks and dislocations are some of the manifestations of radiation damage.

At this moment, let us briefly consider the case of Ar^+ beam incident on sapphire. For this system the maximum electronic stopping occurs at an energy of

$$E_{e,max} = \tfrac{1}{2} M_1 v_{e,max}^2 = \tfrac{1}{2} M_1 Z_1^{4/3} \left[\frac{e^2}{\hbar} \right]^2 \sim 47 MeV$$

where the subscript 1 denotes the projectile, Ar. In contrast, the maximum nuclear stopping occurs at the energy corresponding to $\varepsilon \sim \tfrac{1}{2}$ (see Eq. A2.1):

$$E_{n,max} = \frac{1}{2}\frac{M_1+M_2}{M_2}\frac{Z_1Z_2e^2}{a} \sim 126keV.$$

Therefore, 1 MeV Ar^+ lies in the Lindhard-Scharff regime and 7.5 keV Ar^+ is in the extreme nuclear stopping region.

In this thesis, to estimate various parameters of interest such as ion beam range and the induced damage, we have used TRIM88 software package which is very briefly described below.

TRIM Monte Carlo Simulation Program

TRansport of Ions in Matter (TRIM) is a Monte Carlo simulation which calculates the slowing down and scattering of energetic ions in *amorphous* targets (i.e., with atoms in random locations). This method (Ziegler *et al.* 1985) consists of following a large number of ions or particles in a target. Each step begins with a given energy, position and direction. The particle is assumed to change direction as a result of binary nuclear collisions and move in straight lines between collisions. There exist two energy loss mechanisms: electronic (inelastic) and nuclear (elastic). These two loss processes are assumed to be independent of each other and thus particles loose energy in discrete amounts in nuclear collisions and continuously in electronic interactions. For low energies, where nuclear scattering is more dominant, the program uses an analytic scheme based on solid-state interatomic potential. This program can be used for a wide range of energies (100 eV to several MeV). The lower limit is due to the inclusion of binary collision only and the upper limit results from the neglect of relativistic effects.

The energy transferred to a target atom is further analyzed to give various information of interest, such as damage energy, number of target atom displacements produced and the sputtering yield. In this thesis, we have used TRIM88 (i.e., the 1988 version of the program).

APPENDIX 3. DESORPTION OF He THIN FILMS FROM SOLID SURFACES

A. Models of Desorption

Microscopic models of desorption generally assume that the substrate phonons interact with isolated adsorbed atoms (Lennard-Jones 1935, Bendow and Ying 1973, Summerside *et al.* 1981, Cole and Toigo 1982, Goodman 1982). The simplest case is to assume that a single phonon with sufficient energy desorbs an atom (i.e., single phonon desorption) while conserving the total energy and the component of momentum parallel to the surface (assuming a flat surface). In this context, this process has been called the *phonoatomic effect*. This model is perhaps justified in the case where the surface potential (i.e., the net static interaction between the adsorbate and the substrate) develops just one bound state.

One may also consider processes in which an atom is first excited by an incident phonon or phonons, then desorbed by a subsequent one (i.e., desorption by phonon cascades) (Gortel *et al.* 1980). The states into which the atom is excited are the bound states of the atom in the attractive well due to the substrate; these may be the states of a single atom on the surface or they might be modified by the presence of other adsorbed atoms. Of course, in these cases, life times of various states are very important because atoms can deexcite by radiating phonons before they are desorbed.

A new level of complexity is introduced if one allows the substrate phonons to interact with the states of the film representing motions parallel to the substrate. The film can be thought of as having a temperature of its own, loosely coupled to the substrate phonons. In an extreme model of this kind (thermal model) (Goodstein and Weimer 1983, Weimer and Goodstein 1983), the film is treated as a continuum thermodynamic system, with desorption occurring because the film is warming up above ambient, thereby raising its vapor pressure.

It was shown (Sinvani *et al.* 1984) that both the single phonon model and the thermal model predict rather similar Maxwellian distributions of desorbed atoms from a thermally pulsed substrate. In the thermodynamic model, this distribution arises because the desorption rate is deduced from considerations of detailed balance with the adsorbate vapor. On the other hand, single phonon models produce Maxwellian distributions because only the tail of the Bose-Einstein substrate phonons, with energies greater than the binding energy of the adsorbate, can cause desorption. As a consequence, it is experimentally difficult to differentiate between the two mechanisms.

The angular distribution of the desorbed atoms is one of the few characteristics of desorption for which the two above models make very different predictions. The thermal model predicts a $\cos\theta$ distribution, whereas in the single phonon model, the conservation of the parallel momentum and total energy lead to some spectacular effects in the angular distribution. The fact that the momentum of a phonon of a given energy is more than an order of magnitude less than the momentum of a free atom of the same energy, leads to emission of atoms nearly normal to the interface. Figure 3A.1a shows a geometric construction of this focusing effect. Figure 3A.1b illustrates another effect in the angular distribution. Because the atom energy is a quadratic function of momentum while the phonon energy is linear in momentum, the low energy atoms leave the surface at larger angles than the high energy ones. This correlation between energy and emission angle results in a rainbow-like effect in the desorption signal.

B. Experimental Observations

To investigate this process, Taborek (1982) studied the desorption of ^{4}He atoms from a thin metallic film (same as the heater used in the phonon reflection experiment discussed in Ch. 3) by a heat pulse (see Fig. 3 A.2). He observed the effects predicted based on the single phonon model (i.e., the focussing and the rainbow effect). However, it was found later that his observations were consequences of collisions among desorbing atoms (Cowin 1985).

To eliminate this problem, the experimental geometry was changed to that shown in the inset to Fig. 3A.1 in the enclosed paper (Goodstein *et al.* 1985a). In this experiment, the phonons, injected into the sapphire crystal by the heater, travel ballistically through the crystal (similar to the phonon reflection experiments) and cause ^{4}He to desorb from the upper surface. Due to spreading of the phonons in the crystal, their flux reaching the desorption surface is reduced by three orders of magnitude. As a consequence, the rate of desorption is lowered sufficiently to make collisions among the desorbing atoms negligible. Also, this geometry is more relevant to the problem of the Kapitza anomaly.

As shown in the enclosed paper, we observed that at very low coverages (less than one monolayer) the direct process (i.e., substrate phonons directly desorbing ^{4}He atoms) is the main feature, but as the film thickness increases, the thermal process starts to develop. Finally, at about two monolayers, this process dominates.

Then, the angular distribution of the desorbing atoms was investigated. Both the thermal and the direct processes were shown to have a $\cos\theta$ angle dependence (i.e., no focussing and no rainbow effect). Though expected for the thermal desorption, the observation for the direct process again points to the fact that our surfaces are by no means ideal.

What all this means as far as the Kapitza anomaly is concerned is not clear at the moment because the desorption from the spot where the diffuse peak comes from (Fig. 2.7 and 5.1) was never studied. However, we can make the following conjectures. In the phonon reflection experiments described in Ch. 3, no detectable change was observed in the specular peaks when ^{4}He was introduced onto the reflection surface. Nevertheless, here we observe desorption of He atoms from that spot. Though puzzling at first, one has to keep in mind that in the reflection measurements, since one needs a high temporal resolution, the pulse width used was kept as short as possible (about 30 nsec); but in desorption, to obtain a reasonable signal, the pulse width is typically 1 μsec! In this respect, the desorption signal might be a more sensitive probe of the heat transmission across a solid-LHe interface. Also, as shown in the enclosed paper, the direct process is always rather weak especially when the film thickness is a monolayer or more, where the Kapitza anomaly starts to set in. In this region, the thermal process becomes dominant. Therefore, the Kapitza anomaly might be associated with the thermal process. If this is the case, it means that the thermal desorption is closely related to the non-ideality of the surface and is enhanced by it. It might be interesting to repeat these measurements on a well-characterized surface.

Volume 54, Number 18 PHYSICAL REVIEW LETTERS 6 May 1985

Experiments on Quantum and Thermal Desorption from ^{4}He Films

D. L. Goodstein, R. Maboudian, F. Scaramuzzi,[(a)] M. Sinvani,[(b)] and G. Vidali[(c)]
Low Temperature Physics, California Institute of Technology, Pasadena, California 91125

(Received 24 January 1985)

Desorption of He atoms from thin films may be resolved experimentally into quantum and thermal components. We show that quantum desorption becomes the dominant part of the signal in submonolayer films. We also show that, when all effects of collisions between desorbed atoms are eliminated, quantum desorption is not focused normal to the surface of optically polished sapphire crystals.

PACS numbers: 68.45.Da, 67.70.+n

The ability to investigate experimentally an instance in which a transition from condensed to gaseous states may be related directly to a single quantum event is of obvious importance. Some years ago, experiments were reported in which ballistic phonons in crystals[1] and ballistic phonons and rotons in liquid helium[2] gave rise, respectively, to desorption and evaporation of He atoms. More recently, both techniques have been refined to the point where they yielded convincing evidence of the existence of processes in which a single quasiparticle gave rise to a single desorbed[3] or evaporated atom.[4] In the context of desorption, this has been called the phonoatomic effect. The phonoatomic effect is of additional interest because it is potentially an effective spectrometer for high-frequency phonons, and can be a direct probe of microscopic processes at a crystal surface.

In this paper, we report experiments in which both the dependence of the phonoatomic effect on film thickness and the angular distribution of desorbed atoms are studied. Previously,[1] the phonoatomic effect has appeared as a distinct but small ($\sim 5\%$) contribution to the total desorption normal to the surface plane due to a high-temperature but low-intensity beam of phonons. By reducing the film thickness we are able, in the present work, to take advantage of thermal desorption kinetics[5] to suppress thermal desorption and achieve signals which are dominated by the phonoatomic effect. We are also able, for the first time, to study the angular distribution of desorption under conditions in which the results cannot have been affected by collisions among the desorbing atoms, and in which thermal desorption may be separated experimentally from phonoatomic-effect desorption.

Assuming translational invariance of the surface leads to the expectation that at a plane surface, noninteracting atoms desorbed by single phonons with energies high compared to $k_B T_f$ (T_f is the temperature of the film) will be strongly concentrated in the direction perpendicular to the surface,[6,7] and also that atoms desorbed at wider angles will have lower mean kinetic energies[7] (the rainbow effect). These effects are a consequence of the condition that the interaction conserves both the phonon energy and the component of its momentum parallel to the surface. They are expected for phonoatomic, but not thermal desorption. Taborek[7] has observed the predicted effects in atoms desorbed directly from the surface of a heater, but subsequent analysis has indicated that both the angular focusing and the rainbow effect observed were most probably consequences of collisions among desorbing atoms.[8] Thus, the question of whether there is any kinematic focusing of desorbed atoms remains unresolved.

As a preliminary experiment, an apparatus similar to the one described in Ref. 3 was used. Basically, it consists of a fast heater (10-ns response time) evaporated on the bottom of a 1-cm-thick, optically polished sapphire crystal. The phonons travel ballistically through the crystal and cause He atoms to desorb from a hole in a mask placed on the upper surface. Three bolometers at angles $\Theta = 0°$, $\sim 22°$, and $\sim 45°$ from the normal measure the time-of-flight (TOF) and angular distribution. The experimental geometry and a typical distribution are shown in Fig. 1. The first shoulder at

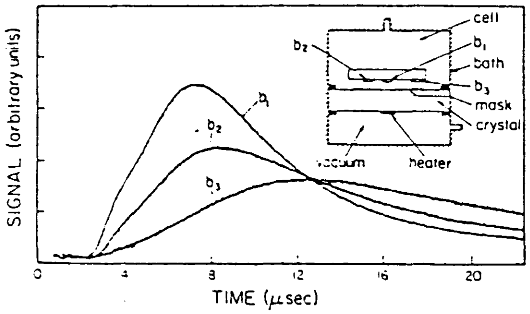

FIG. 1. Time-of-flight spectra at angles of approximately 0°, 22°, and 45° with respect to the surface normal (bolometers b_1, b_2, and b_3, respectively). The inset shows the experimental geometry. The hole in the mask was 0.8 mm in diameter. The distance between the detector plane and the desorbing surface is 1.2 mm. The heater temperature was 19 K calculated according to acoustic mismatch. Ambient temperature was 2.4 K. A typical pulse width used was 180 ns. The chemical potential is roughly -30 K.

earlier times on curve b_1 represents atoms arriving with an associated temperature of about 9 ± 2 K. It is due to atoms desorbed by substrate phonons having an apparent temperature of 9 K. The second peak is due to the process in which phonons are thermalized, raising the temperature of the film slightly above the ambient (~ 2.4 K), and thus causing thermal desorption.

The absence of collisions in our experiment is a consequence of the low rate of desorption. If ΔN atoms per unit area desorb in time τ, the approximate number of collisions per atom among them in subsequent time t (the TOF to the detector) is $\nu = \sigma \Delta l / \times \ln(t/\tau)$, where σ is the collision cross section.[9] In Taborek's experiments, ν is of order 1 ($\sigma \Delta N \approx 1$ per monolayer desorbed, and the logarithmic factor is always ~ 1). In the present experiments, however, the flux of phonons to the desorbing surface is reduced by more than 3 orders of magnitude because of spreading in the crystal. As a result, ΔN is roughly 10^3 times smaller, and we thus conclude that the collisions are far too few to influence the signal.

Figure 2 shows the TOF measurements at 0° as a function of film thickness. At very low coverage (less than 1 monolayer) the phonoatomic peak is the principal feature, but as the film thickness increases, a thermal peak at longer times starts to develop. Finally, at roughly two monolayers, we approach the results obtained previously by Sinvani and co-workers,[1,3] i.e., the thermal peak dominates the signal. In other words, we observe that, on the time scale of our heat pulses, photoatomic desorption dominates in thin films, but thermal processes become more important in thicker films. We return to this issue below.

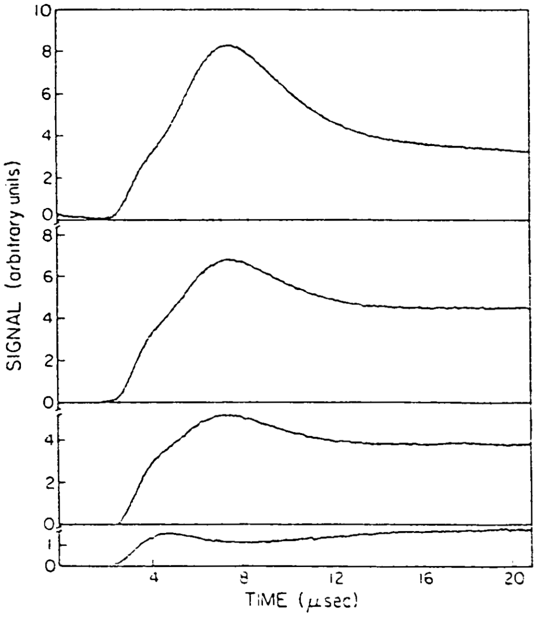

FIG. 2. Time-of-flight spectra at 0° angle for four different coverages with estimated chemical potentials of $\mu \approx -70$ K, -55 K, -40 K, and -30 K, reading from bottom to top.

To be able to study the behavior of these two processes semiquantitatively as a function of chemical potential and angle, we have used a rough deconvolution technique which is basically a four-parameter fit to the signal. The parameters are the magnitudes (S_m) and positions (t_m) of the maxima of the phonoatomic and thermal distributions. Based on the analyses of Sinvani *et al.*,[3] the signals are given by

$$S(t) = S_m \frac{t_m^n}{t^n} \frac{|\mu| + ml^2/2t^2}{|\mu| + ml^2/2t_m^2} \times \exp\left[-\beta_{f,n} \frac{m}{2} l^2 \left(\frac{1}{t^2} - \frac{1}{t_m^2}\right)\right],$$

where l is the distance between the desorbing surface and bolometer planes, and

$$\beta_{f,n} \approx \frac{2t_m^2}{ml^2} \left(\frac{n}{2} + \frac{1}{1 + (2|\mu|/ml^2)t_m^2}\right),$$

and where $n = 5$ for point source and point detector, and $n = 3$ for infinite source and point detector. The phonoatomic and thermal peak temperatures are then given, respectively, by $\beta_{h,n}$ and $\beta_{f,n}$ with $\beta = (k_B T)^{-1}$.

With this technique, the 0° signal can be deconvolved by trial and error. However, as a result of the experimental geometry at 45°, the resolution of the signal's two components is reduced to the extent that the deconvolution leads to ambiguous results. The data in Fig. 1 seem to show only a thermal desorption signal at 45° and were at first thought to be evidence of focusing, but an attempted deconvolution showed some phonoatomic contribution at this angle. Because of the importance of this point, it became evident that the background had to be removed. A new mask was designed, a schematic diagram of which is presented in the inset of Fig. 3. It almost completely removed the background as the signal in Fig. 3 indicates.

Figure 4 shows a typical signal at 0° and 45°, but on a more expanded time scale. As can be seen, a phonoatomic peak is present at 45°. It arrives later than the same peak at 0° by a factor of $\sqrt{2}$, attributable to geometry. There is no rainbow effect, and its magnitude is consistent with a $\cos\Theta$ distribution in the desorbed flux. All of our data have these features. Thus, we find neither kinematic focusing due to phonon desorption, nor focusing due to collisions.

The absence of kinematic focusing can be attributed to surface roughness, surface defects, a damaged layer, impurities, or any other mechanism that can lift the assumption of parallel momentum conservation built

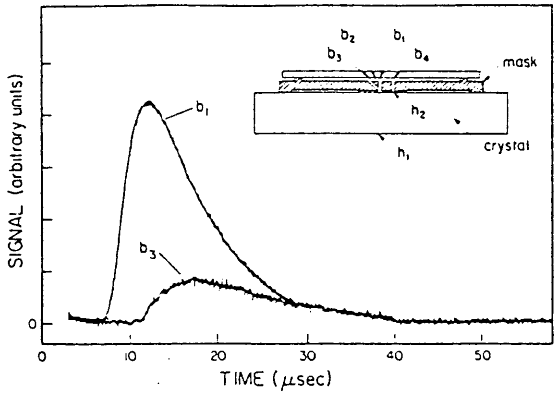

FIG. 3. The new mask, in the inset, and a typical signal at 0° and 45° are shown (from bolometers b_1 and b_3, respectively). The mask, made of stainless steel, covers the whole desorption surface. The two holes are 1 mm in diameter, one at 45° to the other. The bolometers were 3 mm away from the surface. To enhance the signal size, a typical pulse width used was 1 μsec. b_2 was used as a heater to match the calibrations of b_1 and b_3. The heater h_2 and bolometer b_4 were used to measure the chemical potential (Ref. 10) (i.e., film thickness).

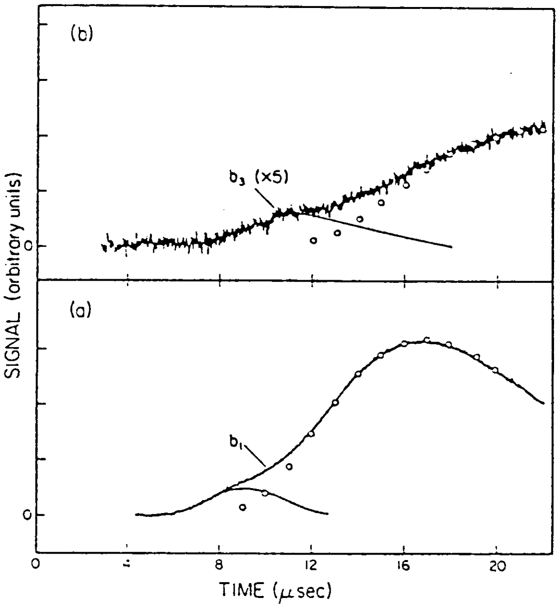

FIG. 4. A typical signal at (a) 0° and (b) 45° is shown on a more expanded time scale than the signal in Fig. 3. The deconvolution technique is depicted, with $n = 5$. The circles represent a fit to the thermal component of the signal, and the solid curve is the subtracted signal (i.e., phonoatomic contribution). $\mu \sim -25$ K.

into the model. Aside from using optically polished crystals and handling them with standard laboratory care, we, at this stage, have no other means to assess the cleanliness of these surfaces or to improve upon them *in situ*. Several methods to achieve better surfaces are under investigation.

We have also studied the evolution of the phonoatomic effect and thermal desorption as a function of film thickness using the new mask. The same general feature was observed; i.e., it appears that in thin films, the phonoatomic-effect contribution dominates, but as the film thickness increases, desorption becomes mainly thermal.

The thermal component can be understood in terms of the thermal time constant τ of the film, the time it takes for the film to reach steady state. Based on either kinetic theory[11] or quantum mechanical calculations,[12] this rate has an exponential behavior: $\tau = \tau_0 \exp(E/k_B T_f)$, where T_f is the film temperature and τ_0 and E are parameters with time and energy units, respectively. E has been shown experimentally to be strongly correlated with the chemical potential.[13]

With the assumption that γ_0 is relatively insensitive to film thickness, the time constant varies by roughly three orders of magnitude from $\mu_1 = -70$ K (our thinnest film) to $\mu_2 = -30$ K (our thickest film), with T_f taken as 4 K, slightly above the ambient temperature, according to the temperature of the thermal component of the signal.

For thick films, it is found that τ is of the order of microseconds, leading to a thin-film time constant of roughly milliseconds. The pulse widths used in these experiments are of the order of 1 μsec during which very little thermal desorption can therefore occur in the case of thin films, causing the spectrum to be dominated by the phonoatomic process. But as the film thickness increases, even though the phonoatomic contribution also increases, the thermal desorption rapidly takes over.

There is abundant evidence that desorption of He is a manifestation of the anomalous Kapitza resistance.[5,14] However, there is no evidence as to whether the mechanism of the phonoatomic effect is related to the Kapitza anomaly since previous experiments concerned with the Kapitza effect could not have detected the contribution of phonoatomic desorption.[15]

Another observation was that the temperature assigned to the phonoatomic-effect peak was at most 9 K, whereas the heater temperature was calculated to be 19 K on the basis of the acoustic mismatch model. Apparently, impurity scattering in sapphire (which goes as the fourth power of frequency) and an imperfect interface between heater and crystal both have the effect of allowing only lower-frequency phonons to arrive ballistically at the desorbing surface. These effects have been commonly observed by other investigators.[16]

In summary, we have shown that it is possible, by taking advantage of thermal desorption kinetics, to suppress thermal desorption leaving the phonoatomic effect the principal component of the desorption signal. We have also shown that once all experimental artifacts are carefully eliminated, phonoatomic desorption is not focused normal to the surface, but is influenced by the surface condition. These results stand in striking contrast to previous experimental pictures and provide the basis for further investigation of quantum desorption.

We would like to thank Milton Cole, Michael Weimer, and Robert Housley for useful discussions, Edward Boud for his technical assistance, and Roman Movshovich for his help in preparing our bolometers. This work was supported in part by the Office of Naval Research, under Contract No. N0014-80-C-0447.

---

[a] Present address: Dipartimento Tecnologie Intersettoriali ali di Base, Energia Nucleare e delle Energie Alternative, I-00044 Frascati, Italy.

[b] Also at Solid State Physics Department, Soreq Nuclear Research Center, Yavne 70600, Israel, and Physics Department, Technion, Technion City, 32000 Haifa, Israel.

[c] Present address: 201 Physics Building, Syracuse University, Syracuse, N. Y. 13210.

[1] M. Sinvani, P. Taborek, and D. Goodstein, Phys. Lett. 95A, 59 (1983).

[2] S. Balibar, Phys. Lett. 51A, 455 (1975); S. Balibar, J. Buechner, B. Castaing, C. Laroche, and A. Libchabor, Phys. Rev. B 18, 3096 (1978); M. J. Baird, F. R. Hope, and A. F. G. Wyatt, Nature (London) 304, 325 (1983).

[3] M. Sinvani, D. L. Goodstein, M. W. Cole, and P. Taborek, Phys. Rev. B 30, 1231 (1984).

[4] F. R. Hope, M. J. Baird, and A. F. G. Wyatt, Phys. Rev. Lett. 52, 1528 (1984).

[5] M. Weimer and D. Goodstein, Phys. Rev. Lett. 50, 193 (1983).

[6] S. C. Ying and B. Bendow, Phys. Rev. B 7, 637 (1973); Z. W. Gortel, H. J. Kreuzer, and S. Spaner, J. Chem. Phys. 72, 234 (1980).

[7] P. Taborek, Phys. Rev. Lett. 48, 1737 (1982).

[8] James P. Cowin, Phys. Rev. Lett. 54, 368 (1985); P. Taborek, private communication.

[9] J. P. Cowin, D. J. Auberbach, C. Becker, and L. Wharton, Surf. Sci. 78, 545 (1978).

[10] M. Sinvani and D. Goodstein, Surf. Sci. 125, 291 (1983).

[11] J. Frenkel, *Kinetic Theory of Liquids* (Dover, New York, 1955).

[12] F. O. Goodman and I. Romero, J. Chem. Phys. 69, 1086 (1978); Z. W. Gortel, H. J. Kreuzer, and R. Teshima, Phys. Rev. B 22, 5655 (1980).

[13] M. Sinvani, P. Taborek, and D. Goodstein, Phys. Rev. Lett. 48, 1259 (1982).

[14] R. C. Johnson, and W. A. Little, Phys. Rev. 130, 596 (1963); G. A. Toombs and L. J. Challis, J. Phys. C 4, 1085 (1971); A. R. Long, R. A. Sherlock, and A. F. G. Wyatt, J. Low Temp. Phys. 17, 7 (1974).

[15] W. Dietsche and H. Kinder, J. Low Temp. Phys. 23, 27 (1975); C. J. Guo, and H. J. Maris, Phys. Rev. A 10, 960 (1974).

[16] A. C. Anderson, in *Nonequilibrium Superconductivity, Phonons and Kapitza Boundaries*, edited by K. E. Gray (Plenum, New York, 1980), and references therein.

REFERENCES

Anderson, A.C. 1980, in *Nonequilibrium Superconductivity, Phonons and Kapitza Boundaries* by K.E. Gray (Plenum, New York) p.1.

Anderson, H.H. and H.L. Bay, 1981, in *Sputtering by Particle Bombardment I*, edited by R. Behrisch (Springer-Verlag, Berlin), p.188.

Anderson, P.W., B.I. Halperin and C.M. Varma, 1972, Phil. Mag. **25**,1.

Axan, B., 1984, Senior Thesis, unpublished (Caltech).

Baragiola, R.A., E.V. Alonso, J. Ferron and A. Oliva-Florio, 1979, Surf. Sci. **90**, 240.

Basso, H.C., W. Dietsche, H. Kinder and P. Leideres, 1984, in *Phonon Scattering in Condensed-Matter*, edited by W. Eisenmenger et al. (Springer, Berlin) p.212.

Basso, H.C., W. Dietsche and H. Kinder, 1986, J. Low Temp. Phys. **65**, 247.

Bendow, B. and S.C. Ying, 1973, Phys. Rev. B **7**, 627.

Bialas, H. and H.J. Stolz, 1975, Z. Physik **B21**, 319.

Braginsky, V.B., V.P. Mitrofanov and V.I. Panov, 1985, *Systems with Small Dissipation*, The University of Chicago Press (Chicago).

Brewer, J.D., B.J. Jeffries and G.P. Summers, 1980, Phys. Rev. B **22**, 4900.

Buechner, J.S. and Maris, H.J., 1975, Phys. Rev. Lett. 34, 316.

Challis, L.J., 1974, J. Phys. C (Solid State Phys.) **7**, 481.

Chu, W.K., J.W. Mayer and M.A. Nicolet, 1978, *Backscattering Spectroscopy* (Academic Press).

Cole, M.W. and F. Toigo, 1982, in *Interfacial Aspects of Phase Transformation*, edited by B. Mutaftschiev (Reidel, Dordrecht, The Netherlands), p.233.

Cooper, B.H., 1981, Ph.D. Thesis, Caltech.

Cowin, J.P., 1985, Phys. Rev. Lett. **54**, 368.

Dietsche, W. and H. Kinder, 1975, J. Low Temp. Phys. **23**, 27.

Espe, W., 1957, *Materials of High Vacuum Technology*, Vol. 1 (Pergamon Press).

Every, E.G., G.L. Koos and J.P. Wolfe, 1984, Phys. Rev. B **29**, 2190.

Farnell, G.W., 1961, Can. J. Phys. **39**, 65.

Federov, F.I., 1968, *Theory of Elastic Waves in Crystals* (Plenum, New York).

Goodman, F.O., 1982, Surf. Sci. **120**, 251.

Goodstein, D.L., G. Paterno', F. Scaramuzzi and P. Taborek, 1980, in *Nonequilibrium Superconductivity, Phonons and Kapitza Boundaries*, edited by K.E. Gray (Plenum, New York), p.665.

Goodstein, D.L. and M. Weimer, 1983, Surf. Sci. **125**, 227.

Goodstein, D.L., R. Maboudian, F. Scaramuzzi, M. Sinvani and G. Vidali, 1985, Phys. Rev. Lett. **55**, 2034.

Goodstein, D.L., 1985, in *Nonequilibrium Phonon Dynamics*, edited by W.E. Bron, NATO Advanced Study Institute (Plenum, New York).

Gortel, L.W., H.J. Kreuzer and R. Teshima, 1980, Phys. Rev. B **22**, 512.

Griffith, J.E., 1979, Ph.D. Thesis, Caltech.

Guo, C.J. and H.J. Maris, 1972, Phys. Rev. Lett. **29**, 855.

Guo, C.J. and H.J. Maris, 1974, Phys. Rev. A **10**, 960.

Herth, P. and O. Weiss, 1970, Z. Angew. Phys. **29**, 101.

Horstman, R.E. and J. Wolter, 1977, Phys. Lett. **62A**, 279.

Kapitza, P.L., 1941, J. Phys. USSR **4**, 181.

Keen, B.E., P.W. Mathews and J. Wilks, 1965, Proc. Roy. Soc. **A284**, 125.

Khalatnikov, I.M., 1965, in *An Introduction to the Theory of Superfluidity* (Benjamin, New York).

Khater, A. and J. Szeftel, 1987, Phys. Rev. B**35**, 6749 and references therein.

Kinder, H., 1981, Physica **107B**, 549.

Kinder, H., 1985, in *Nonequilibrium Phonon Dynamics*, edited by W.E. Bron, NATO Advanced Study Institute (Plenum, New York).

Klemens, P.G., 1955, Proc. Phys. Soc. A**68**, 1113.

Klitsner, T. and R.O. Pohl, 1984, in *Phonon Scattering in Condensed Matter*, edited by W. Eisenmenger et al. (Springer, Berlin) p.188.

Klitsner, T. and R.O. Pohl, 1986, in *Phonon Scattering in Condensed Matter*, edited by A.C. Anderson and J.P. Wolfe (Springer, Berlin) p.162.

Koester, L., S. Wurdack, W. Dietsche and H. Kinder, 1986, in *Phonon Scattering in Condensed Matter*, edited by A.C. Anderson and J.P. Wolfe (Springer, Berlin), p.171.

Lennard-Jones, J.E., 1935, Proc. R. Soc. London, Ser. **A 150**, 442.

Little, W.A., 1959, Can. J. Phys. **37**, 334.

Long, A.R., R.A. Sherlock and A.F.G. Wyatt, 1973, J. Low Temp. Phys. **15**, 523.

Maris, H.J., 1971, J. Acoustical Soc. America **50**, 812.

Maul, M.K. and M.W.P. Strandberg, 1969, J. Appl. Phys. **40**, 2822.

Musgrave, M.J.P., 1970, *Crystal Acoustics* (Holden-Day, San Francisco).

Northrop, G.A. and J.P. Wolfe, 1984, Phys. Rev. Lett. **52**, 2156.

Perrin, N. and H. Budd, 1972, Phys. Rev. Lett. **28**, 1701.

Pohl, R.O., and B. Stritzker, 1982, Phys.Rev. B **25**, 3608

Qui, Y., J.E. Griffith and T.A. Tombrello, 1982, Radiation Effects **64**, 111.

Roesch, F. and O. Weiss, 1976, Z. Physik **B25**, 101.

Sabisky, E.S. and C.H. Anderson, 1975, Solid State Comm. **17**, 1095.

Shiren, N.S., 1981, Phys. Rev. Lett. **47**, 1466.

Sigmund, P., 1969, Phys. Rev. **184**, 383.

Sigmund, P., 1977, in *Inelastic Ion-Surface Collisions*, edited by N.H. Tolk and J.C. Tully (Academic Press, New York).

Sinvani, M., D.L. Goodstein, M.W. Cole and P. Taborek, 1984, Phys. Rev. **B50**, 1231.

Speriosu, V.S., 1981, J. Appl. Phys. **51**(10), 6094.

Summerside, P., E. Sommer, R. Teshima and H.J. Kreuzer, 1981, Phys. Rev. B **25**,6235.

Taborek, P. and D.L. Goodstein, 1979, J. Phys. C (Solid State Phys.) **12R, 4737.**

Taborek, P. and D.L. Goodstein, 1980, Phys. Rev. **B22**, 1550.

Taborek, P. and D.L. Goodstein, 1981, Solid State Comm. **38**, 215, and some other unpublished results.

Taborek, P., 1982, Phys. Rev. Lett. **48**, 1737.

Von Gutfeld, R.J., 1968, in *Physical Acoustics*, vol. V, edited by W.P. Mason (Academic, New York), p.233.

Vreeland, T.Jr. and B.M. Paine, 1986, J. Vac. Sci. Technol. **A4**(6), 3153.

Weber, J., W. Sandmann, W. Dietsche and H. Kinder, 1978, Phys. Rev. Lett. **40**, 1469.

Wei, P.S.P. and A.W. Smith, 1972, J. Vac. Sci. Technol. **9**, 1209.

Weimer, W. and D.L. Goodstein, 1983, Phys. Rev. Lett. **50**, 193.

White, G.K., 1979, *Experimental Techniques in Low Temperature Physics*, 3rd edition (Oxford).

Wie, C.R., T. Vreeland, Jr., and T.A. Tombrello, 1985a, Mat. Res. Soc. Symp. Proc. 35, 305.

Wie, C.R., T. Vreeland, Jr., and T.A. Tombrello, 1985b, Nucl. Instr. Meth. Phys. Res. **B9**, 25.

Wyatt, A.F.G., 1980, in *Nonequilibrium Superconductivity, Phonons and Kapitza Boundaries*, edited by K.E. Gray (Plenum, New York) p.31.

Ziegler, J.F., J.P. Biersack and U. Littmark, 1985, *The Stopping Range of Ions in Solids*, Vol. 1, Chapter 4 (Pergamon Press).

FIGURE CAPTIONS

Fig. 1.1a. P. 92

Schematic diagram of the geometry of a ballistic phonon reflection experiment. A thin-film heater is evaporated on one side of an Al_2O_3 single crystal. By pulsing the heater (made of nichrome), phonons are radiated into the substrate. They traverse the crystal, reflect from the other surface and are detected using a Sn superconducting bolometer.

Fig. 1.1b. P. 93

Reflection signal showing various reflection processes (taken from Taborek and Goodstein 1980). Polarizations are labeled 1, 2, 3 in order of wavespeed (1 = longitudinal, 2 = fast transverse and 3 = slow transverse), arrows indicating the change in polarization upon reflection. Heater and bolometer are separated by 9 mm along the X-axis (2-fold symmetry axis).

Fig. 1.2. P. 94

Reflection signal for heater and bolometer displaced by 2 mm along the X-axis (taken from Taborek and Goodstein 1980). The solid curve is the signal with the reflection surface under vacuum. The sharp peaks are the specularly reflected phonons (labeled using the same notation as in Fig. 1c) whereas the broad peak is from the diffusely-scattered phonons which, due to anisotropy of Al_2O_3, are preferentially focussed in the direction of the bolometer. The small peak at 4.5 μs is attributed to double reflection process. The dashed curve shows the effect of adding liquid He. The specular peaks remain essentially unchanged whereas the diffuse signal is dramatically suppressed (Kapitza anomaly). The long decaying background, onto which the reflection signal is superimposed, is thought to be due to bulk scattering.

Fig. 2.1. P. 95

Drawing for deriving the anisotropic phonon-intensity distribution in real space from a known $\vec{k}$-space distribution.

Fig. 2.2. P. 96

Slowness surfaces for sapphire. It shows a grid of lines of constant θ_k and ϕ_k at 5° intervals in the range $-30° \le \phi_k \le 120°$ and $0° \le \theta_k \le 180°$. The lines of zero Gaussian curvature are shown as heavy lines. The Cartesian axes are oriented with respect to the standard hexagonal axes as follows: $X \| [11\bar{2}0]$, $Y \| [1\bar{1}00]$, $Z \| [0001]$. (a) ST sheet. (b) FT sheet. (c) L sheet (taken from Every *et al.*, 1984).

Fig. 2.3. P. 97

Group velocity surfaces for sapphire. They have been constructed by mapping out the set of group velocities corresponding to the grid of slowness vectors in Fig. 2.2. The lines along which this surface is folded correspond to the lines of zero Gaussian curvature in Fig. 2.2. The dashed curves correspond to ellipses of conical refraction. (a) ST sheet. (b) FT sheet. (c) L sheet (reduced in size by a factor of 2) (taken from Every *et al.*, 1984).

Fig. 2.4. P. 98

Schematic polar plot of the constant energy surface in $\vec{k}$ space for the crystallographic plane defined by $\vec{k}_{inc}$ and the surface normal $\hat{n}$. The inner curve represents the quasi-longitudinal mode, which always has the larger phase velocity. The larger curves correspond to the two quasi-transverse modes. If the solid were isotropic, these curves would be circles. The $\vec{k}$ vectors of the three reflected waves, which are related to the incident wave by the relation $\vec{k}_{inc,||} = \vec{k}_{ref,||}$ are determined by the geometrical construction illustrated in the figure (taken from Taborek and Goodstein 1980).

Fig. 2.5. P. 99

Calculated specularly-reflected-flux singularity lines in the X plane (taken from Northrop and Wolfe 1984) .

Fig. 2.6. P. 100

a) The geometry for the diffuse signal calculation. b) The contribution to the diffuse signal at a time t comes from a circular annulus on the reflection surface. c) A plot of the signal expected from a rough surface. The signal has a sharp onset at the time that a specular signal would arrive ($t = 2h/c$).

Fig. 2.7. P. 101

Reflection signal for heater and bolometer displaced by 2 mm along the X-axis (taken from Taborek and Goodstein 1980). The solid curve is the signal with the reflection surface under vacuum. The sharp peaks are the specularly reflected phonons (labeled using the same notation as in Fig. 1c) whereas the broad peak is from the diffusely-scattered phonons which, due to anisotropy of Al_2O_3, are preferentially focussed in the direction of the bolometer. The small peak at 4.5μs is attributed to double reflection process. The long decaying background, onto which the reflection signal is superimposed, is thought to be due to bulk scattering.

Fig. 2.8a. P. 102

Monte Carlo calculation of the ballistic phonon image for sapphire. The crystal face is cut in the $[1\bar{1}00]$ direction (i.e., Y-cut). Bright regions indicate directions of high phonon flux. The image represents a ±60° horizontal scan with the $[1\bar{1}00]$ direction (Y-axis) at the center of the pattern. The fast and slow transverse caustics are identified. The length scale is shown for a 1 cm-thick crystal. (Courtesy of D.C. Hurley and J.P. Wolfe, University of Illinois).

Fig. 2.8b. P. 103

The effect of displacing the heater and the bolometer (shown by the pluse signs) along the X-axis by 2 mm. The figure shows the intersection of the heater and the bolometer caustics with the reflection surface. The intersection of these two caustics provides a high-focusing channel for nonspecular scattering which gives rise to the large peak in the reflection signal (Fig. 2.7).

Fig. 2.9. P.104

Waves created at an interface by a longitudinal wave. Subscripts are defined in the following way: 0-incident wave, 1-reflected wave, 2-transmitted wave, L-longitudinal wave, T-transverse wave. A similar behavior occurs for incident transverse waves. Here, both solids are assumed to isotropic. In the case of anisotropic solids, each incident wave, in general, could lead to three reflected and three transmitted waves.

Fig. 4.1. P.105

Schematic diagram of the UHV cryostat. The crystal, looking into the beam line, is mounted on a copper block which is in direct contact with the LHe bath. To reduce the heat loss due to room temperature radiation, the LHe reservoir is surrounded by a LN_2 chamber as well as a LN_2 radiation shield. The operating period is about 4 hours and the lowest achievable temperature is ~ 2 K. To check the quality of the beam (its alignment, uniformity, etc.) a shutter is suspended from the LHe pot. When closed, the beam sees a quartz crystal, mounted on the shutter, which fluoresces due to the impinging ions. When the beam is in a satisfactory shape, the shutter is open and the beam hits the crystal.

Fig. 4.2a. P. 106

A closer look at how the crystal was originally mounted on the cryostat. As can be seen, both sides of the crystal were under vacuum. Around the rim, the crystal is in direct contact with the LHe as a result of which many low-temperature leaks were encountered.

Fig. 4.2b. P. 107

With this design, both sides of the crystal are still in vacuum, but now the crystal is no longer in direct contact with LHe, removing the problems with cold-leaky joints.

Fig. 4.3. P. 108

Top view of the experimental setup, showing the pumping system as well as the beam line. The MeV implantation beam was generated by a tandem van de Graaff accelerator. Using a 15 kV ion gun, low energy (7.5 keV) sputtering beam was produced and bent into the main beam line via a 90° bending magnet. Using a mirror along with a viewing port, one can see the beam spot on the shutter right before it hits the crystal.

Fig. 4.4. P. 109

Schematic diagram of the pumping system used to cool the LHe bath below its condensation point at ambient pressure (4.2 K). This is achieved by using a mechanical pump along with a vacuum regulator valve (Lake Shore Cryotronics, Inc. model 329) That enables us to maintain the temperature constant to a few mK. The bath temperature is determined by measuring the vapor pressure using a differential pressure gauge and a remote pressure sensor. The values are compared to a Ge thermometer located at the bottom of the LHe chamber. The amount of LHe in the chamber is measured by using a LHe level sensor (Cryomagnetics Inc.).

Fig. 4.5. P. 110

Schematic diagram of the mask used for the fabrication of heaters and bolometers. Pieces (A) and (B), made of brass, are separately machined and assembled as shown in part (C). The mask is, then, placed on the crystal and aligned with respect to its crystallographic axes, as shown. This way, the whole crystal is covered expect where the slits are (i.e., where the heaters or the bolometers are to be).

Fig. 4.6a. P. 111

Schematic diagram of the heater. The periphery (0.25 mm x 6 mm) indicates one of the slits in Fig. 4.5. After evaporating nichrome and then, on top of it, copper, the copper is gradually etched from the central region till the resistance is about 50 Ω ± 1 Ω. The two indium dots, pressed onto the ends, are used to make electrical connections to the device, as shown. To maintain the 50 Ω resistance in the heater circuitry, two twisted copper wires (with 50 Ω characteristic impedance) are used to connect the device to the 50 Ω coaxial cable.

Fig. 4.6b. P. 112

Schematic diagram of a bolometer. To obtain a reasonable resistance over a small area, a snake pattern is used as shown. The dimensions are indicated. Photolithographic techniques are used to fabricate the device (see the text). The rest of the circuitry is the same as that for the heater (Fig. 4.6a).

Fig. 4.7. P. 113

Superconducting transition curve of one of our bolometers. The bath temperature is adjusted such that the bolometer is in the middle of its transition temperature (in this case, ~3.658 K). Phonons arriving at the bolometer, cause its temperature to change, which in turn leads to a change in its resistance and thus in the voltage across the device. The normal biasing current used is ~200 μA.

Fig. 4.8. P. 114

The SEM pictures at two different magnifications showing the diffusion of indium into tin.

Fig. 4.9. P. 115

Schematic diagram of the electronics used in phonon reflection experiment. A pulse generator with fast rise and fall times (~ 5 nsec) is used to pulse the heater and raise its temperature from 3.7 K (ambient temperature) to ~ 19 K. Typical values for the pulse duration is 30 nsec and for the pulse repetition rate is 100 kHz. Some distance away from the heater is a superconducting bolometer which is biased in the middle of its superconducting transition. Reflected phonons, arriving at the bolometer, raise its temperature, leading in turn to a change in its resistance and thus a change in the voltage across the device. Then, using a preamplifier, this change is amplified 100 times and after being averaged by a box-car integrator, is recorded on an X-Y recorder.

Fig. 4.10. P. 116

A schematic diagram showing the layout of the accelerators. The MeV Ar^+ beam was extracted from the JN and, after passing through the Tandem, was energy selected with a 90° magnet. The low energy sputtering setup was used to generate the 7.5 keV Ar^+ beam. Using a bending magnet, the beam was introduced to the experimental chamber.

Fig. 5.1a. P. 117

Top view of the crystal showing the positions of the heaters and bolometers used in the experiments reported here. The beam hits the center of the crystal (~ 6 mm in diameter). In this case, the specular peaks of the $H_0 - B_0$ set are affected as well as the diffuse peak of the $H_1 - B_1$ set. Neither the specular peaks nor the diffuse peak of the $H_2 - B_2$ set should see the incident beam and thus we use this set to make sure nothing spurious is happening.

Fig. 5.1b. P. 117

Side view of the crystal showing the gold film overlaid on the crystal. Sapphire, being an insulator, cannot be directly used to measure the beam current and thus the beam dose. To be able to do so, a 750 Å Au film was overlaid on the surface. Also in the case of the low energy (keV) beam, the gold film is essential; without it the crystal would charge up and repel the beam.

Fig. 5.2. P. 118

Phonon reflection signal for the same geometry as in Fig. 2. The lower curve is for the reflection surface in vacuum and the upper curve is with 750 Å of Au evaporated onto the surface. Though the specular peaks remain essentially unchanged, the diffuse peak is considerably suppressed. The dashed curves are the SPLINE fits to the background (see Ch. 6, Sec. A).

Fig. 5.3a. P. 119

Reflection signals showing the effect of 1 MeV Ar^+ implantation on the specular peaks as shown in the inset. The upper trace is the signal prior to implantation and the curve is taken after 2.4×10^{14} Ar^+/cm^2 implantation dose. As seen in the inset, in this case, the beam is affecting the specular peaks only. The dashed curves are SPLINE fits to the background (see Ch. 6, Sec. A).

Fig. 5.3b. P. 120

Phonon reflection signal showing the effect of 1 MeV Ar^+ implantation on the diffuse peak as shown in the inset. The reflection surface is covered with 750 Å of Au. The upper curve is the signal from a virgin crystal whereas in the lower trace, 1 MeV Ar^+ is implanted in the substrate (~ 7.3×10^{14} Ar^+/cm^2). The inset shows that in this case, the beam is only affecting the diffuse peak as can be seen from the traces. The dashed curve is a SPLINE fit to the background (see Ch. 6, Sec. A).

Fig. 5.4. P. 121

Phonon reflection signal showing the effect of thermal argon adsorption on the 1 MeV Ar implanted crystal. The upper curve is the signal prior to the adsorption and the lower trace is after. As can be seen, no appreciable change in any part of the signal occurred (compare with Fig. 1.2). The dashed curves are SPLINE fits to the background (see Ch. 6, Sec. A).

Fig. 5.5. P. 122

(a) Optical picture of the MeV bombarded region of gold-sapphire system. The region appears to be full of bubbles. (b) SEM picture of the spot showing the bubbles.

Fig. 5.6a P. 123

Phonon reflection signal showing the effect of 7.5 keV Ar sputtering of the gold film (overlaid on sapphire) on the specular peaks (see the inset to Fig. 5.3a). The upper curve is the signal from a virgin crystal (with 750 Å of Au) whereas in the lower trace, the ion beam has completely sputtered the gold film away. The dashed curves are SPLINE fits to the background.

Fig. 5.6b. P. 124

Reflection signal showing the effect of 7.5 keV Ar sputtering of the gold film (on sapphire) on the diffuse peak (see the inset to Fig. 5.3b). The upper trace is the signal prior to irradiation and the lower curve is taken after all the gold is sputtered away. The dashed curves are SPLINE fits to the background.

Fig. 5.7. P. 125

Reflection signal showing the effect of thermal Ar adsorption on the 7.5 keV Ar irradiated crystal. The lower curve shows the signal prior to the adsorption whereas the upper trace is the signal after. Note that, even though the specular peaks remain unchanged, the diffuse peak is noticeably suppressed (compare with Fig. 5.4 and 1.2). The dashed curves are the SPLINE fits to the background.

Fig. 5.8. P. 126

X-ray rocking measurements on virgin as well as 1 MeV Ar^+ implanted Al_2O_3. The dots (·) are the measured intensity of the diffracted x-ray for the virgin crystal as a function of the tilt angle about the substrate Bragg peak and the pluses (+) show the effect of the Ar^+ implantation. The solid curve is the calculated x-ray rocking intensity using kinematical x-ray model for the strain profile of Fig. 6.3b.

Fig. 5.9. P. 127

Rutherford backscattering spectrum for 3 MeV $^4He^+$ at scattering angle of 165° : a) gold-sapphire system prior to any bombardment; b) 1 MeV Ar implanted crystal; c) 7.5 keV Ar sputtered crystal. The various peaks are labelled accordingly. See the text (Ch. 5) for further detail. The energies of the backscattered ions are given by:

$$E = (3.2 \pm 0.016) N_c - 37 \pm 9.9\, keV$$

where N_c denotes the channel number.

Fig. 6.1a. P. 130

Reflection signal showing the background subtraction scheme. Arrows indicate the points where, we believe, the background is free from the influence of the reflection peaks. To these point (normally 6), a cubic SPLINE is fitted (dashed curve).

Fig. 6.1b. P. 131

The reflection signal with the background subtracted (Fig. 8a) showing the deconvolution scheme. By assuming the line shapes of the two transverse peaks (2 → 2, 3 → 3) and the mode-converted peak (2 ↔ 3) to be the same as that of the longitudinal peak (1 → 1), one can successively deconvolve these three peaks and the diffuse peak. Note that the heights of the fast transverse mode (2 → 2) and the diffuse peak are unaffected by the other peaks and therefore we have used these two peaks as means to quantify the effect of each treatment.

Fig. 6.2a. P. 132

The height of the fast transverse peak, normalized to the amplitude of the diffuse peak, as a function of the 1 MeV Ar implanted dose. Note that here the signal is saturated by the dose of 8×10^{13} ions/cm^2 in contrast to the dose of 6×10^{14} ions/cm^2 in the case of the diffuse signal. The error bars are due to uncertainty in the reproducibility of the biasing point of the bolometer after each measurement in addition to reading errors (see Ch. 6, Sec. A).

Fig. 6.2b. P. 133

The height of the diffuse signal, normalized to the unaffected amplitude of the fast transverse peak, as a function of the implanted 1 MeV Ar^+ dose. The error bars are due to uncertainty in the reproducibility of the biasing point of the bolometer after each measurement in addition to the reading error (see Ch. 6, Sec. A). The squares (□) are the data taken on 10-7-87 where as the circles (○) are taken on 10-20-87. In between, the cryostat was warmed up to room temperature and cooled back down. We see some weak evidence for annealing of the induced damage.

Fig. 6.3a. P. 134

TRIM Monte Carlo simulation of the range of a 1 MeV Ar^+ beam in Al_2O_3. The mean range is about 5400 Å with a straggling of 900 Å.

Fig. 6.3b. P. 135

The solid curve shows the TRIM results for target-atom displacement in the case of 1 MeV Ar^+ bombardment. The dashed curve is the strain distribution found by trial and error which led to a good fit to the x-ray rocking curve of Fig. 5.8 (see Ch. 6, Sec. B).

Fig. 6.4a. P. 136

The height of the fast transverse peak, normalized to the unaffected amplitude of the diffuse peak as a function of the amount of Au removed. Note that the signal is saturated by the time 300 Å of Au is removed in contrast to a more gradual enhancement of the diffuse peak (Fig. 6.4b). Also in this case, the specular peaks are almost completely gone in contrast to a factor of 2 reduction in the MeV implantation case.

Fig. 6.4b. P. 137

The height of the diffuse peak, normalized to the unaffected amplitude of the fast transverse peak, as a function of the integrated charge for 7.5 keV Ar^+ bombardment. The arrows on the horizontal axis indicate how much gold is removed. The circles (O) are the data taken on 1-7-88 whereas the diamonds (♦) are the data taken on 1-10-88. Between these two runs, the crystal was warmed up to room temperature and cooled back down. Again we see an indication of some possible annealing of the induced damage. The cross (x) indicates the height of the diffuse peak for a virgin crystal without the gold film (see the text).

Fig. 6.5a. P. 138

TRIM Monte Carlo simulation of the range of a 7.5 keV Ar beam in gold. The mean range is about 55 Å with a straggling of 30 Å.

Fig. 6.5b. P. 139

TRIM Monte Carlo simulation of the range of a 7.5 keV Ar beam in (50 Å) gold-sapphire system. The mean range is about 65 Å with the straggling of 35 Å.

Fig. A1.1. P. 140

A schematic diagram of the rocking curve setup.

Fig. A2.1. P. 141

Schematic diagram of the stopping power of an ion as a function of energy.

Fig. A2.2. P. 142

Sputtering yield (Y) for gold as a function of incident Ar ion energy. The theoretical values (dashed curve) agrees well with the experimental data (taken from Anderson and Bay 1981).

Fig. A3.1. P. 143

Experimental configuration originally used to study desorption of He atoms from the surface of a constantan film (taken from Taborek, 1982).

Fig. A3.2. P. 144

Curves of constant energy in momentum space for atoms above the interface and phonons below, drawn to scale with E_b = 30 K. (a) Geometric construction which shows that parallel momentum conservation leads to atoms emitted almost normal to the interface. (b) The angular width of the atomic critical cone depends upon the energy, with the high energy atoms emitted into a narrow cone. This results in an atomic rainbow in the desorption spectrum (taken from Sinvani *et al.*, 1984).

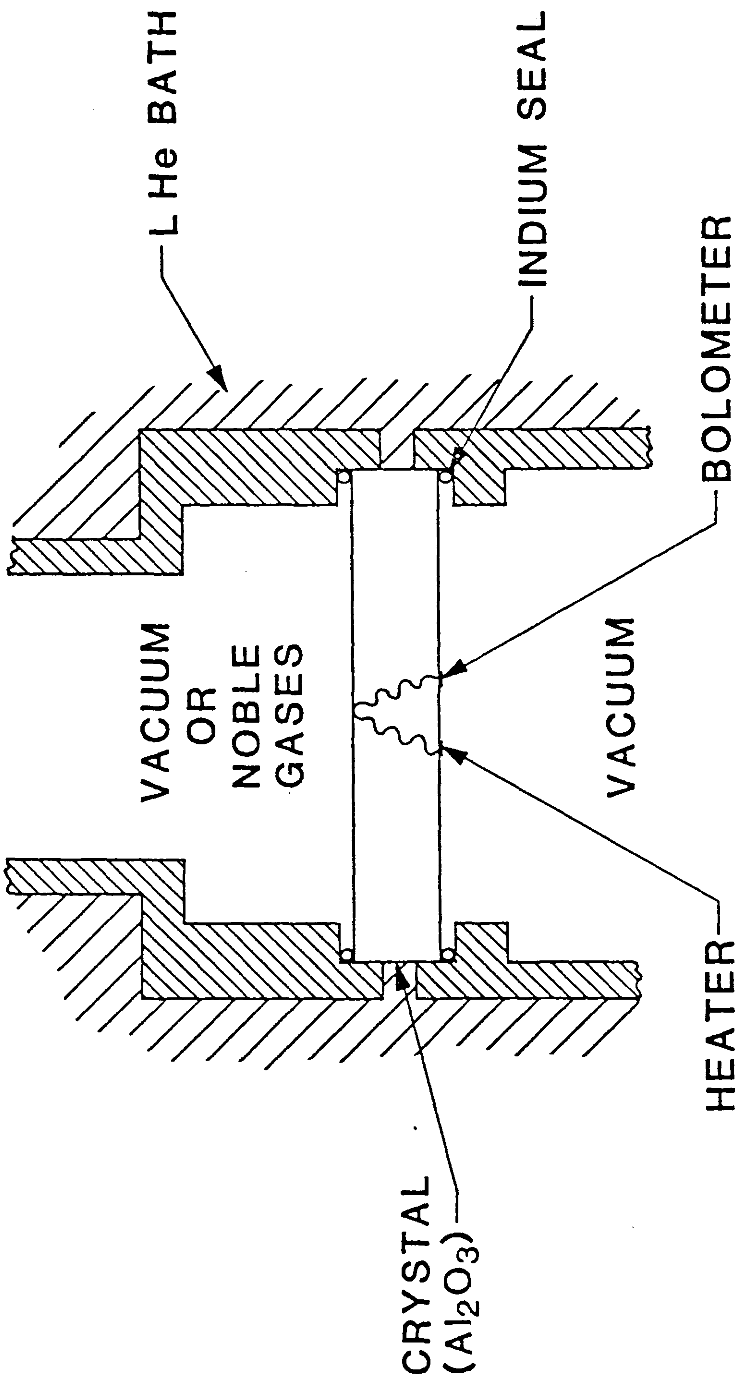
L He BATH
INDIUM SEAL
BOLOMETER
VACUUM OR NOBLE GASES
VACUUM
HEATER
CRYSTAL (Al_2O_3)

Fig. 1.1a

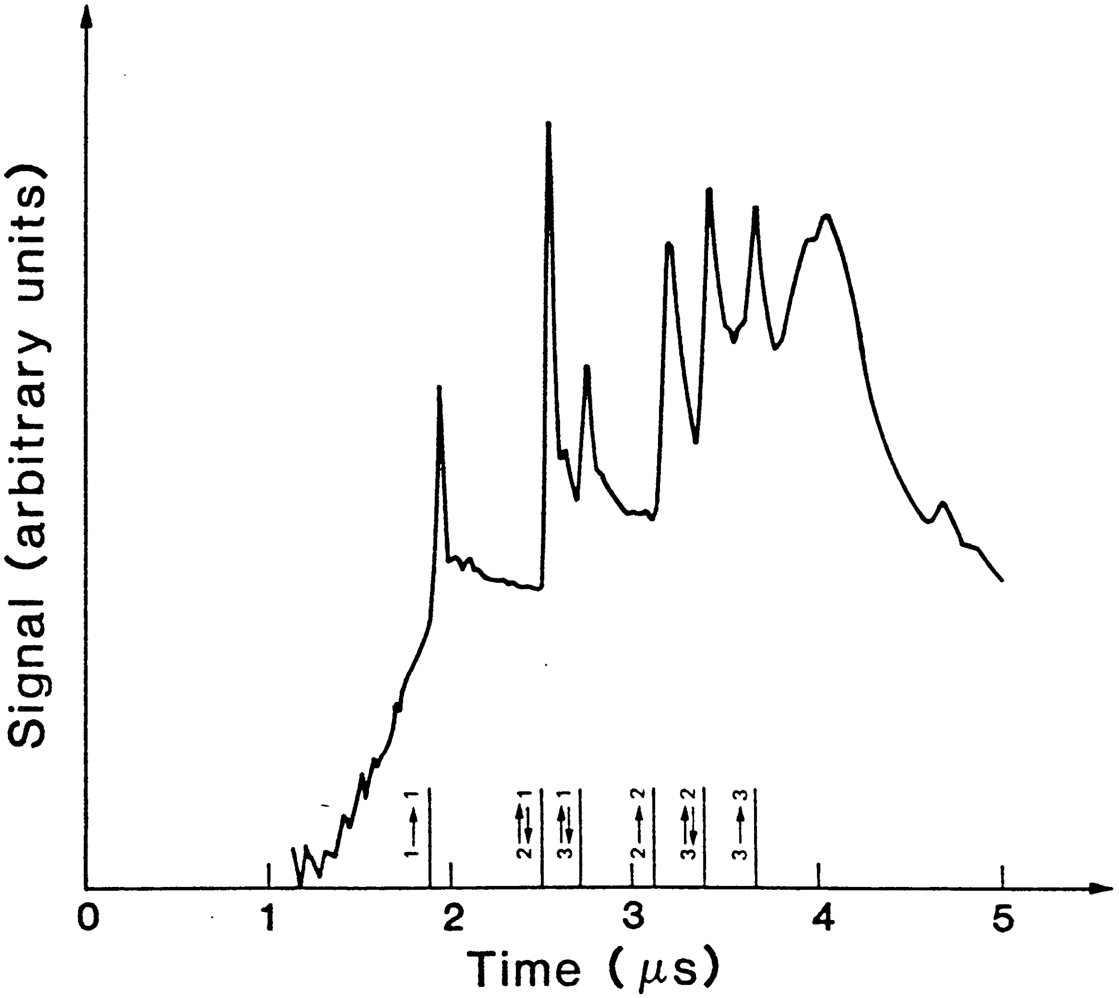

Fig. 1.1b

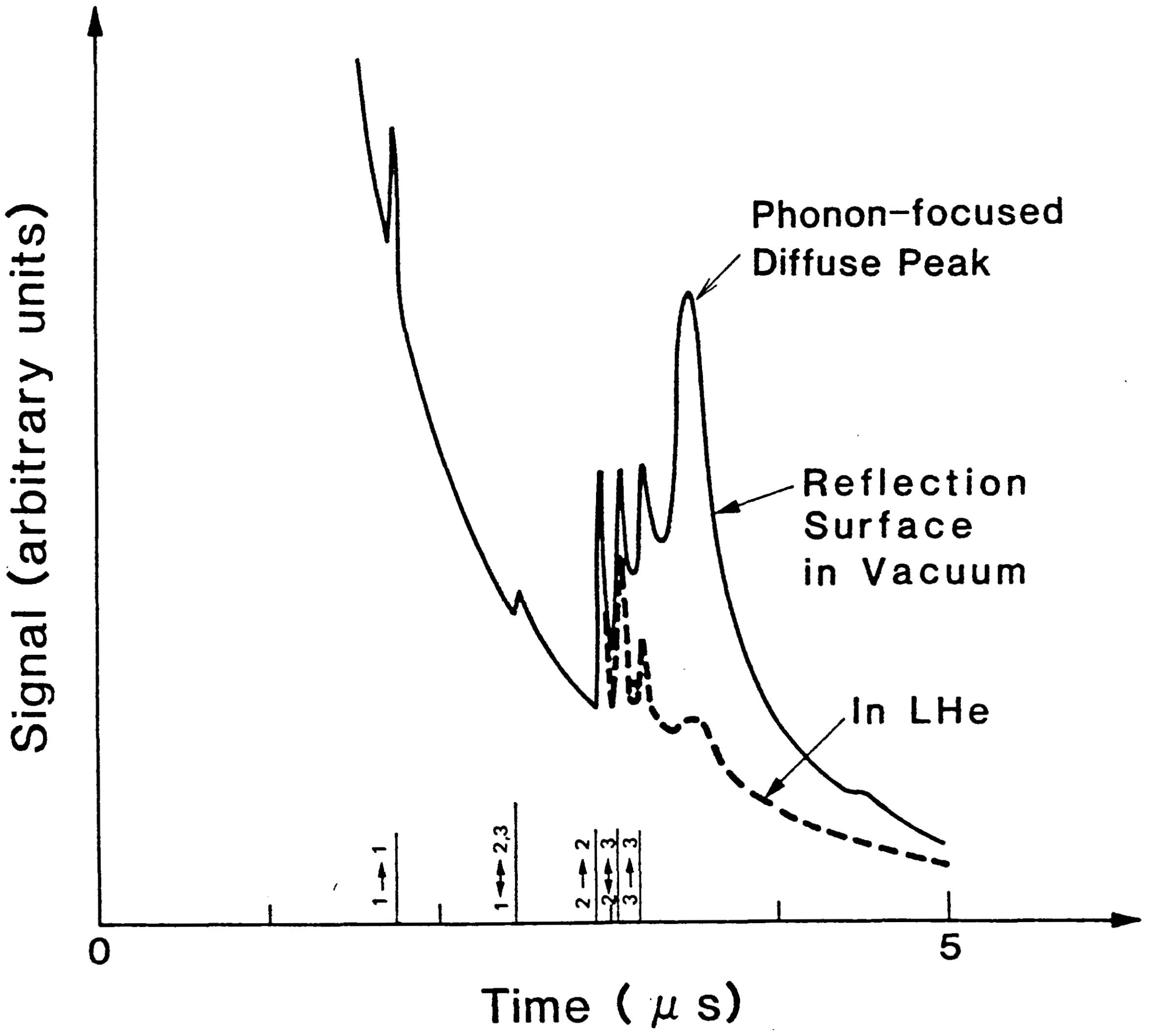
Signal (arbitrary units)
Phonon-focused Diffuse Peak
Reflection Surface in Vacuum
In LHe
1 → 1
1 ↔ 2,3
2 → 2
2 ↔ 3
3 → 3
0
5
Time (μ s)

Fig. 1.2

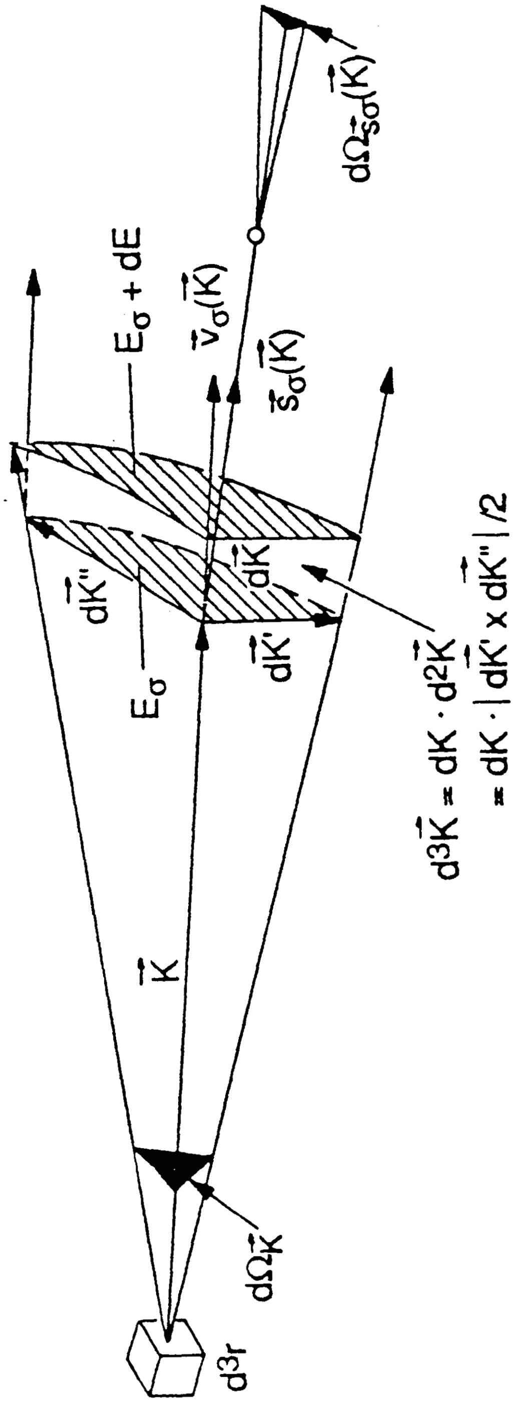
d^3r
$d\Omega_{\vec{K}}$
$\vec{K}$
E_σ
$d\vec{K}''$
$d\vec{K}'$
$d\vec{K}$
$E_\sigma + dE$
$\vec{v}_\sigma(\vec{K})$
$\vec{s}_\sigma(\vec{K})$
$d\Omega_{\vec{s}_\sigma}(\vec{K})$
$d^3\vec{K} = dK \cdot d^2\vec{K}$
$= dK \cdot |d\vec{K}' \times d\vec{K}''|/2$

Fig. 2.1

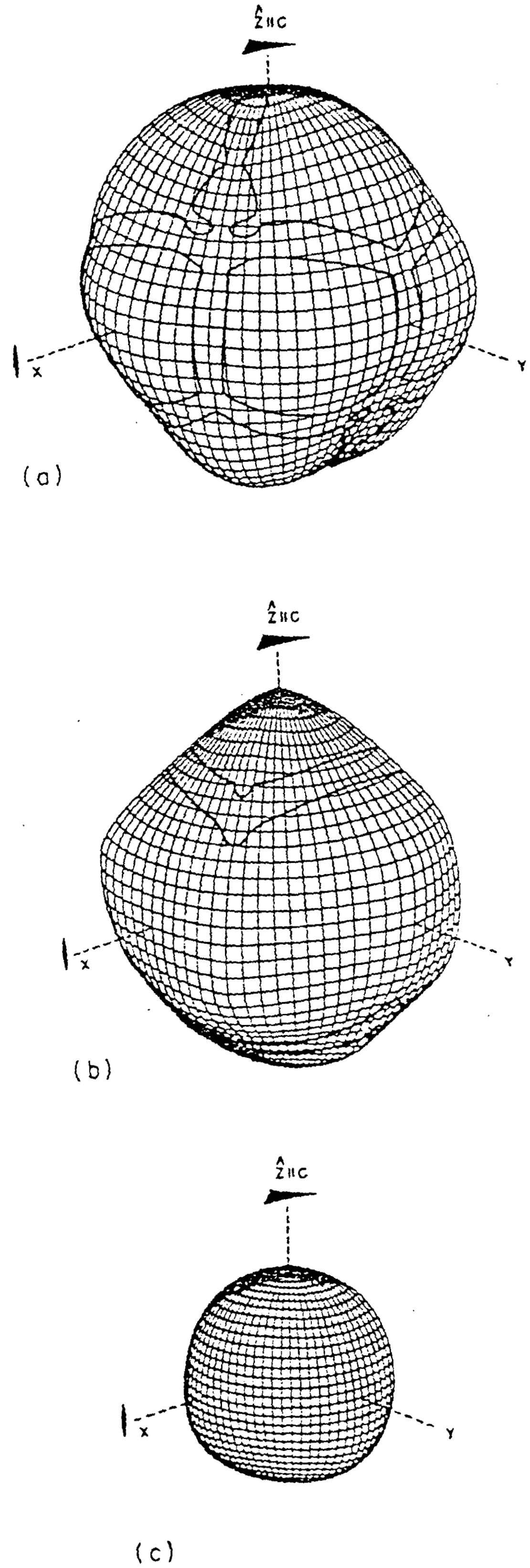

Fig. 2.2

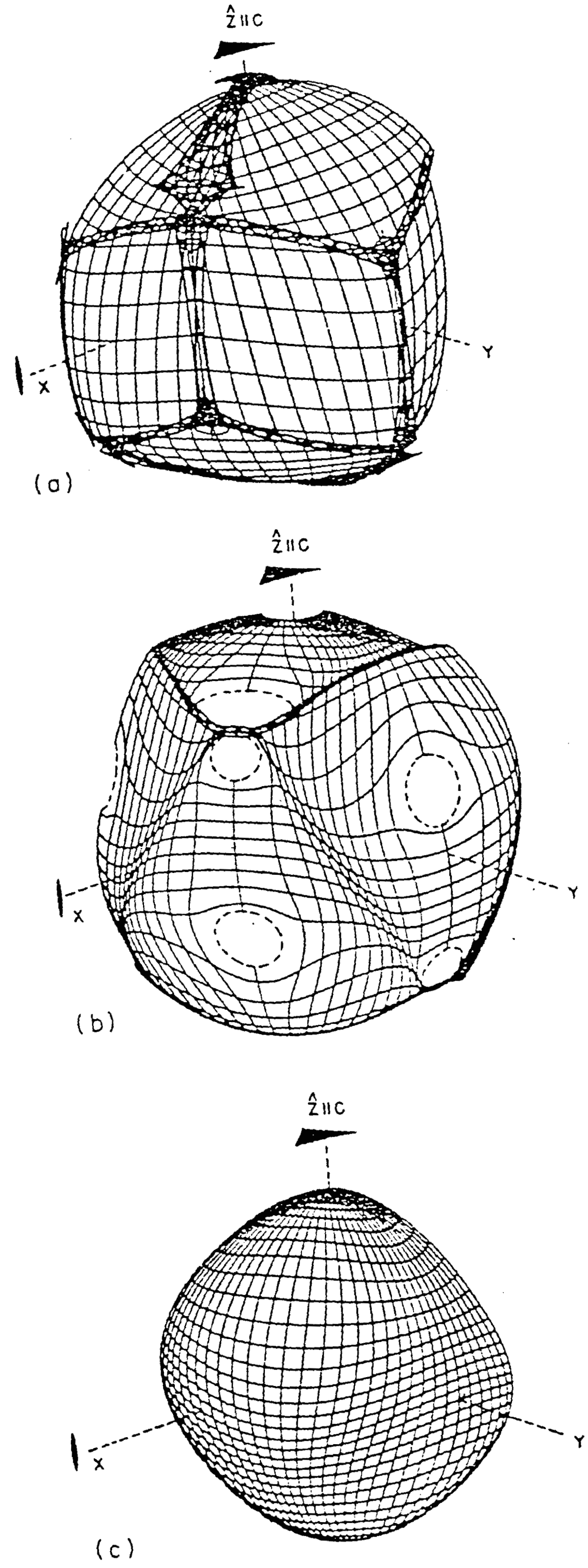

Fig. 2.3

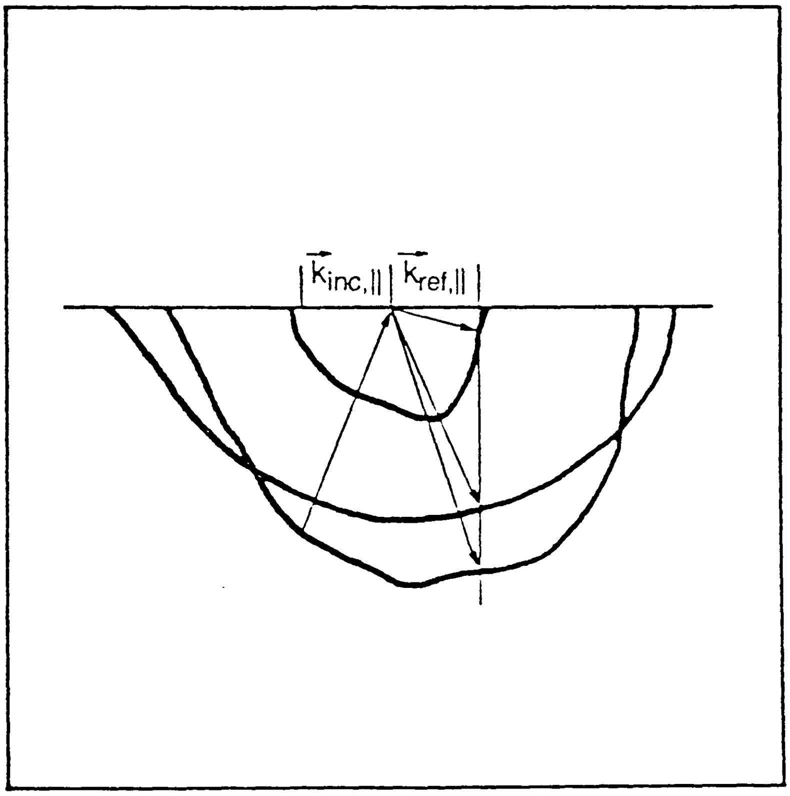

Fig. 2.4

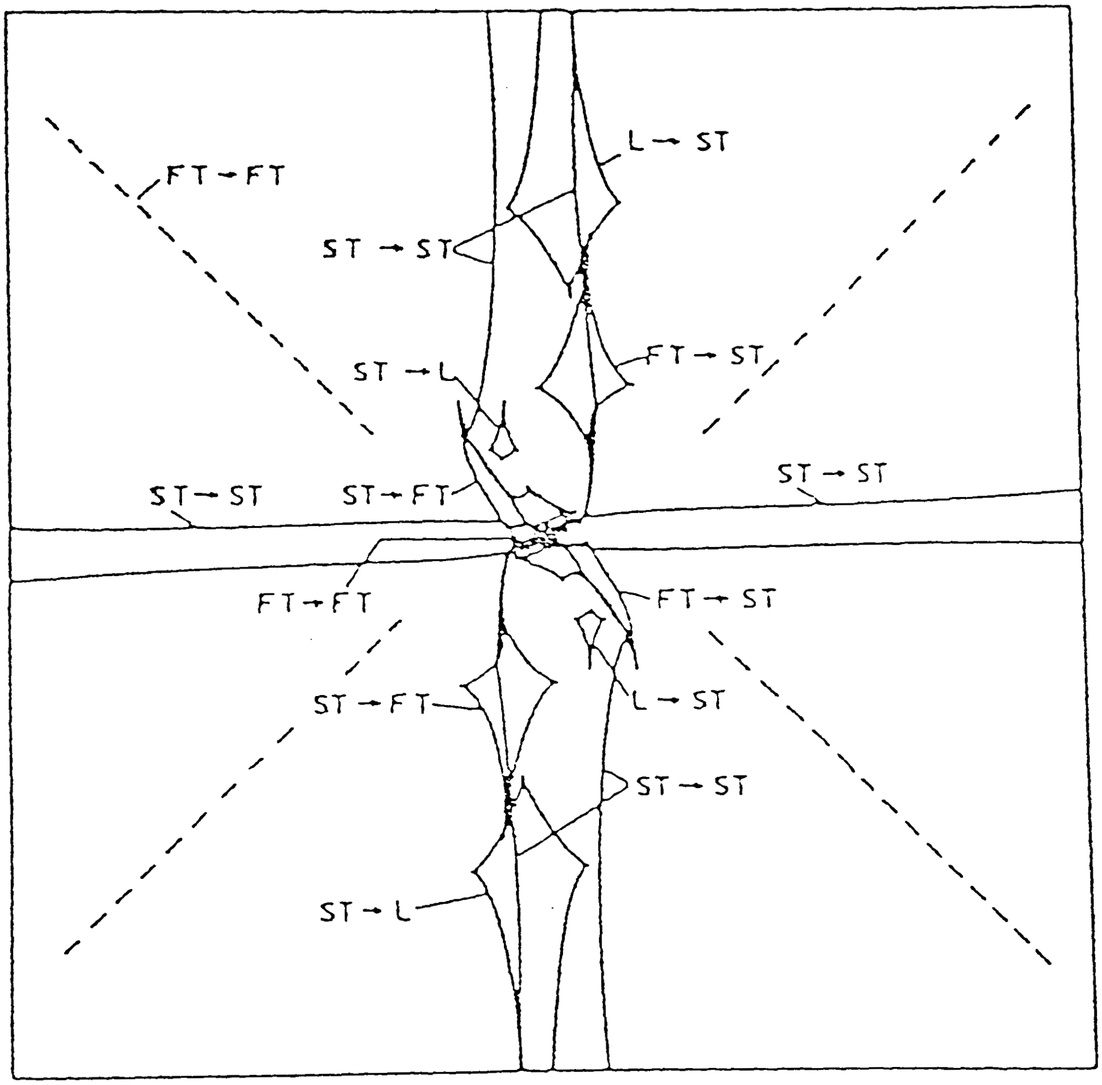
L → ST
FT → FT
ST → ST
FT → ST
ST → L
ST → ST
ST → FT
ST → ST
FT → FT
FT → ST
ST → FT
L → ST
ST → ST
ST → L

Fig. 2.5

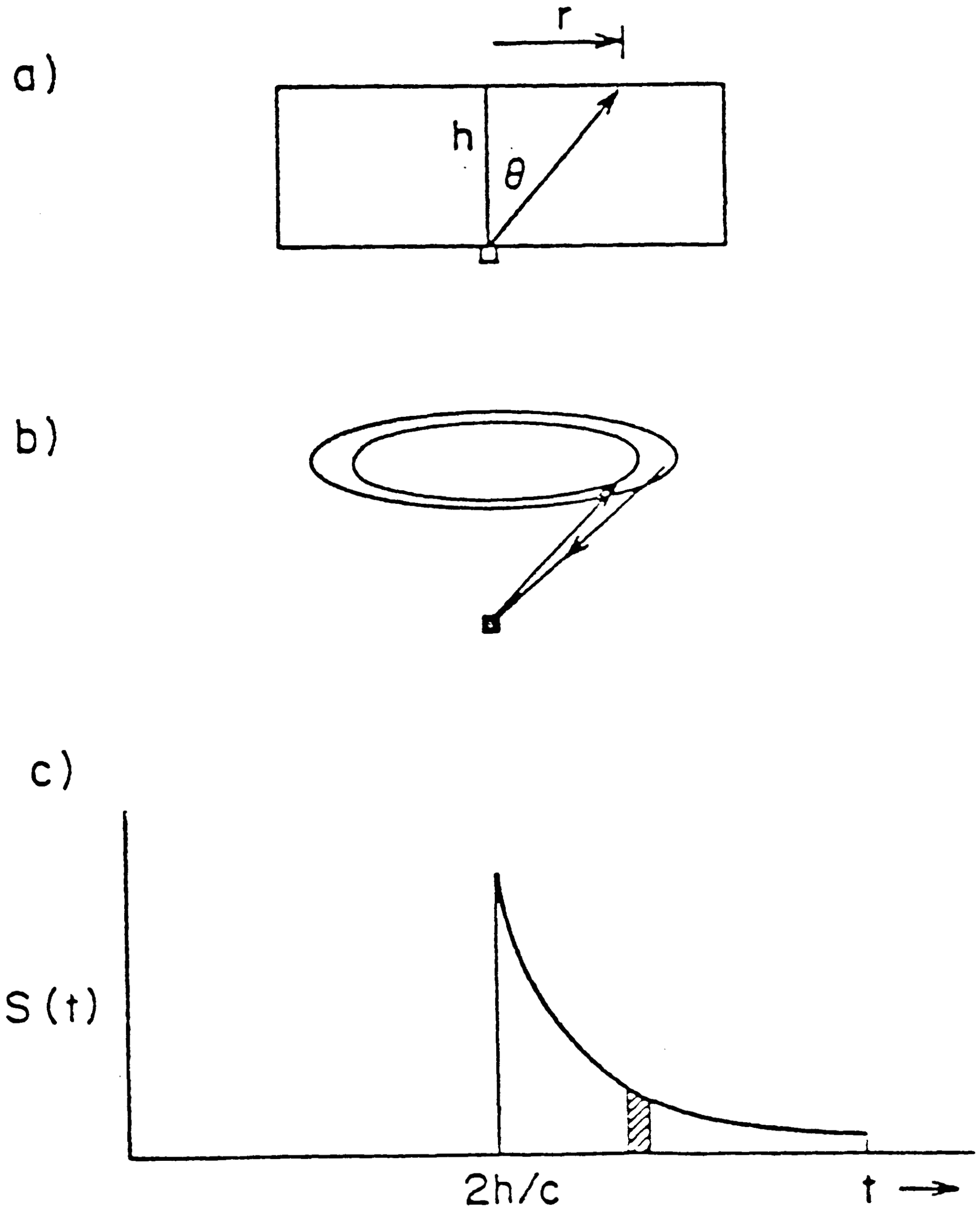

Fig. 2.6

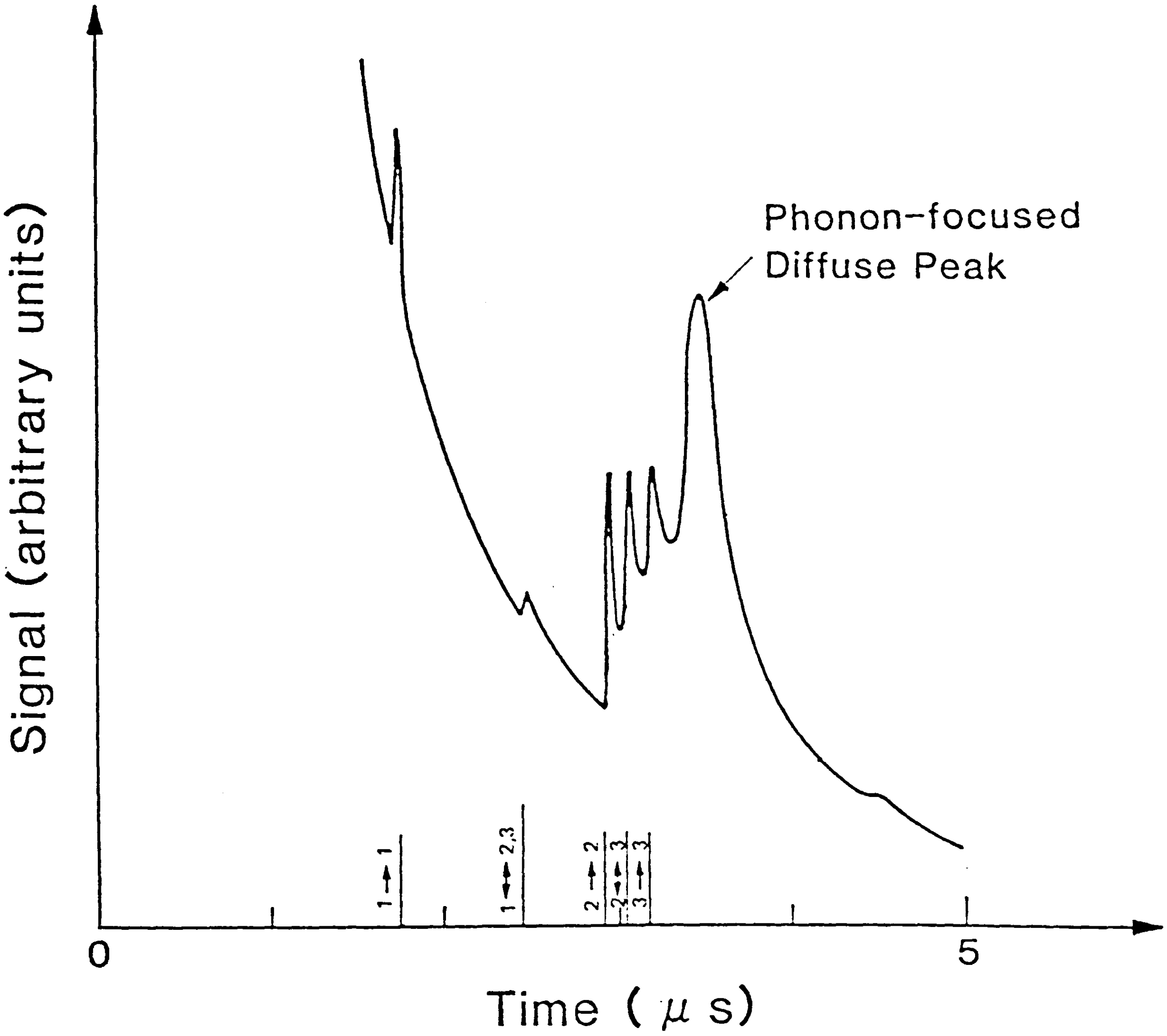
Signal (arbitrary units)
Phonon-focused
Diffuse Peak
1 → 1
1 ↔ 2,3
2 → 2
2 ↔ 3
3 → 3
0
5
Time (μ s)

Fig. 2.7

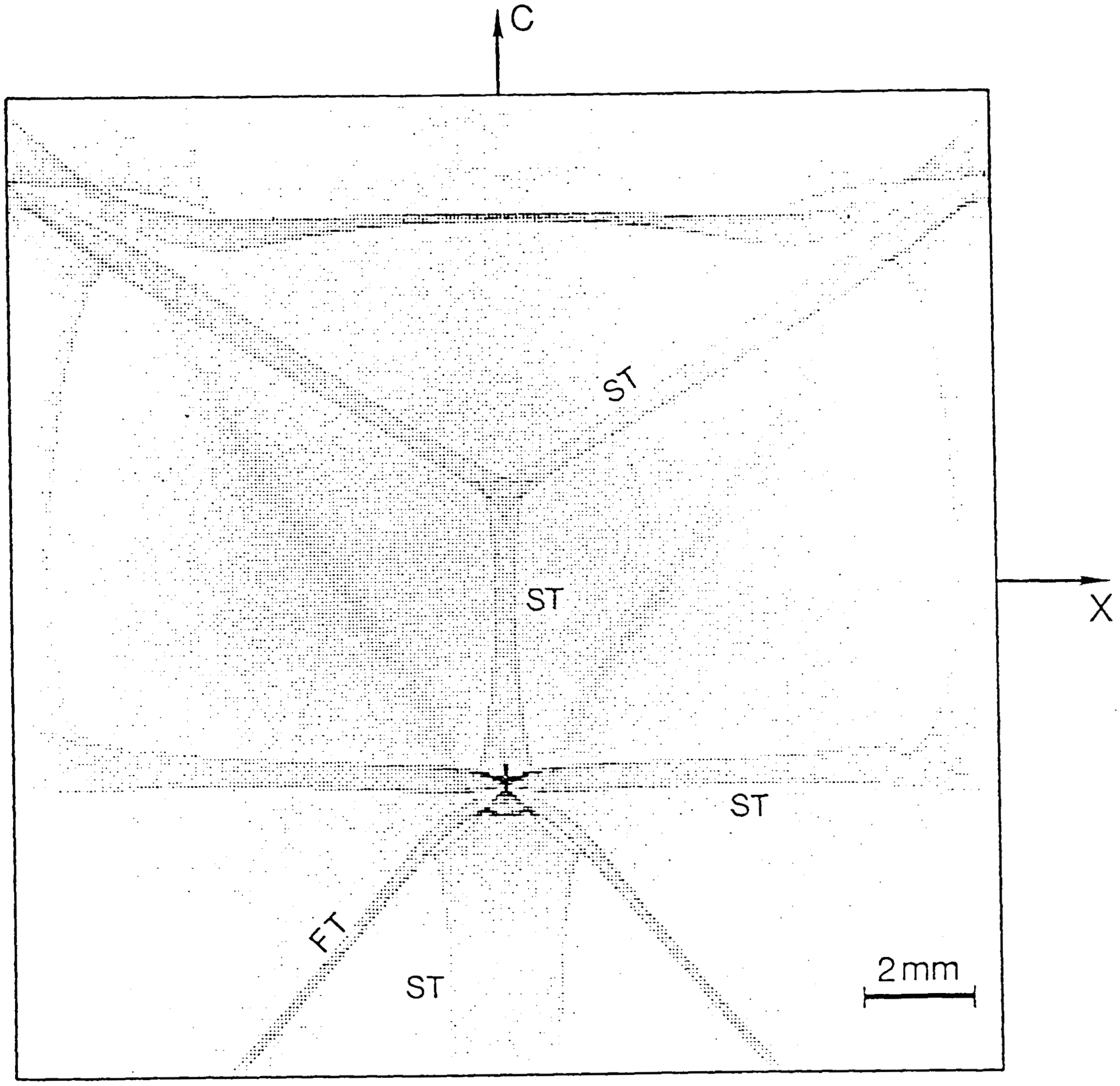

Fig. 2.8a

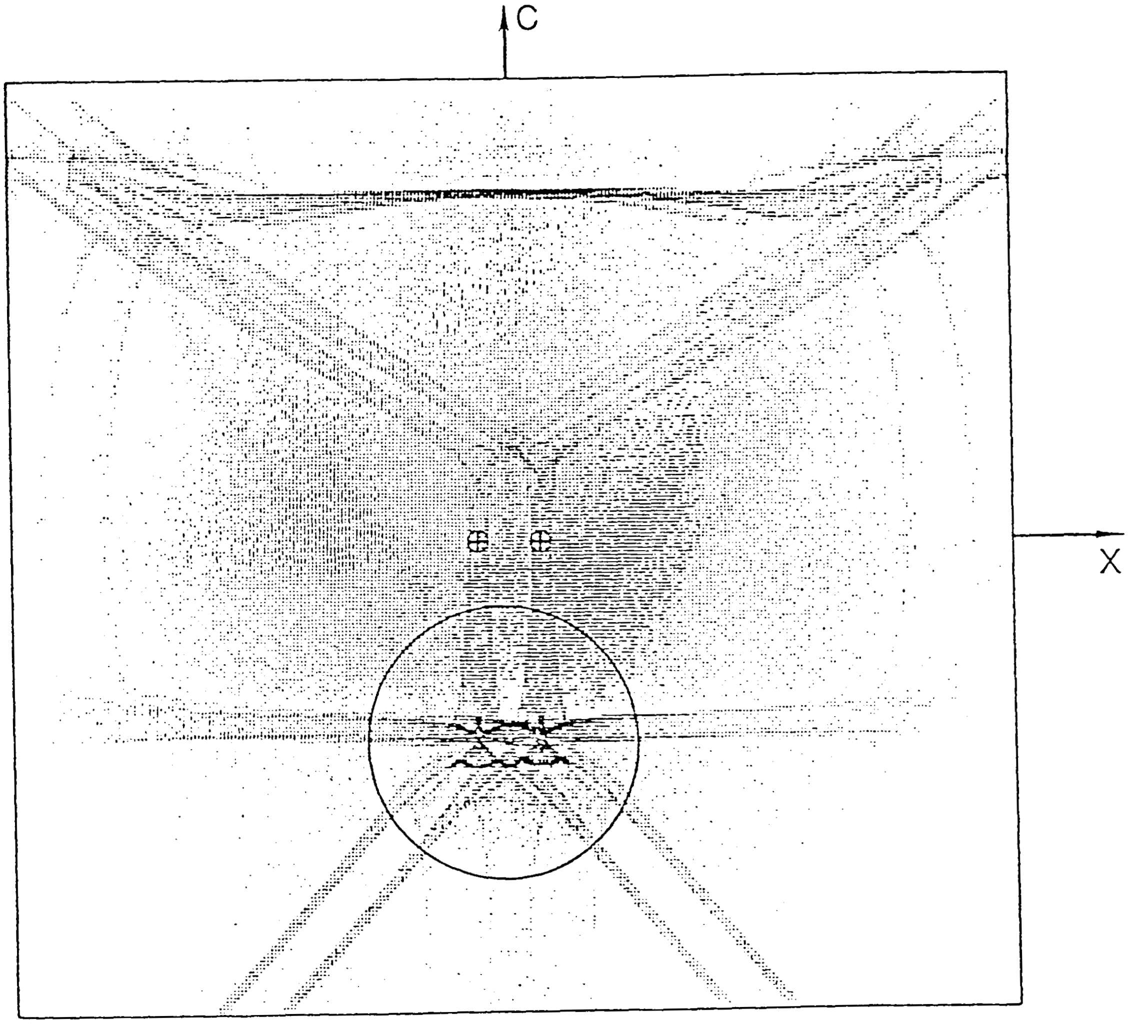

Fig. 2.8b

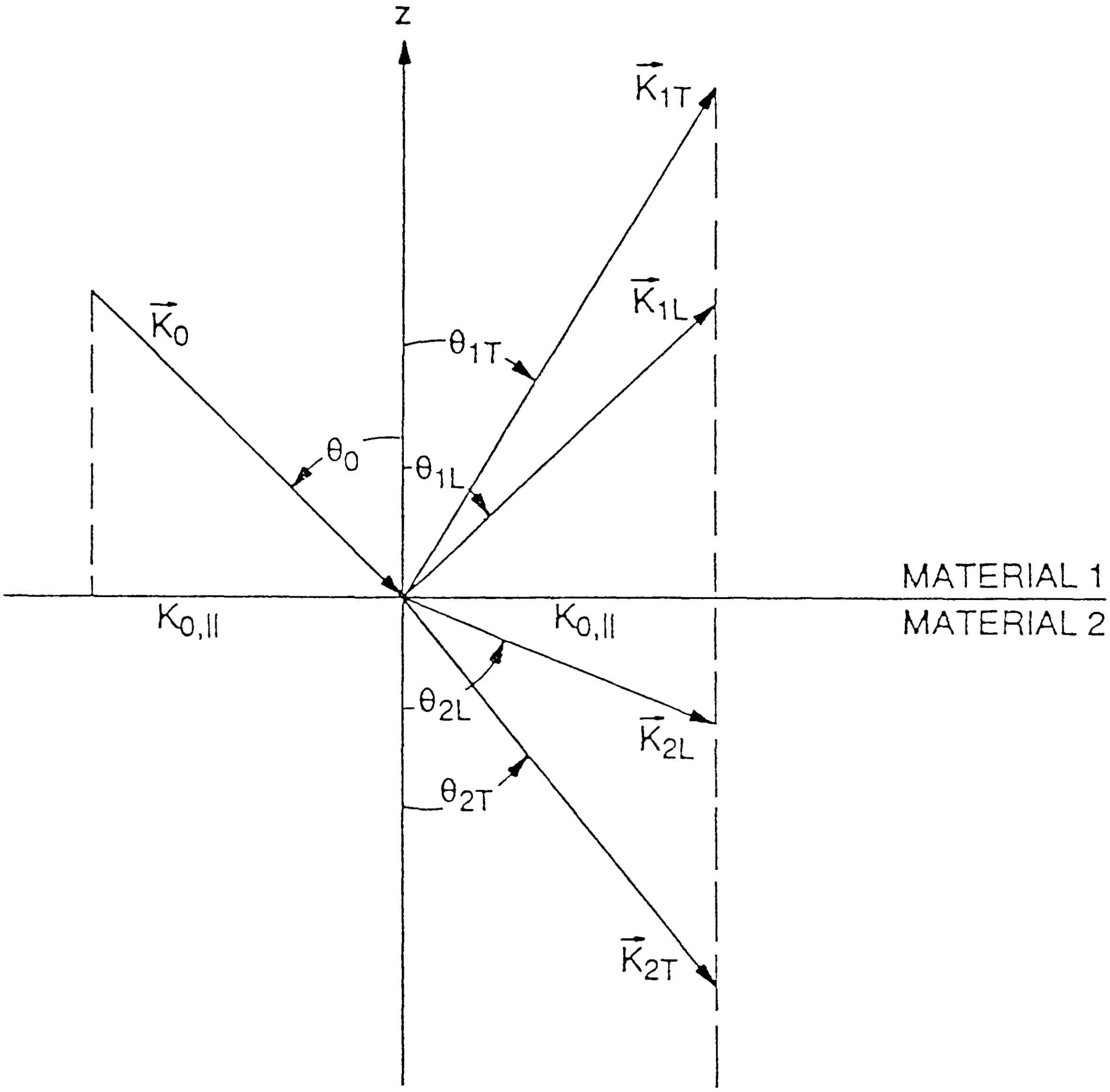
z
$\vec{K}_{1T}$
$\vec{K}_{1L}$
$\vec{K}_0$
θ_{1T}
θ_0
θ_{1L}
MATERIAL 1
MATERIAL 2
$K_{0,\parallel}$
$K_{0,\parallel}$
θ_{2L}
$\vec{K}_{2L}$
θ_{2T}
$\vec{K}_{2T}$

Fig. 2.9

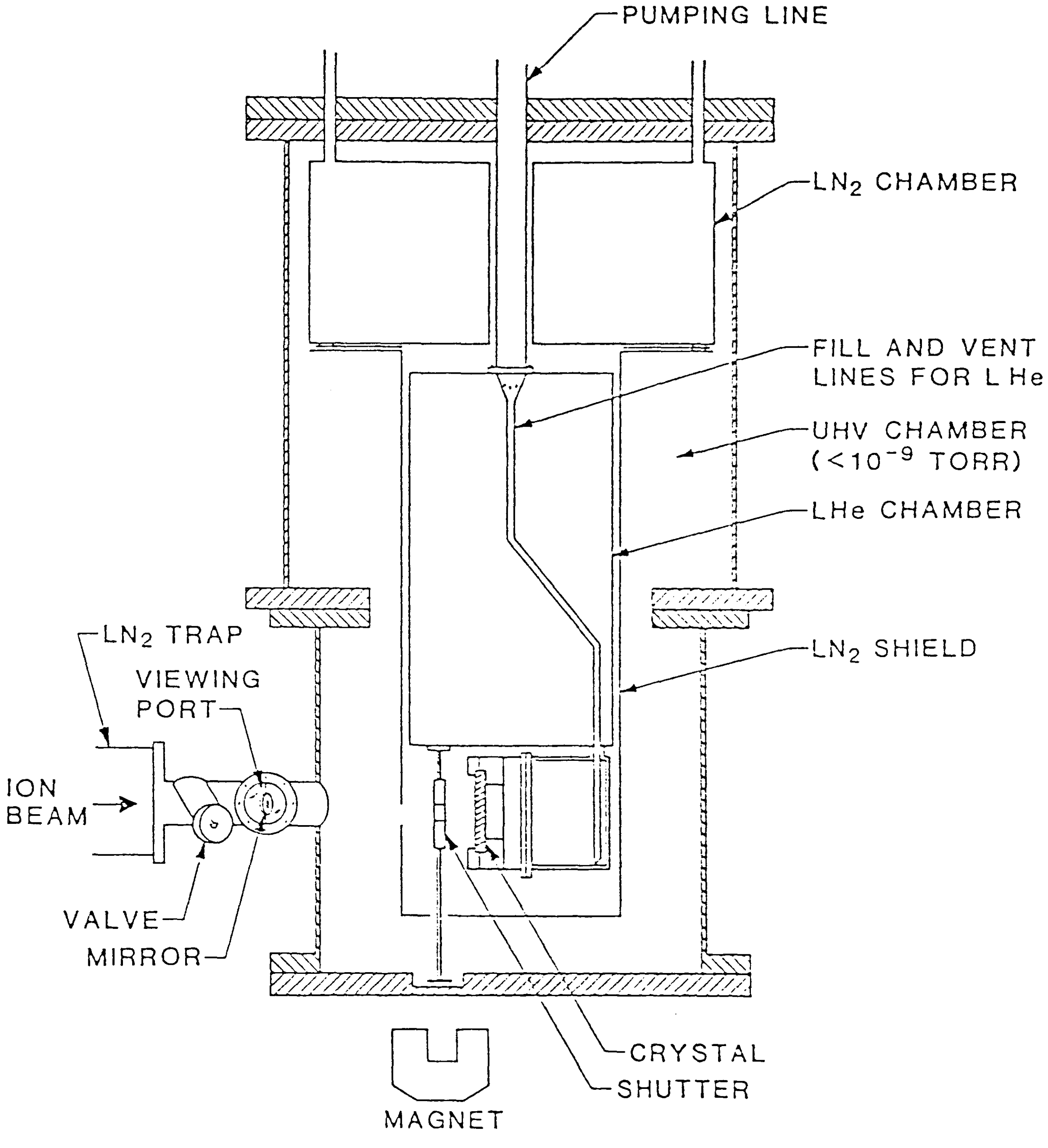
PUMPING LINE
LN$_2$ CHAMBER
FILL AND VENT LINES FOR L He
UHV CHAMBER (<10^{-9} TORR)
LHe CHAMBER
LN$_2$ SHIELD
LN$_2$ TRAP
VIEWING PORT
ION BEAM
VALVE
MIRROR
CRYSTAL
SHUTTER
MAGNET

Fig. 4.1

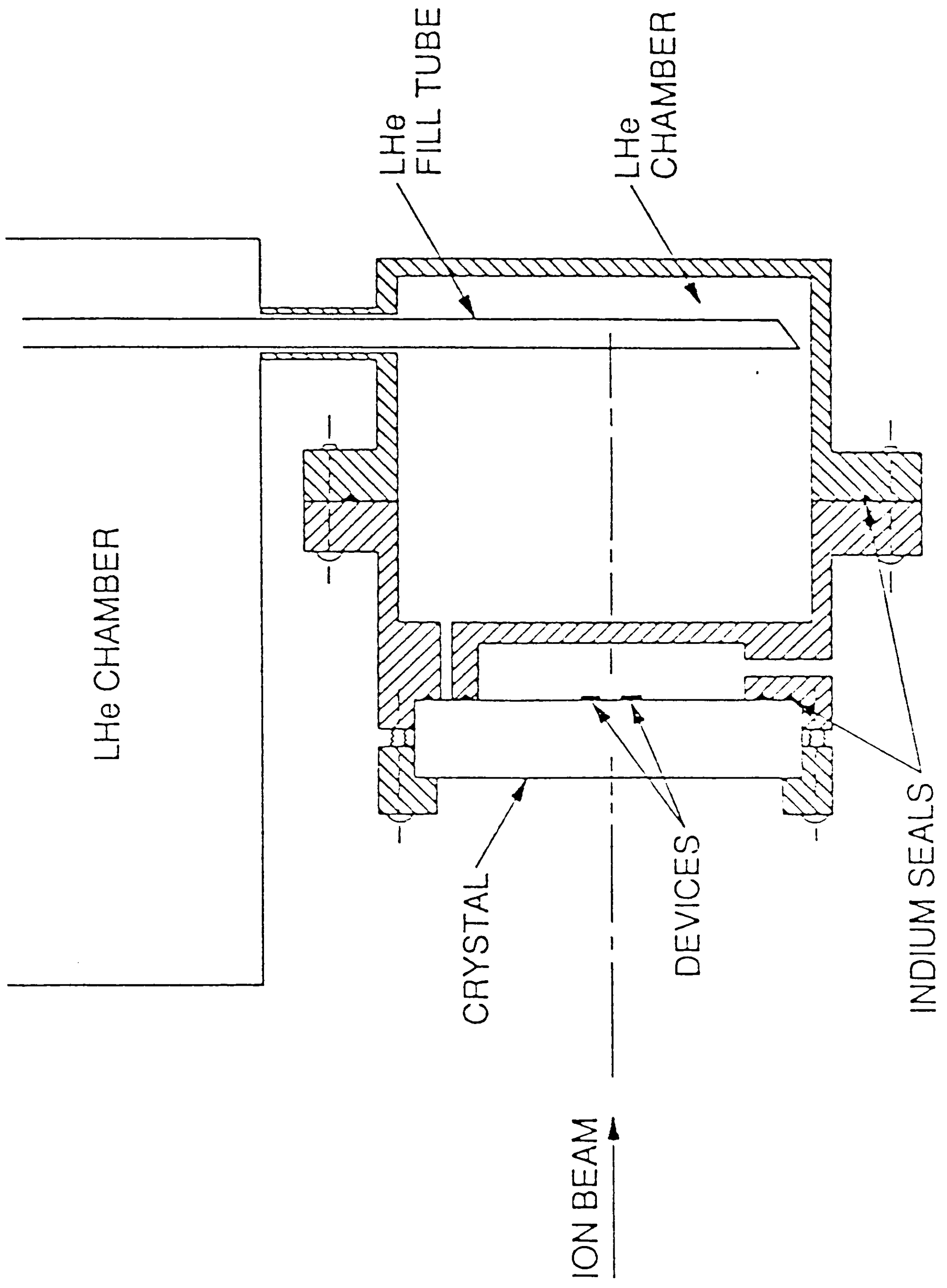
LHe
FILL TUBE
LHe
CHAMBER
LHe CHAMBER
CRYSTAL
DEVICES
INDIUM SEALS
ION BEAM

Fig. 4.2a

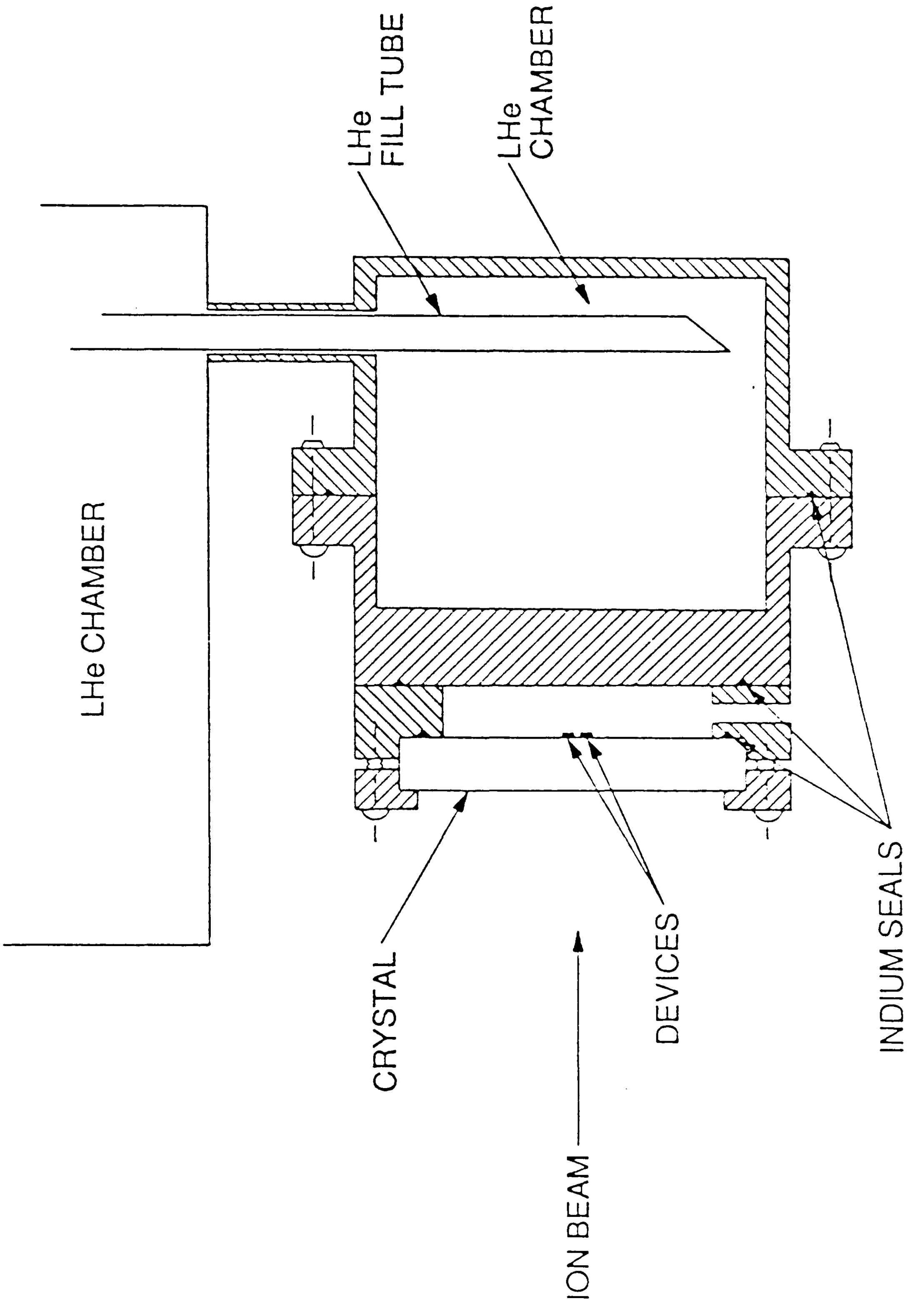
LHe CHAMBER
LHe FILL TUBE
LHe CHAMBER
CRYSTAL
ION BEAM
DEVICES
INDIUM SEALS

Fig. 4.2b

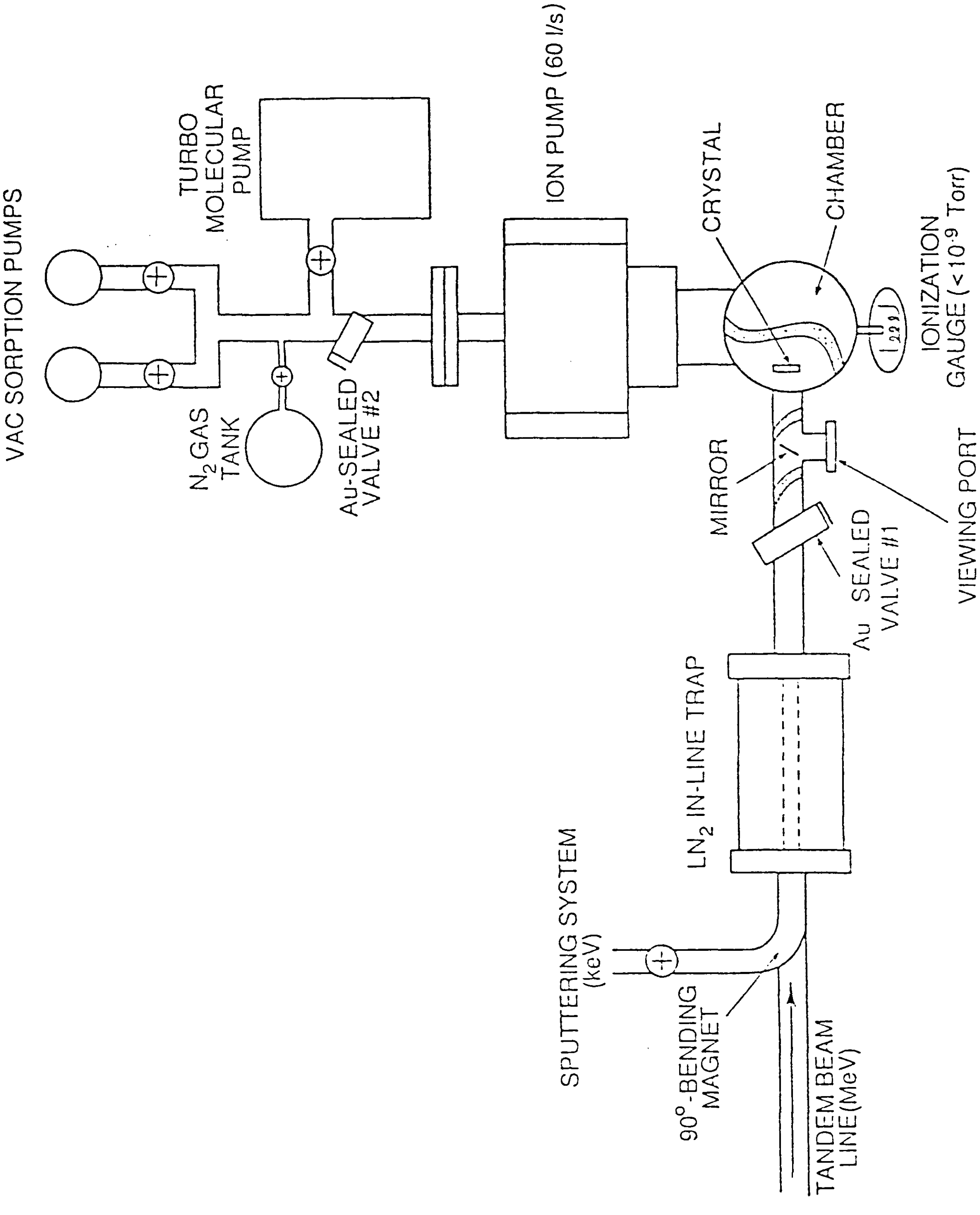
VAC SORPTION PUMPS
TURBO MOLECULAR PUMP
ION PUMP (60 l/s)
CRYSTAL
CHAMBER
IONIZATION GAUGE ($<10^{-9}$ Torr)
N_2 GAS TANK
Au-SEALED VALVE #2
MIRROR
VIEWING PORT
Au SEALED VALVE #1
LN_2 IN-LINE TRAP
SPUTTERING SYSTEM (keV)
90°-BENDING MAGNET
TANDEM BEAM LINE (MeV)

Fig. 4.3

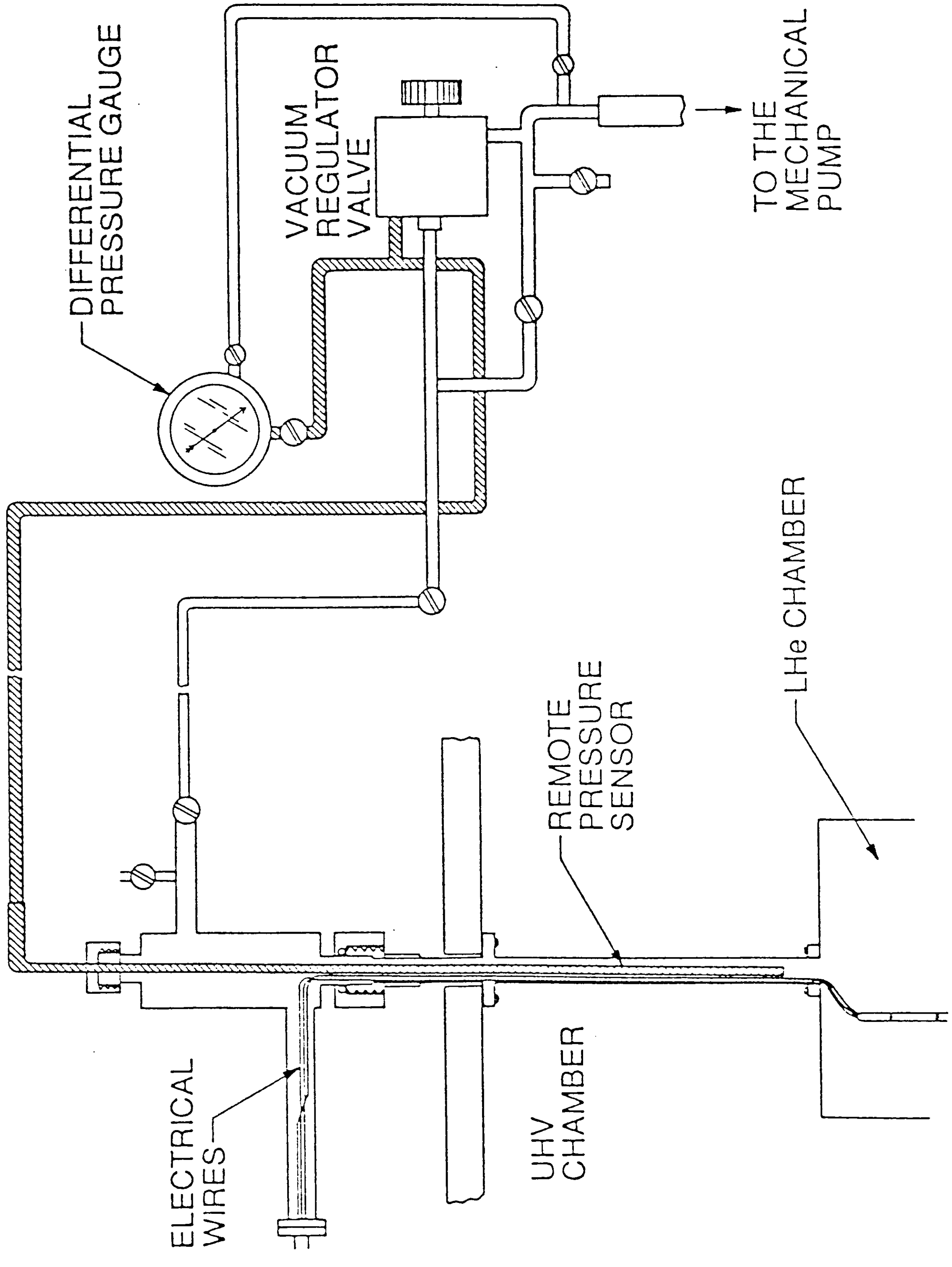
DIFFERENTIAL PRESSURE GAUGE
VACUUM REGULATOR VALVE
TO THE MECHANICAL PUMP
LHe CHAMBER
REMOTE PRESSURE SENSOR
ELECTRICAL WIRES
UHV CHAMBER

Fig. 4.4

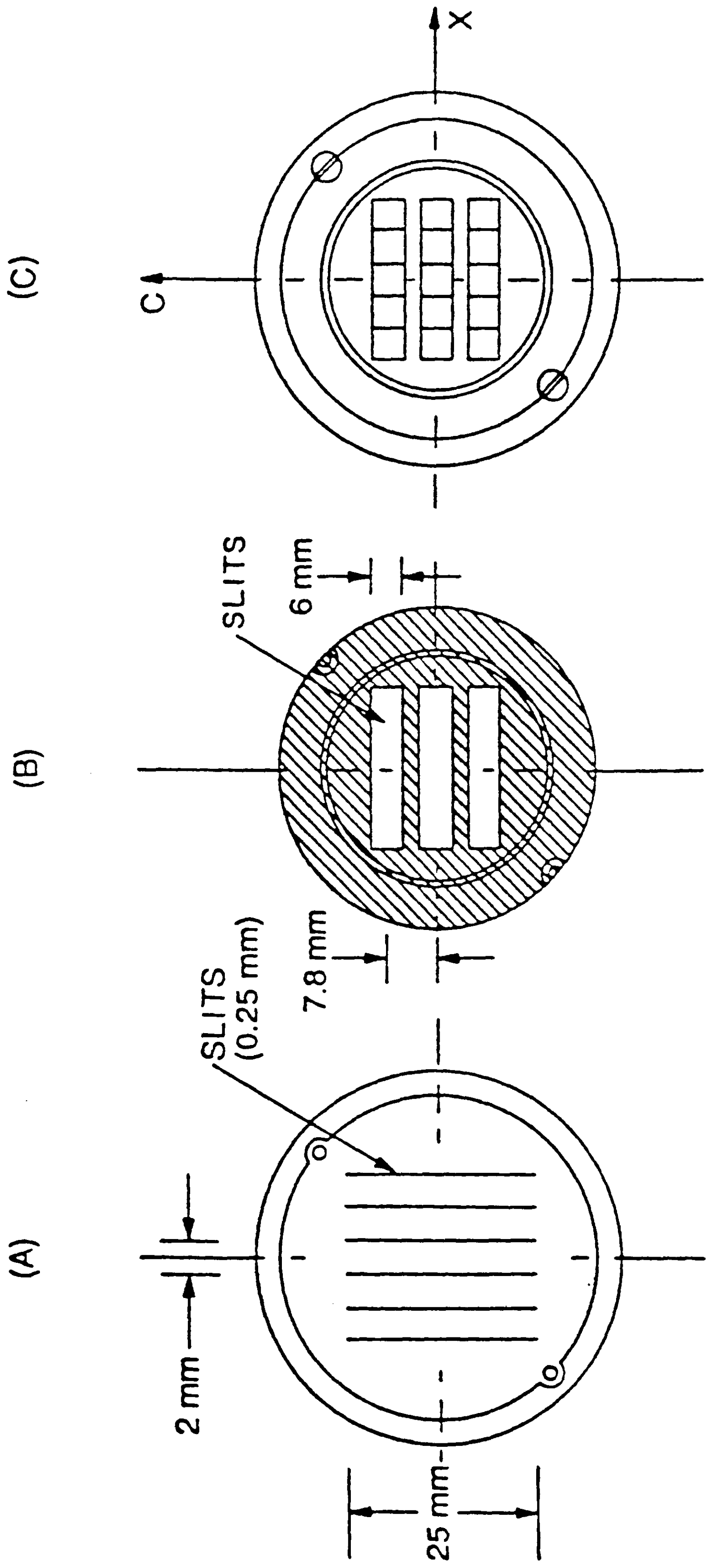

Fig. 4.5

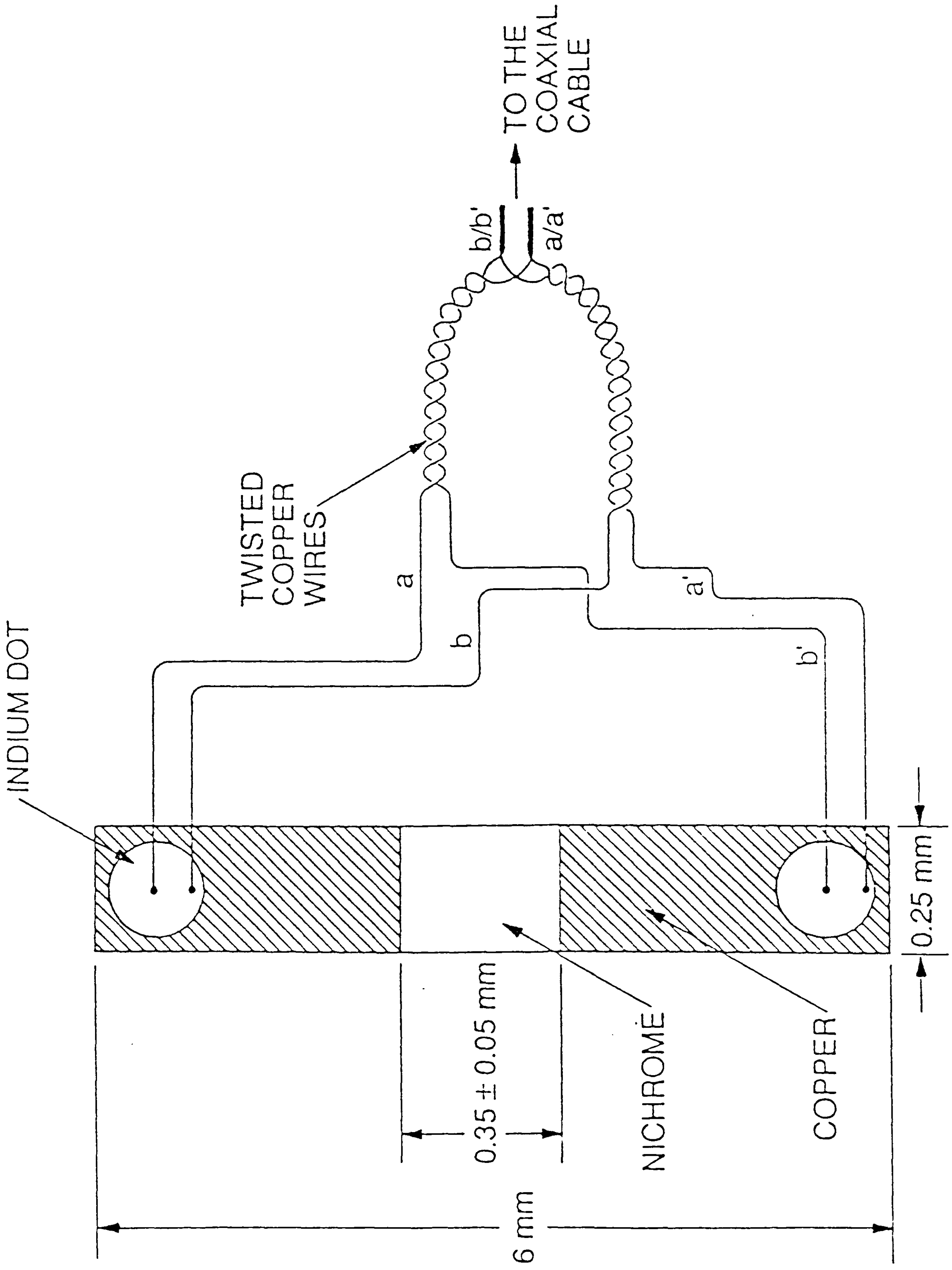
INDIUM DOT
TWISTED COPPER WIRES
a
b
a'
b'
b/b'
a/a'
TO THE COAXIAL CABLE
0.25 mm
0.35 ± 0.05 mm
NICHROME
COPPER
6 mm

Fig. 4.6a

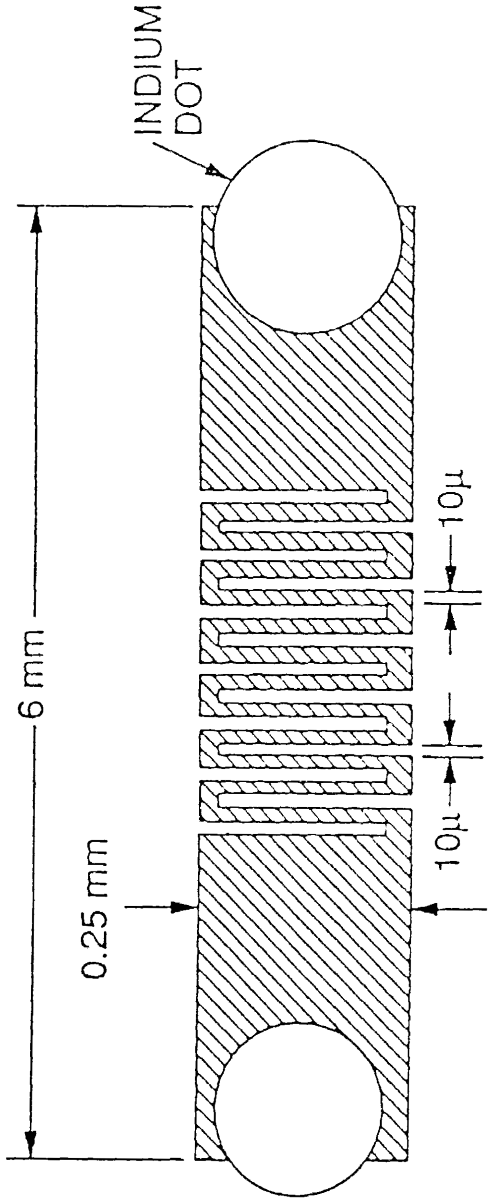

Fig. 4.6b

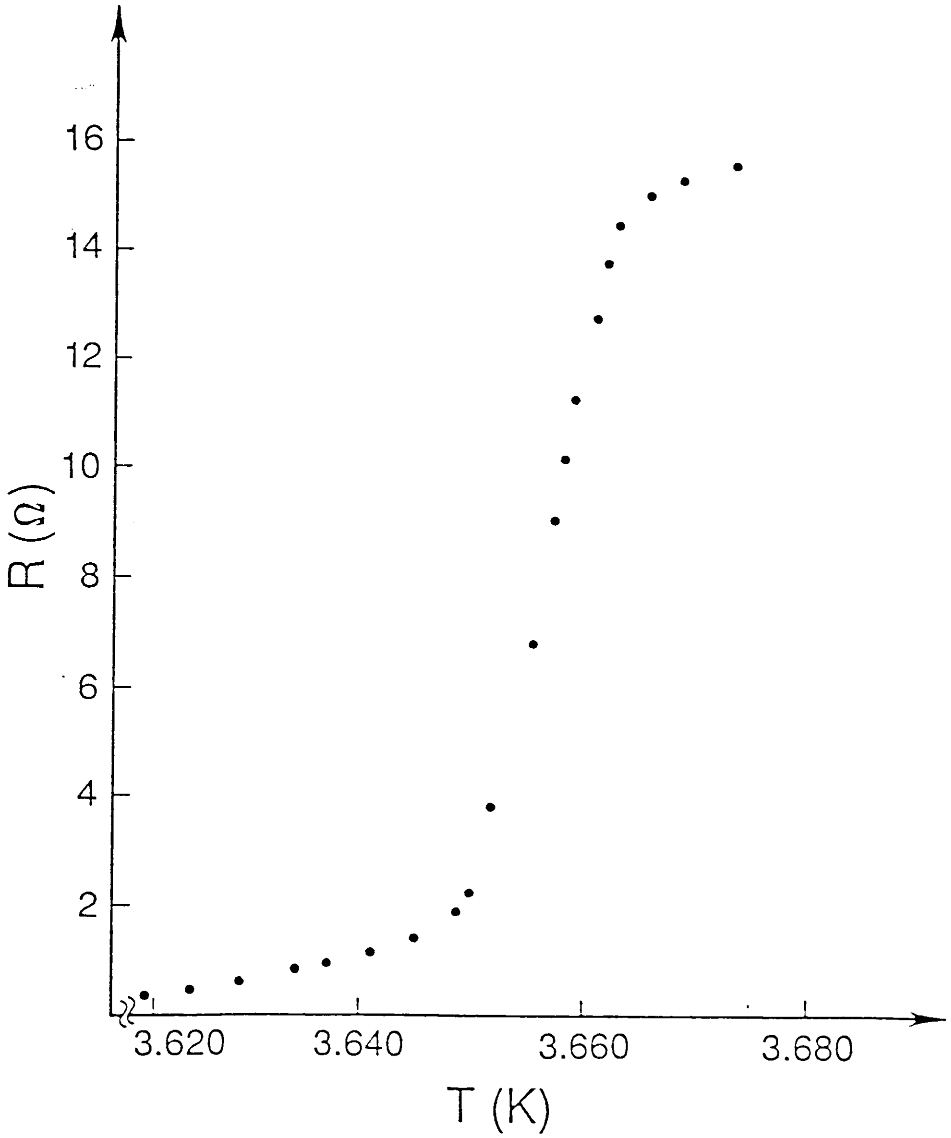

Fig. 4.7

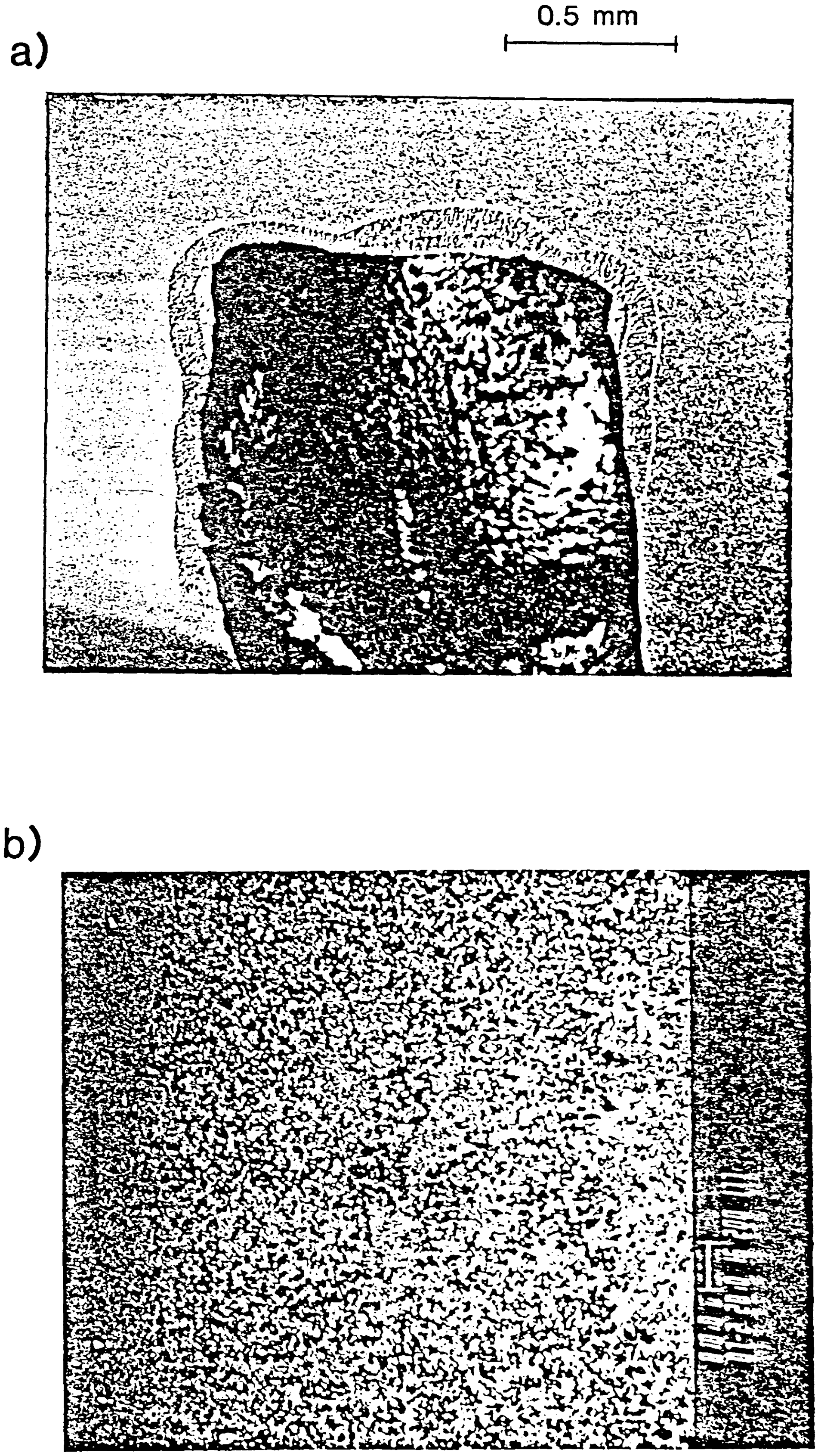

Fig. 4.8

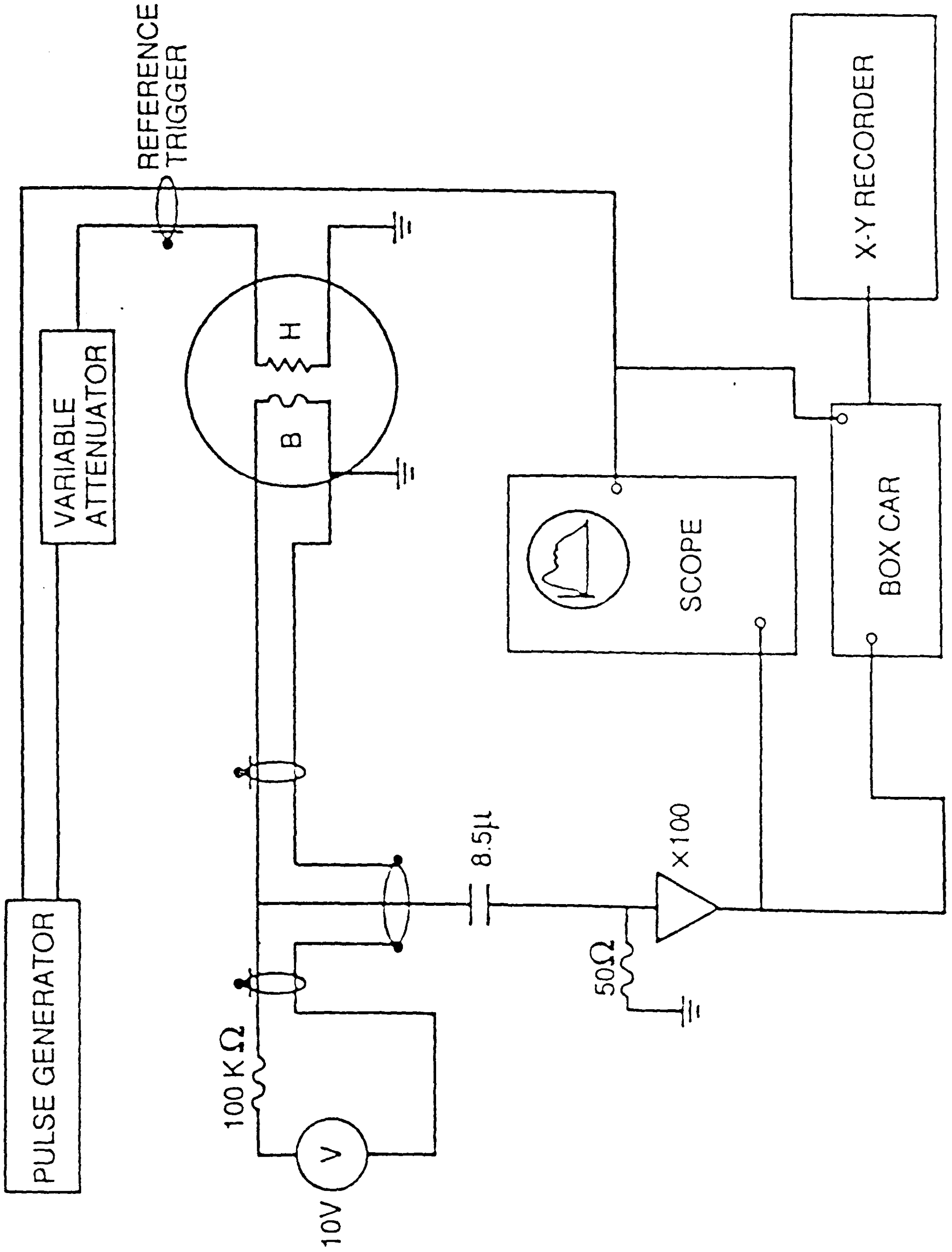
REFERENCE TRIGGER
X-Y RECORDER
VARIABLE ATTENUATOR
H
B
SCOPE
BOX CAR
8.5μ
×100
50Ω
PULSE GENERATOR
100 KΩ
V
10V

Fig. 4.9

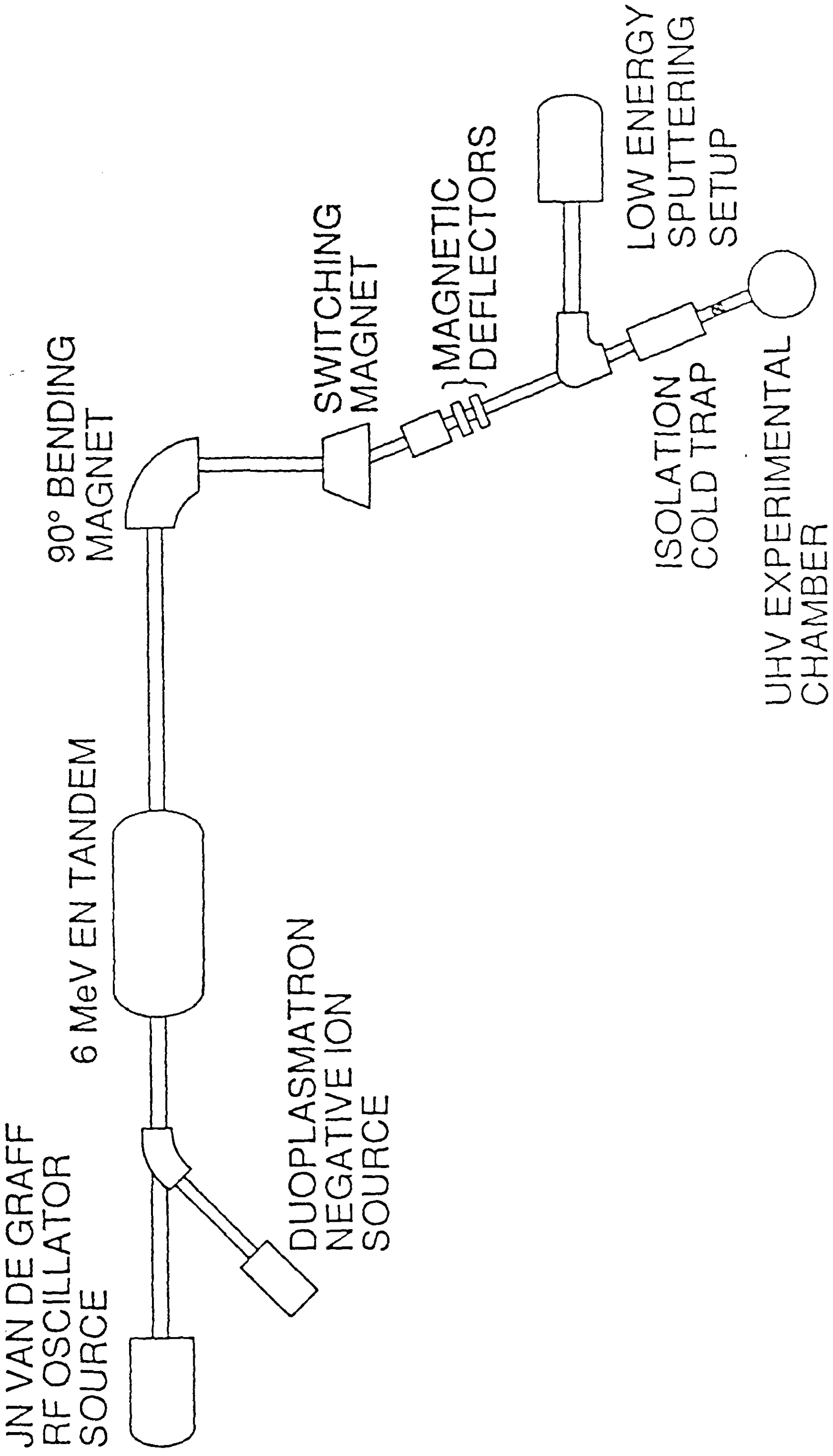
JN VAN DE GRAFF
RF OSCILLATOR
SOURCE
6 MeV EN TANDEM
DUOPLASMATRON
NEGATIVE ION
SOURCE
90° BENDING
MAGNET
SWITCHING
MAGNET
MAGNETIC
DEFLECTORS
LOW ENERGY
SPUTTERING
SETUP
ISOLATION
COLD TRAP
UHV EXPERIMENTAL
CHAMBER

Fig. 4.10

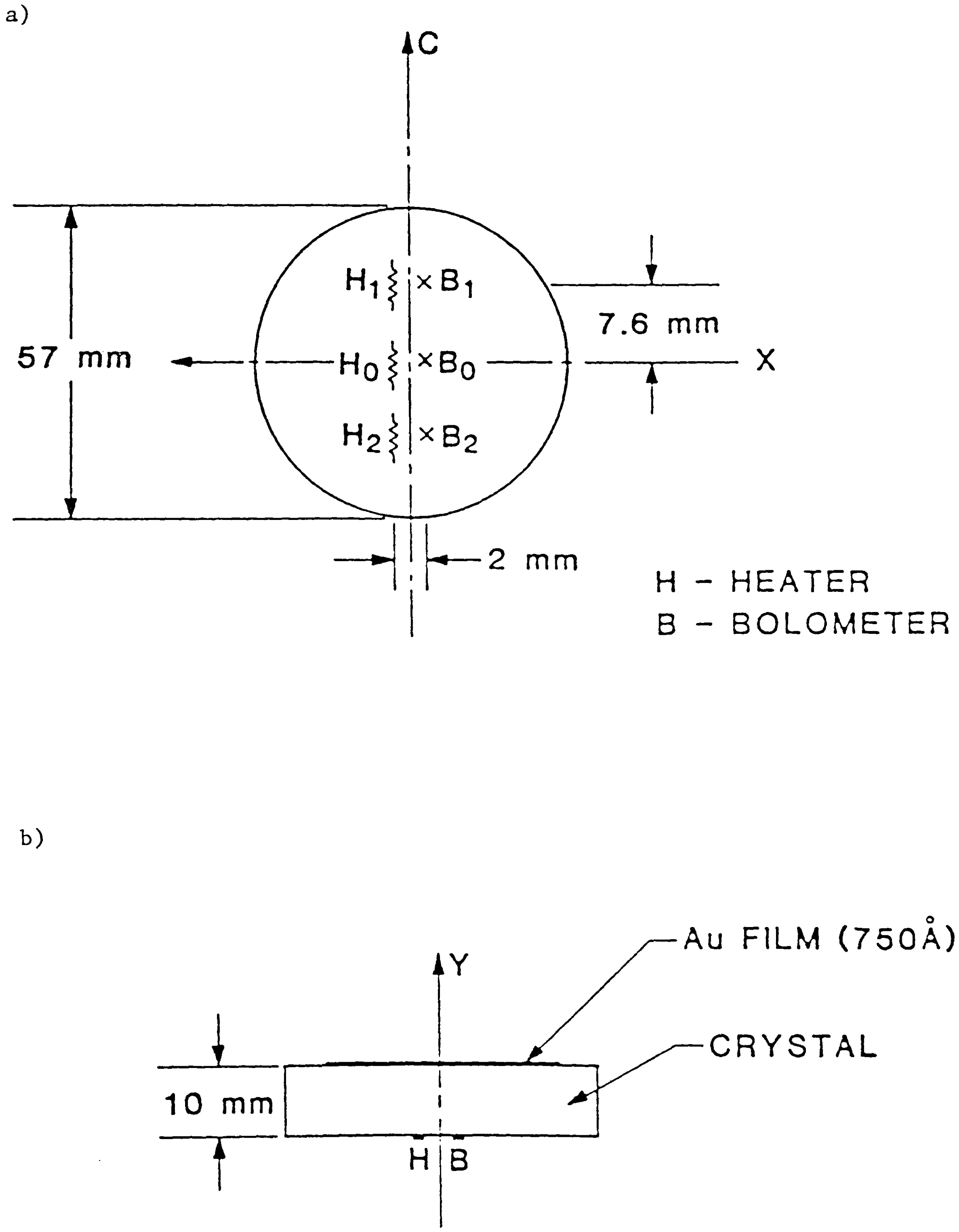
a)
C
H_1
$\times B_1$
7.6 mm
57 mm
H_0
$\times B_0$
X
H_2
$\times B_2$
2 mm
H - HEATER
B - BOLOMETER
b)
Au FILM (750Å)
Y
CRYSTAL
10 mm
H
B

Fig. 5.1

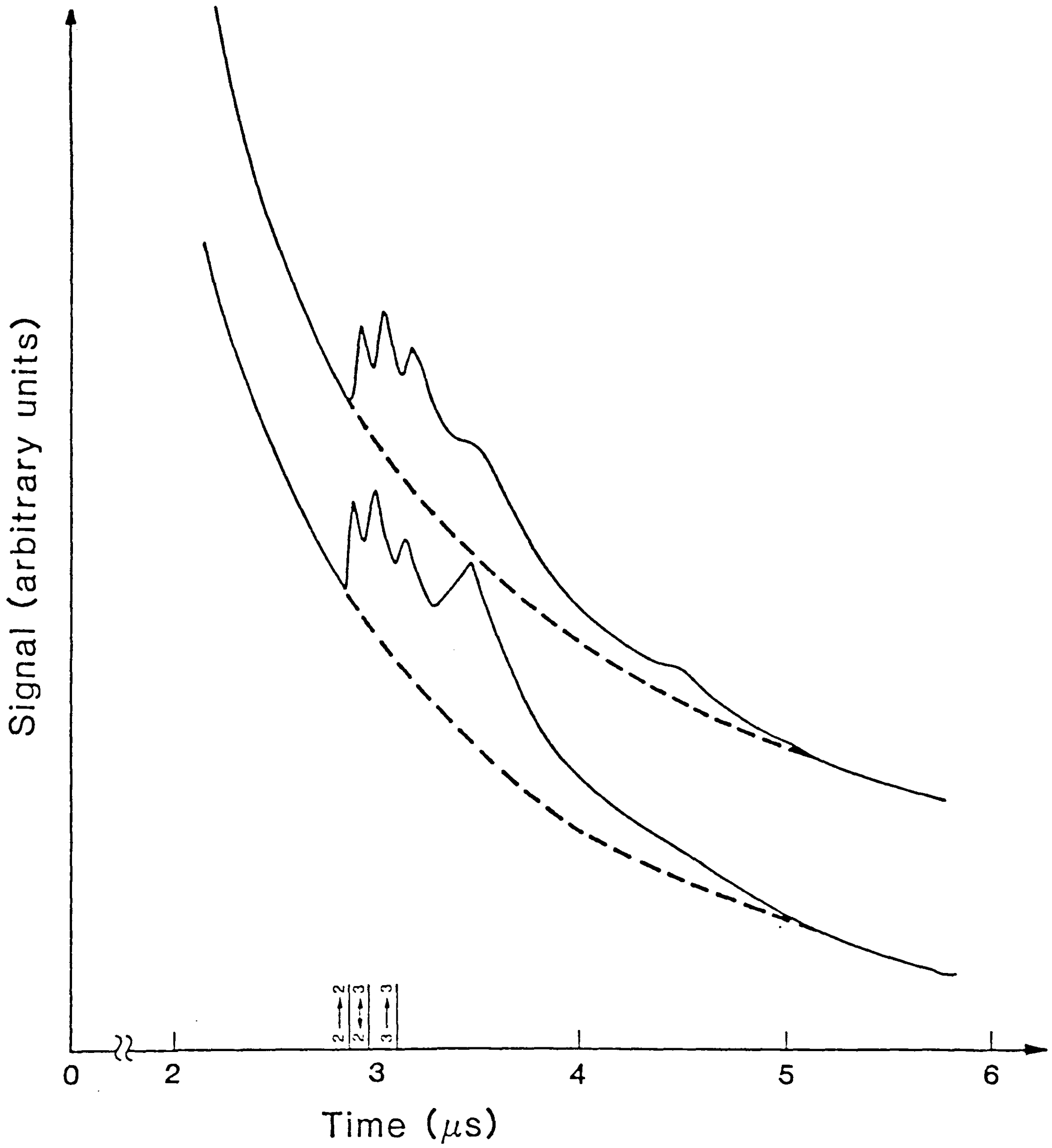

Fig. 5.2

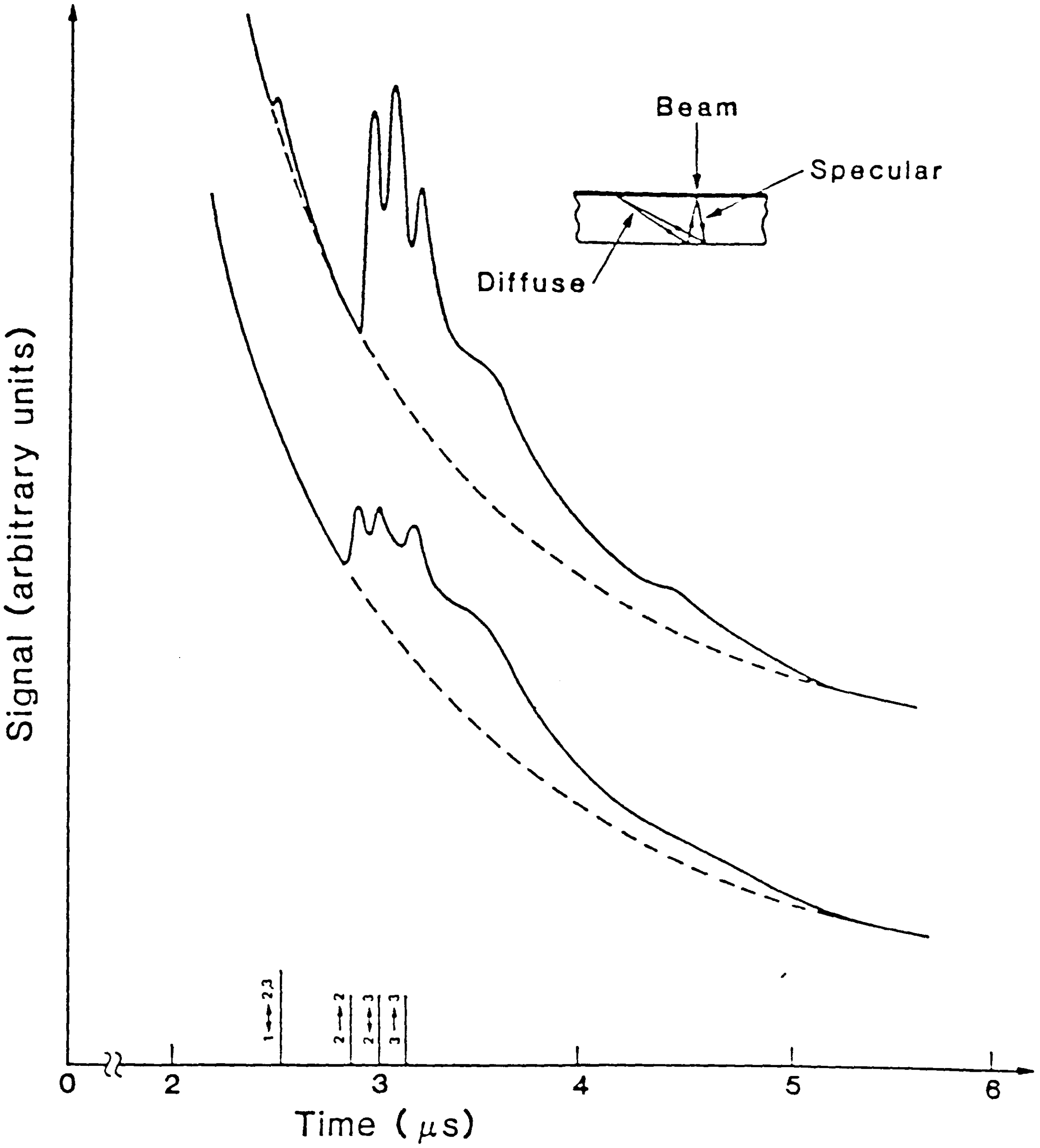
Beam
Specular
Diffuse
Signal (arbitrary units)
1↔2,3
2→2
2↔3
3→3
0
2
3
4
5
6
Time (μs)

Fig. 5.3a

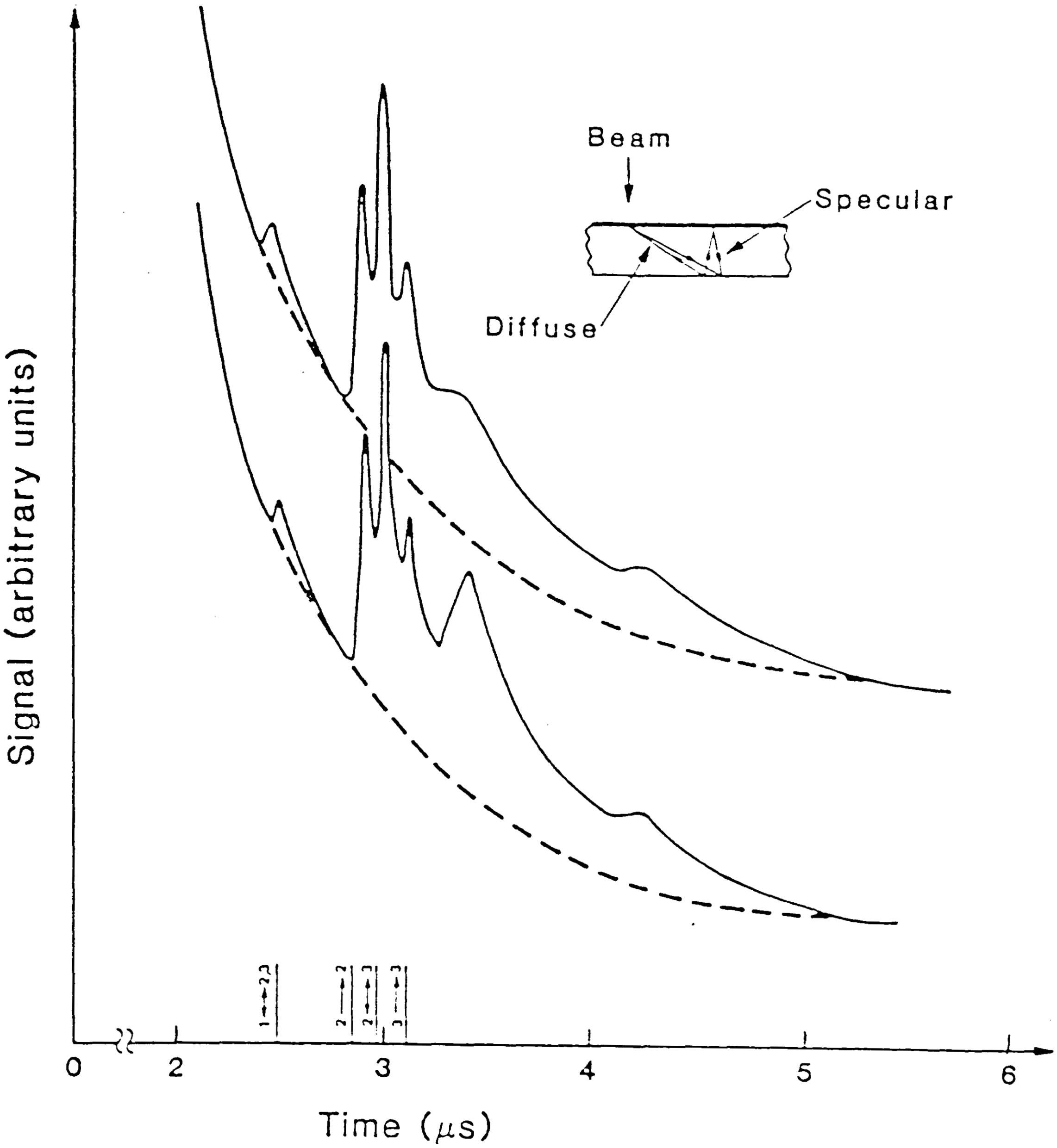
Beam
Specular
Diffuse
Signal (arbitrary units)
1↔2
2↔2
2↔3
3↔3
0
2
3
4
5
6
Time (μs)

Fig. 5.3b

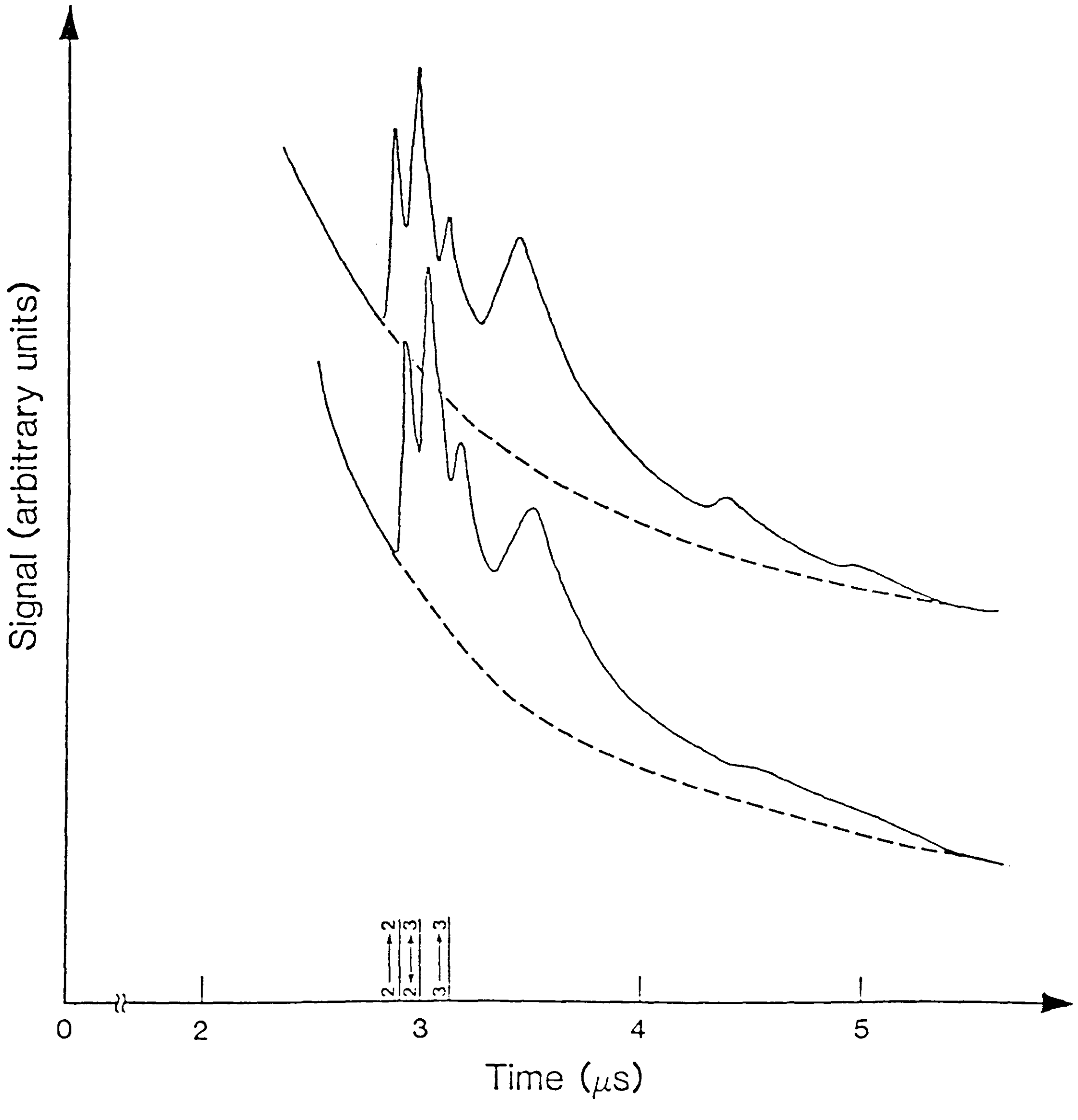

Fig. 5.4

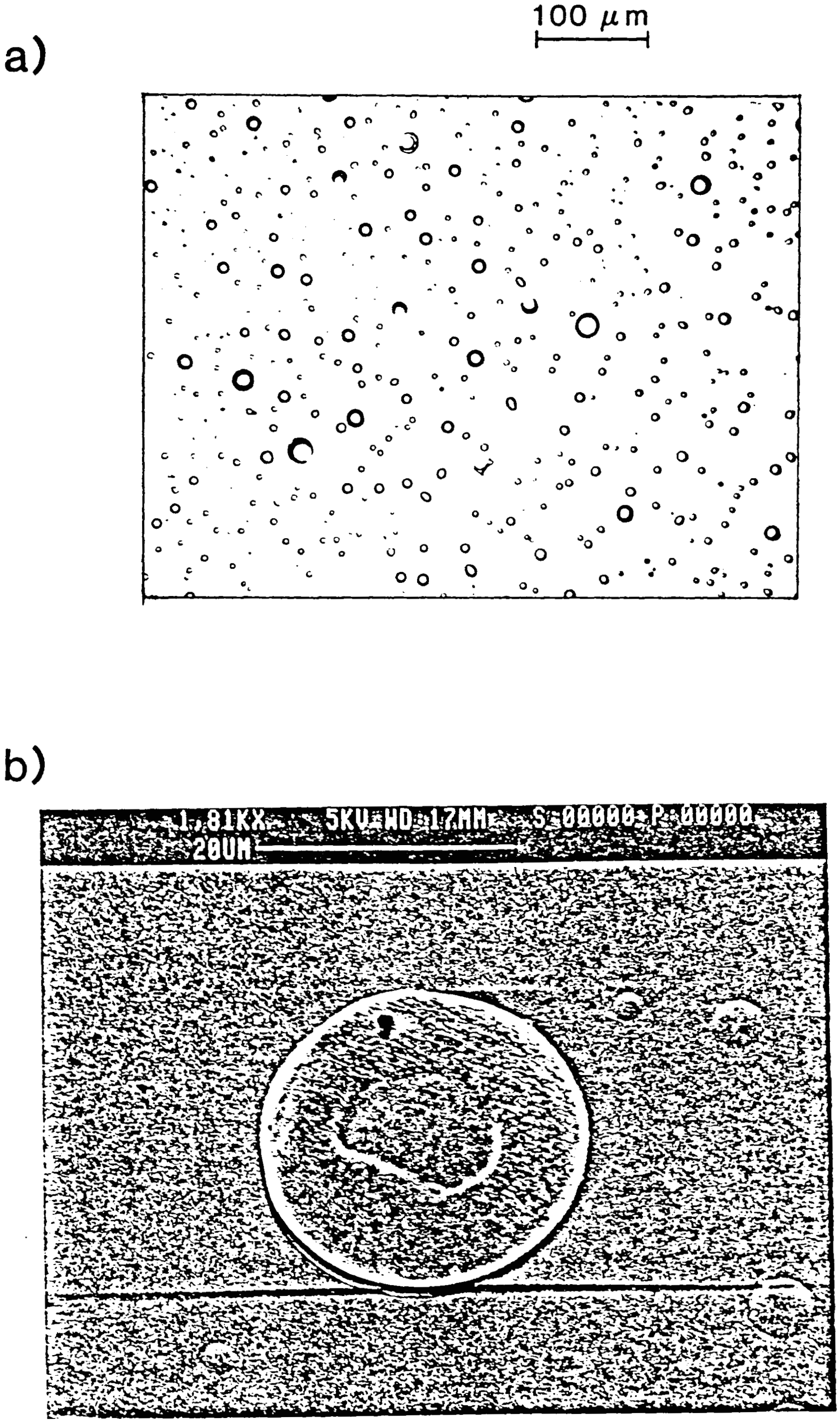

Fig. 5.5

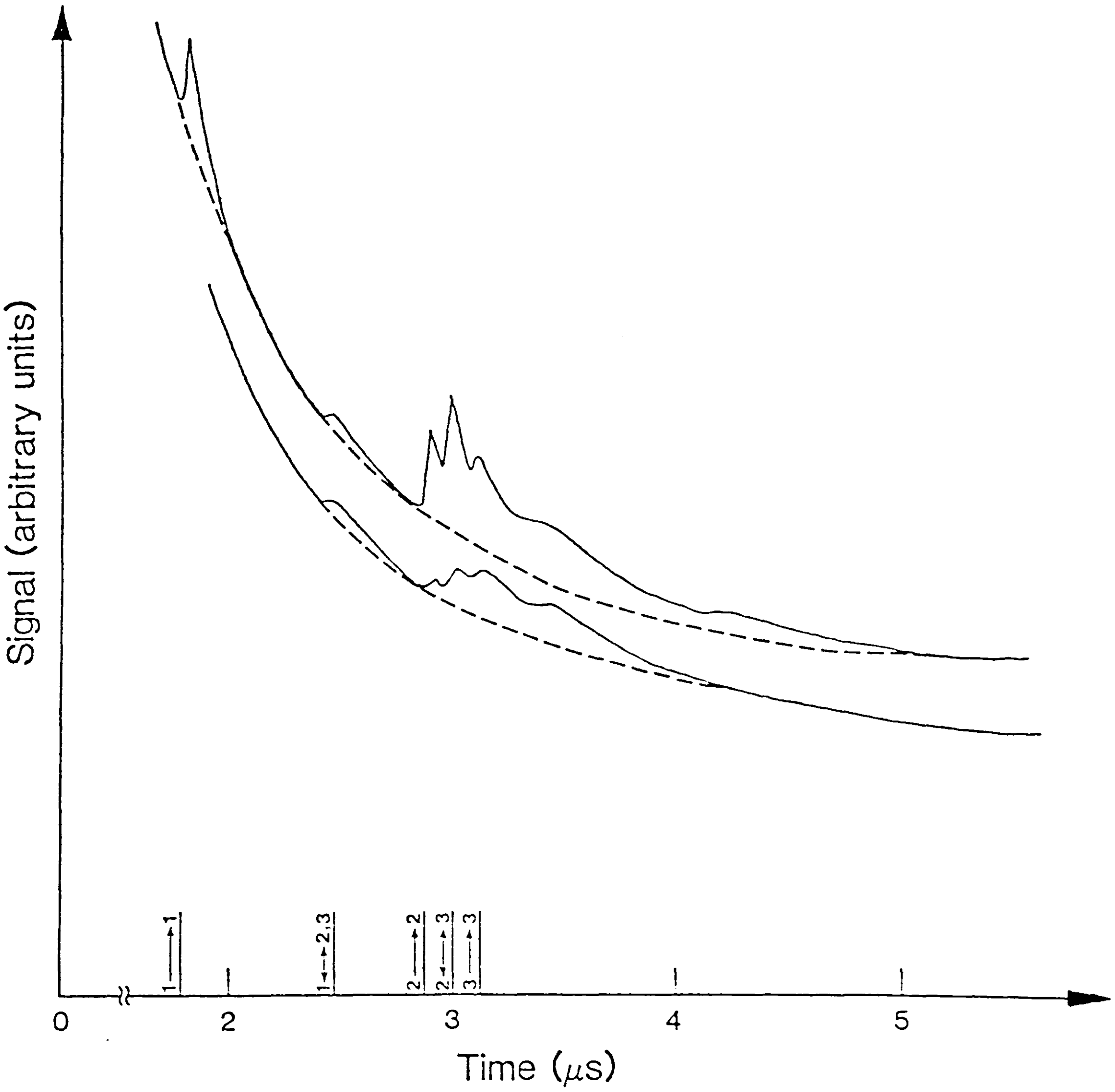

Fig. 5.6a

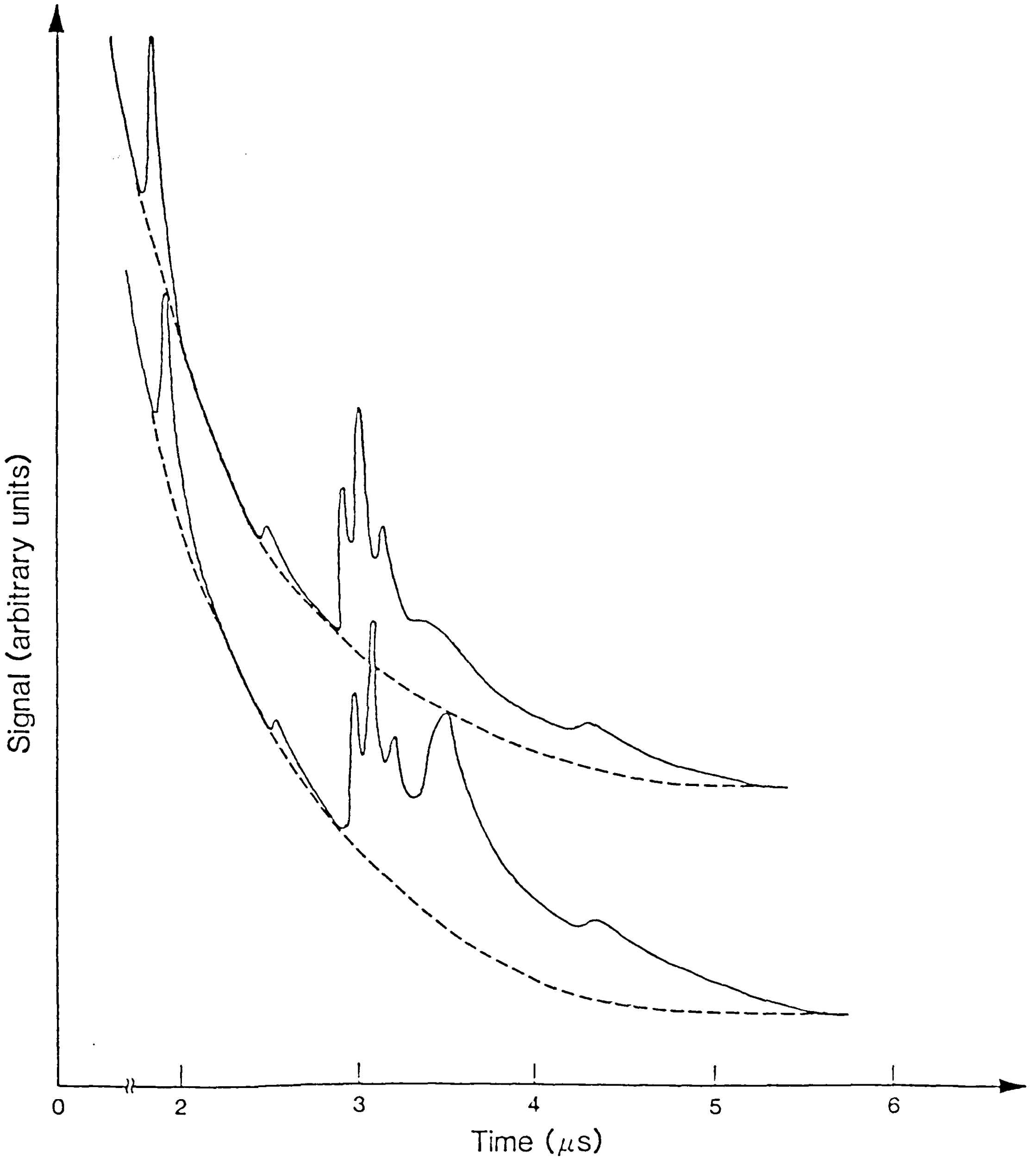

Fig. 5.6b

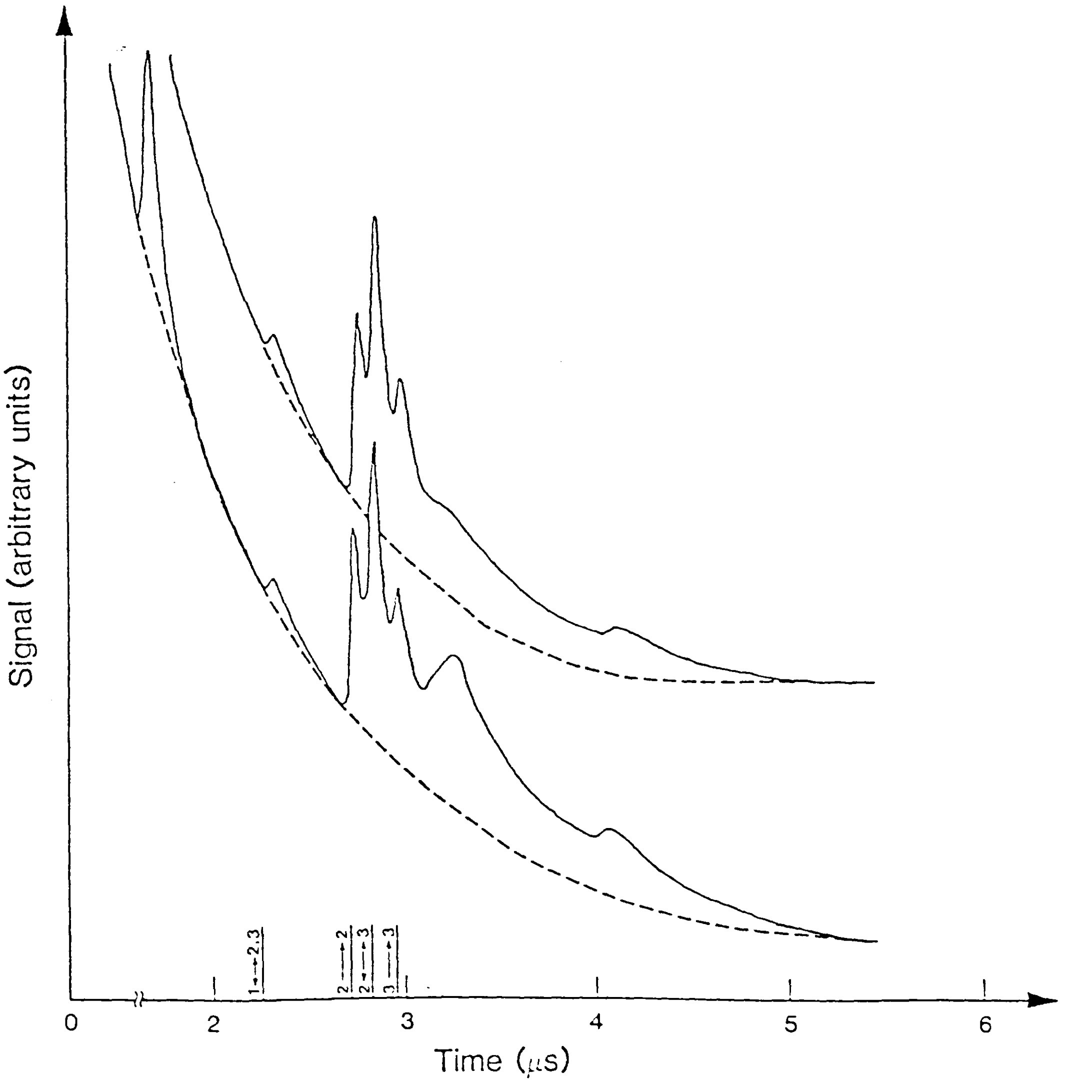

Fig. 5.7

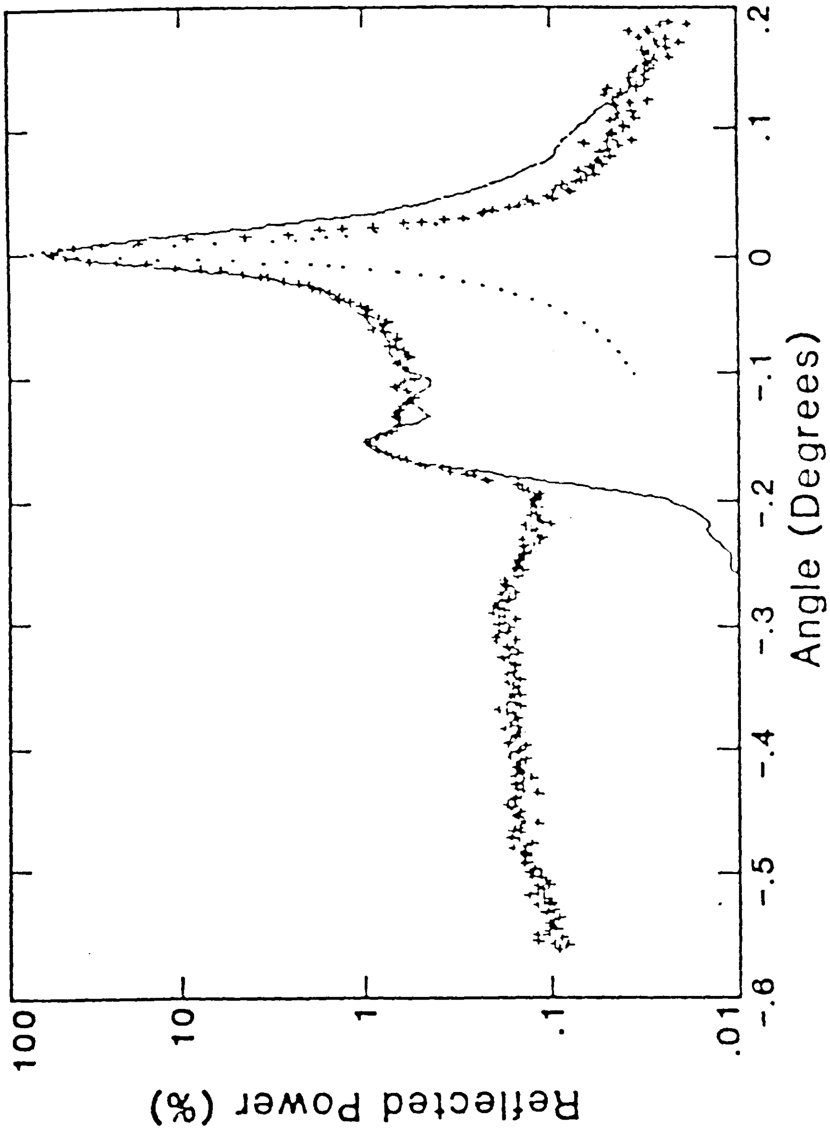

Fig. 5.8

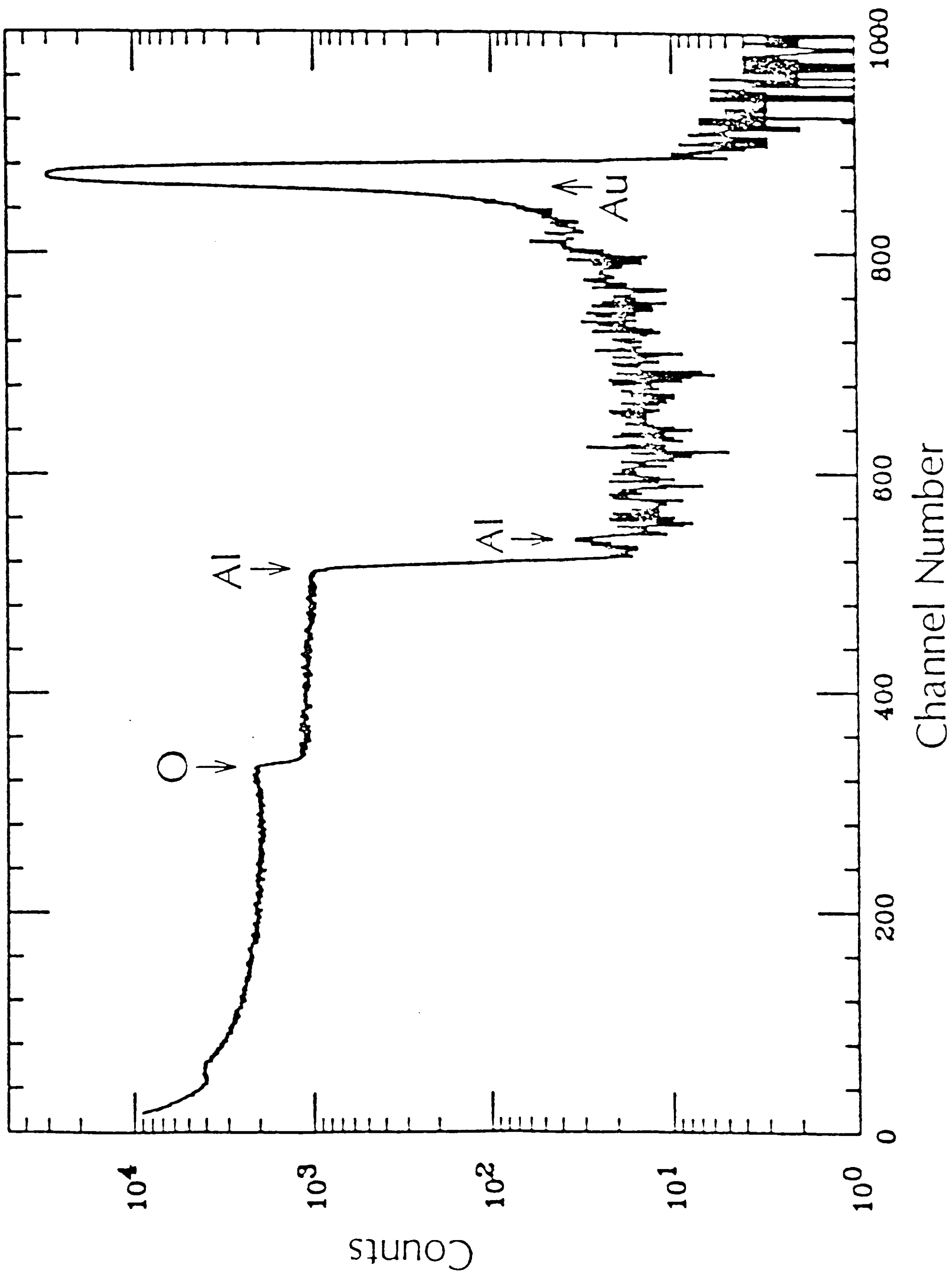
Counts
10^0
10^1
10^2
10^3
10^4
Channel Number
0
200
400
600
800
1000
O
Al
Al
Au

Fig. 5.9a

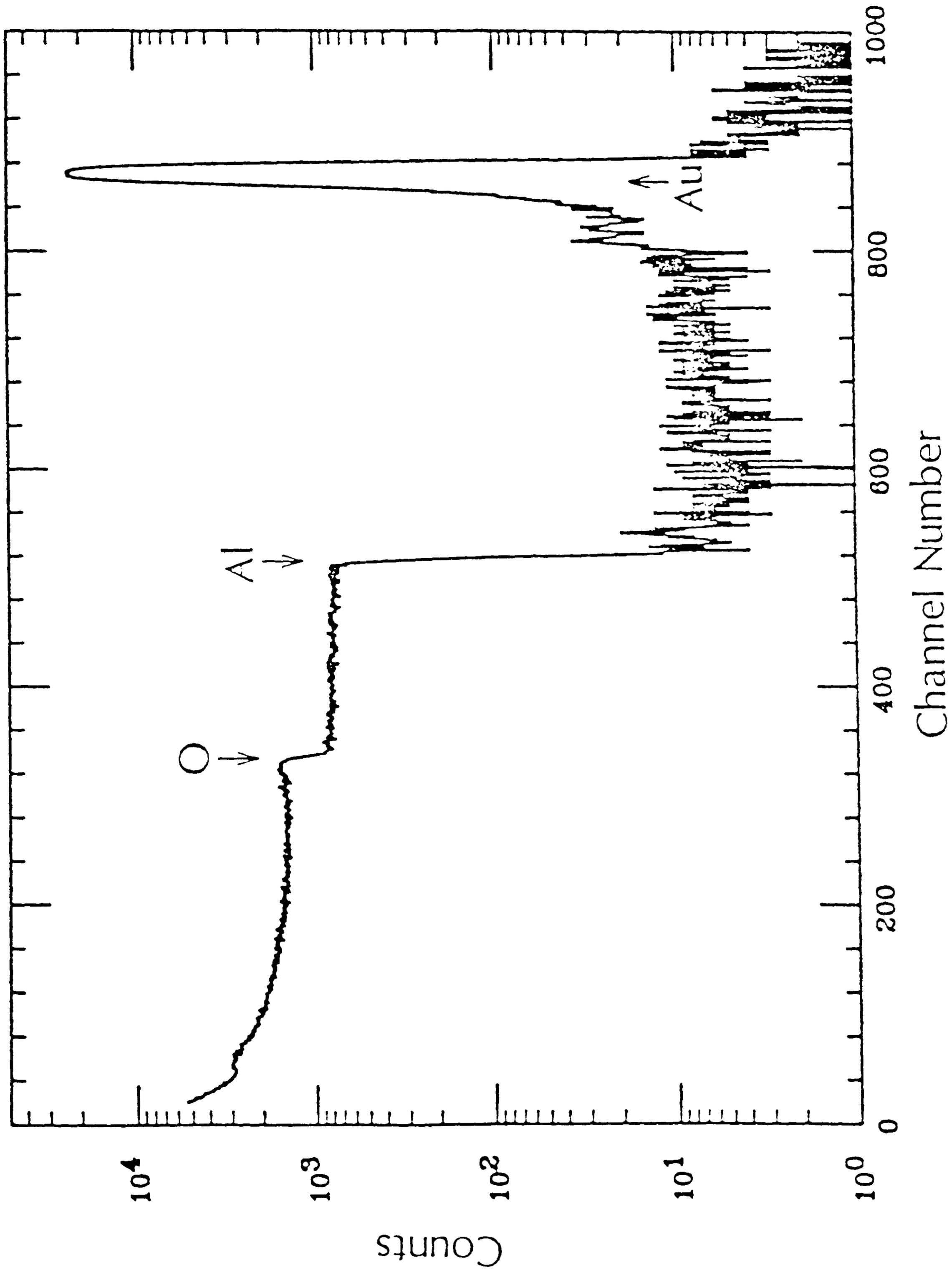
Counts
10^4
10^3
10^2
10^1
10^0
0
200
400
600
800
1000
Channel Number
O
Al
Au

Fig. 5.9b

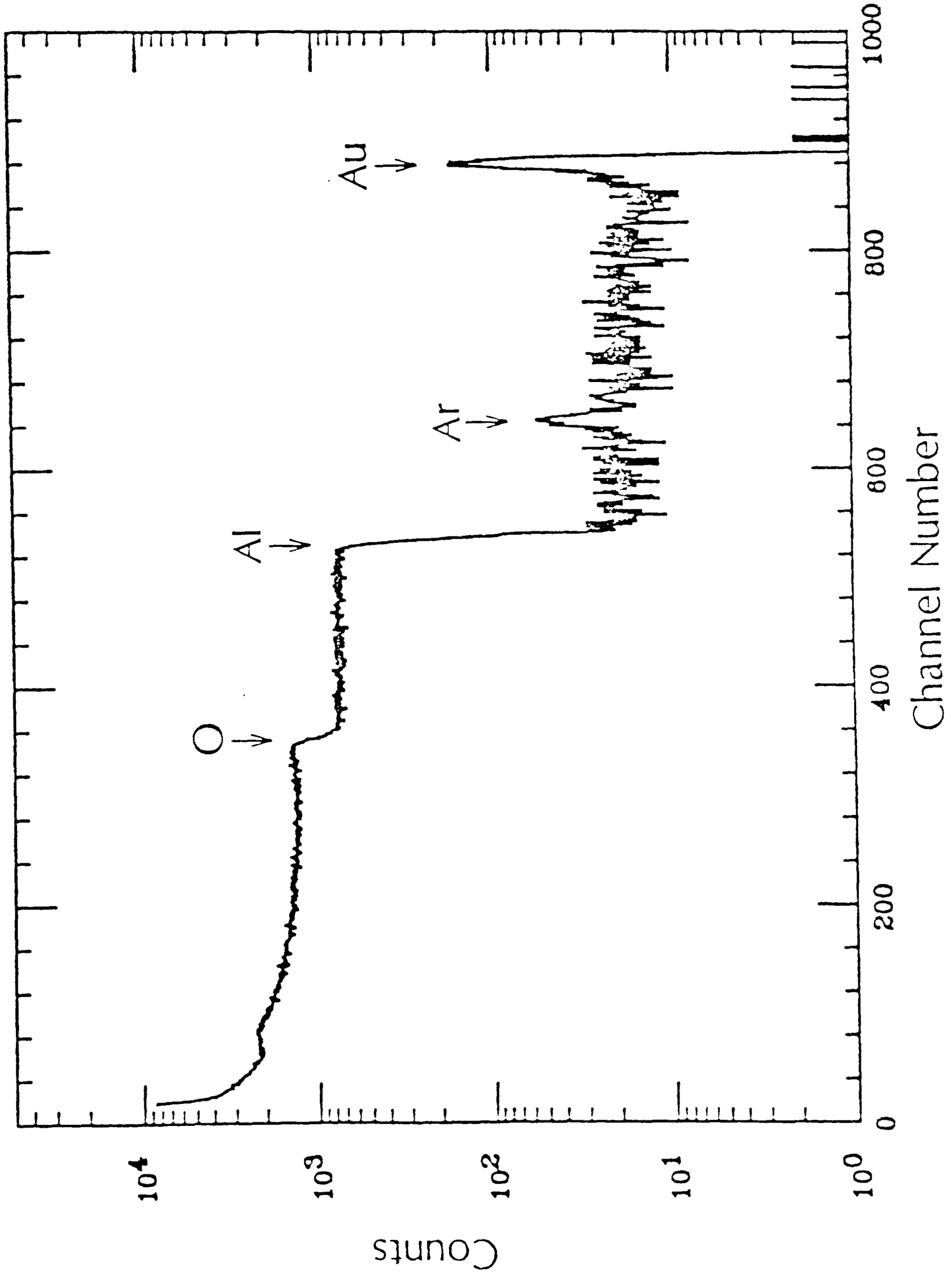
Counts
10^4
10^3
10^2
10^1
10^0
Channel Number
0
200
400
600
800
1000
O
Al
Ar
Au

Fig. 5.9c

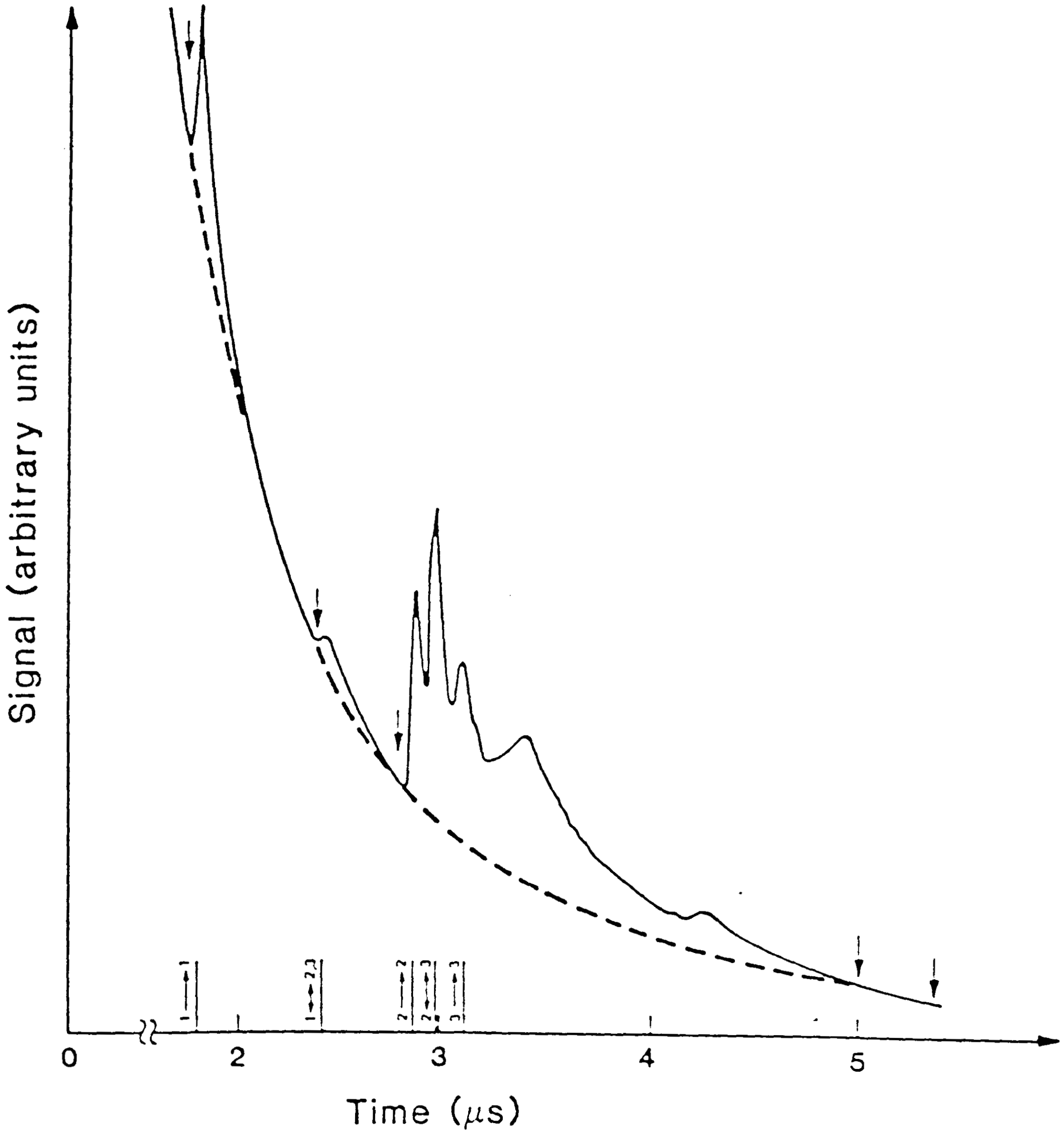

Fig. 6.1a

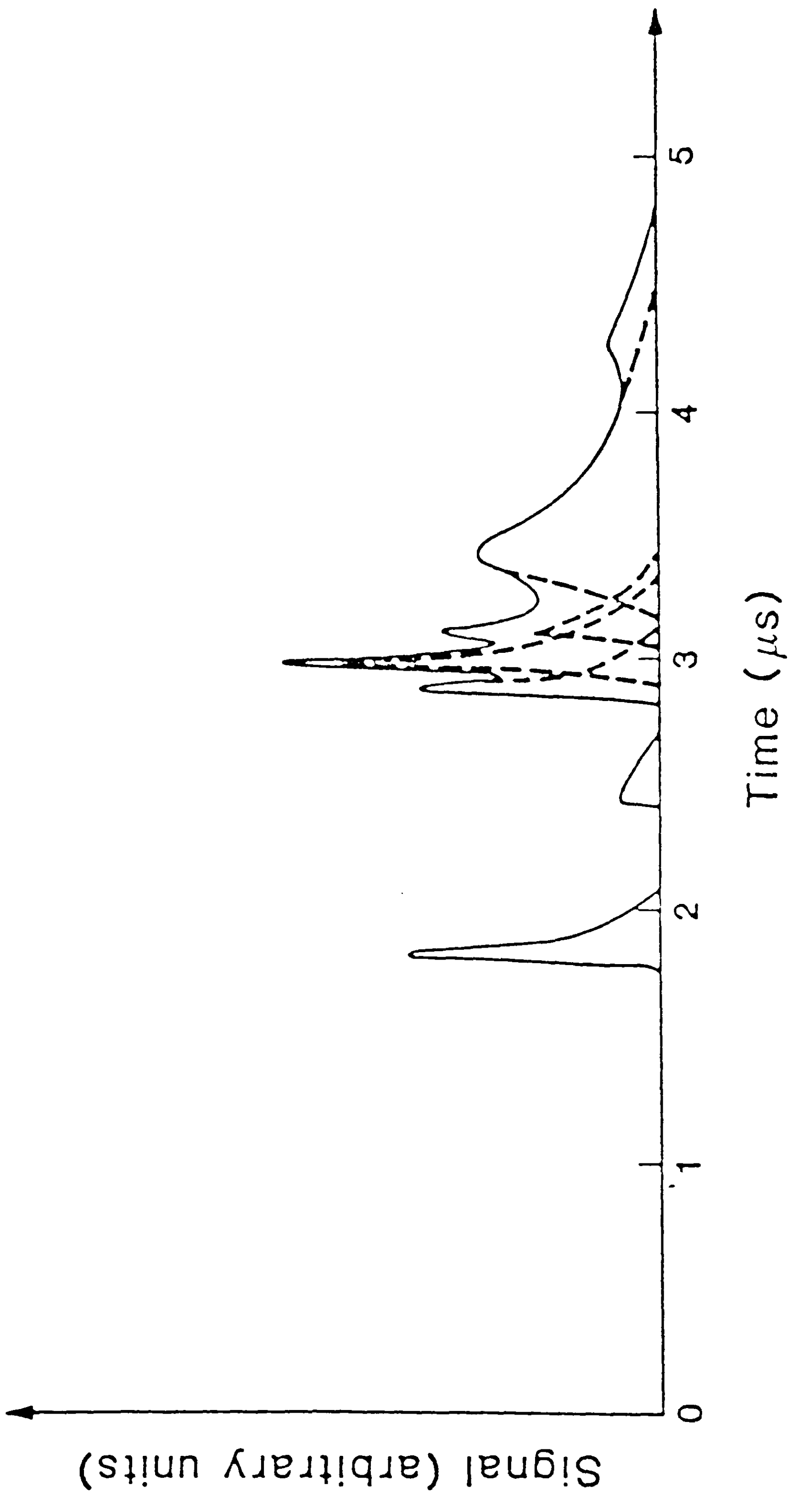

Fig. 6.1b

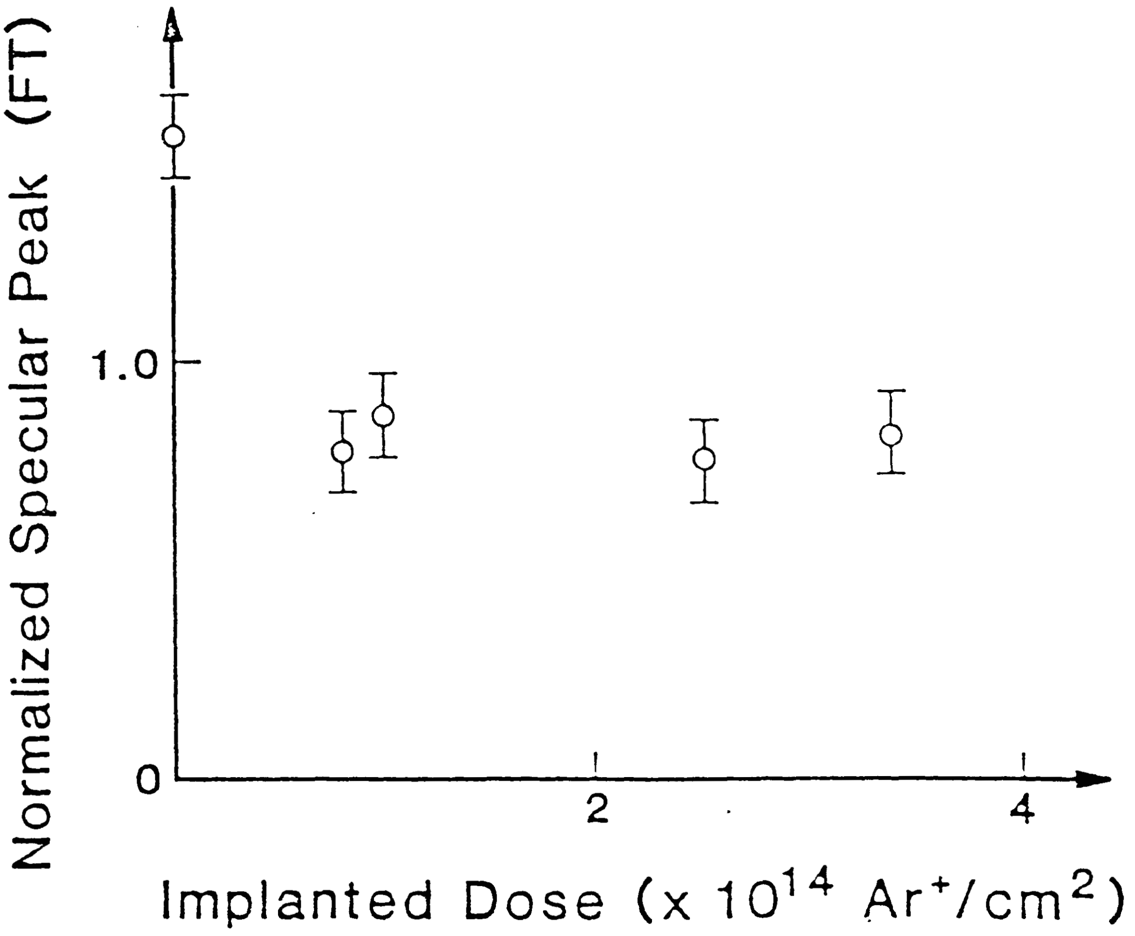
Normalized Specular Peak (FT)
1.0
0
2
4
Implanted Dose (x 10¹⁴ Ar⁺/cm²)

Fig. 6.2a

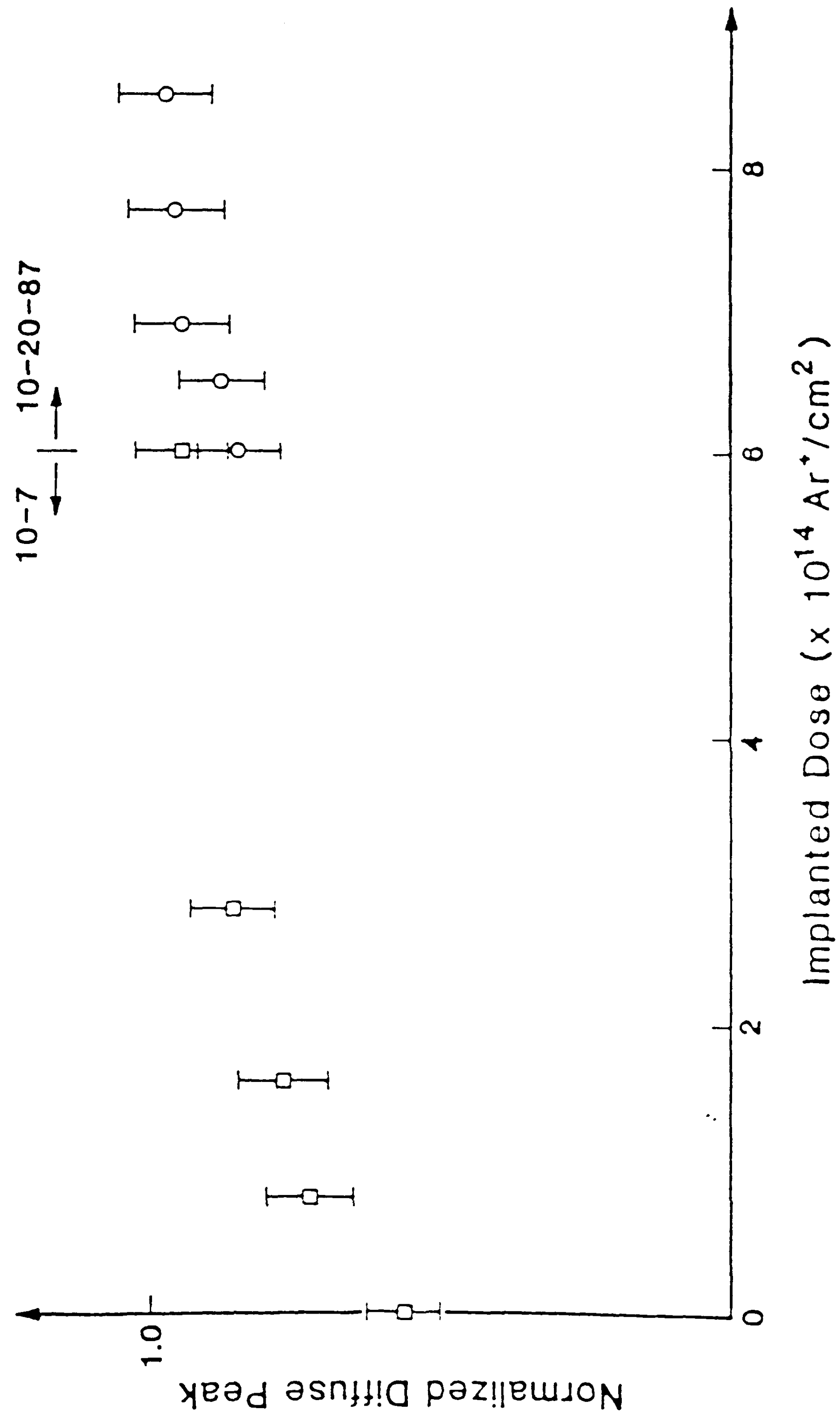
10-7
10-20-87
1.0
Normalized Diffuse Peak
0
2
4
6
8
Implanted Dose (x 10^{14} Ar$^+$/cm^2)

Fig. 6.2b

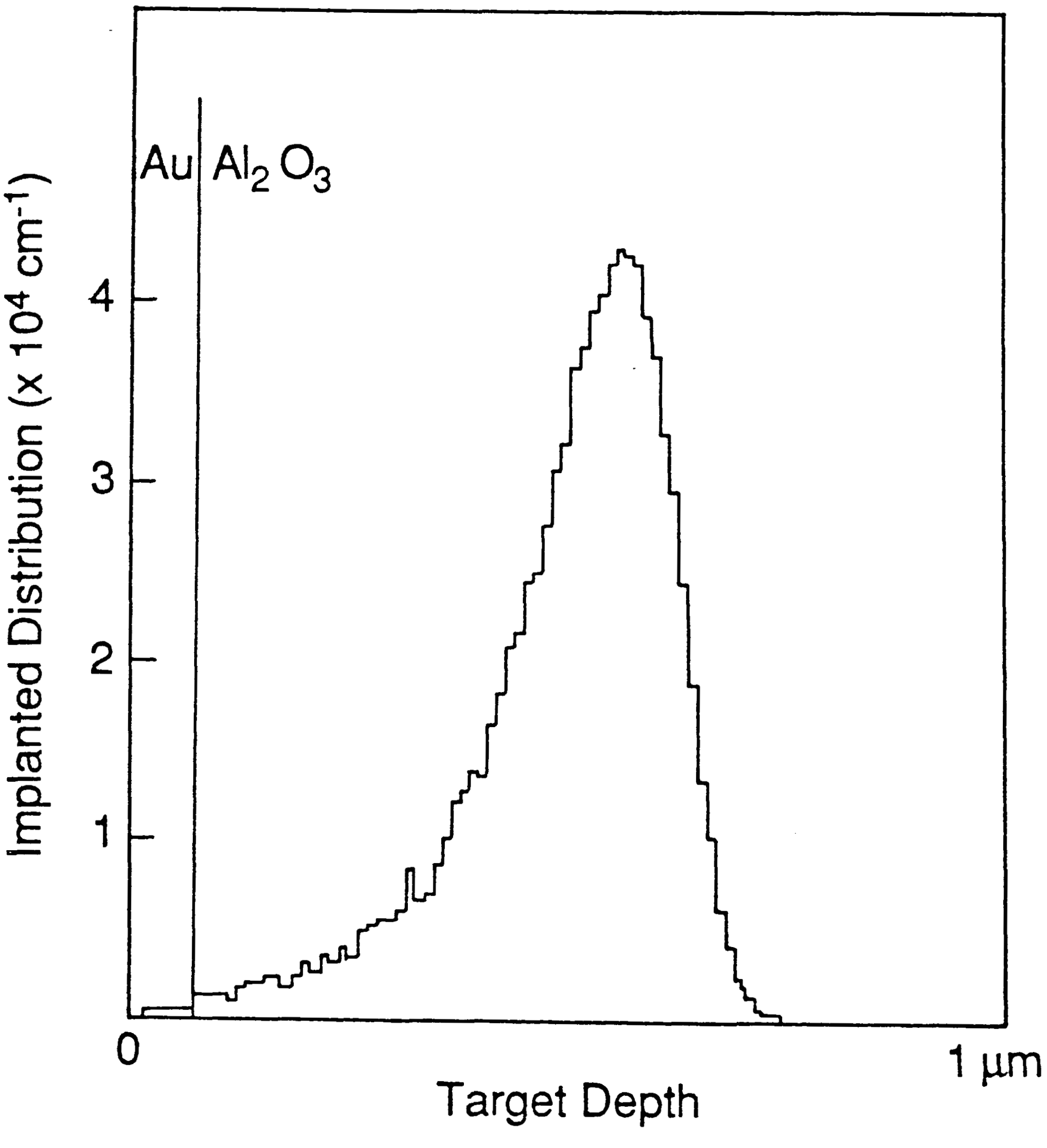
Au
Al_2O_3
Implanted Distribution (x 10^4 cm^{-1})
1
2
3
4
0
1 μm
Target Depth

Fig. 6.3a

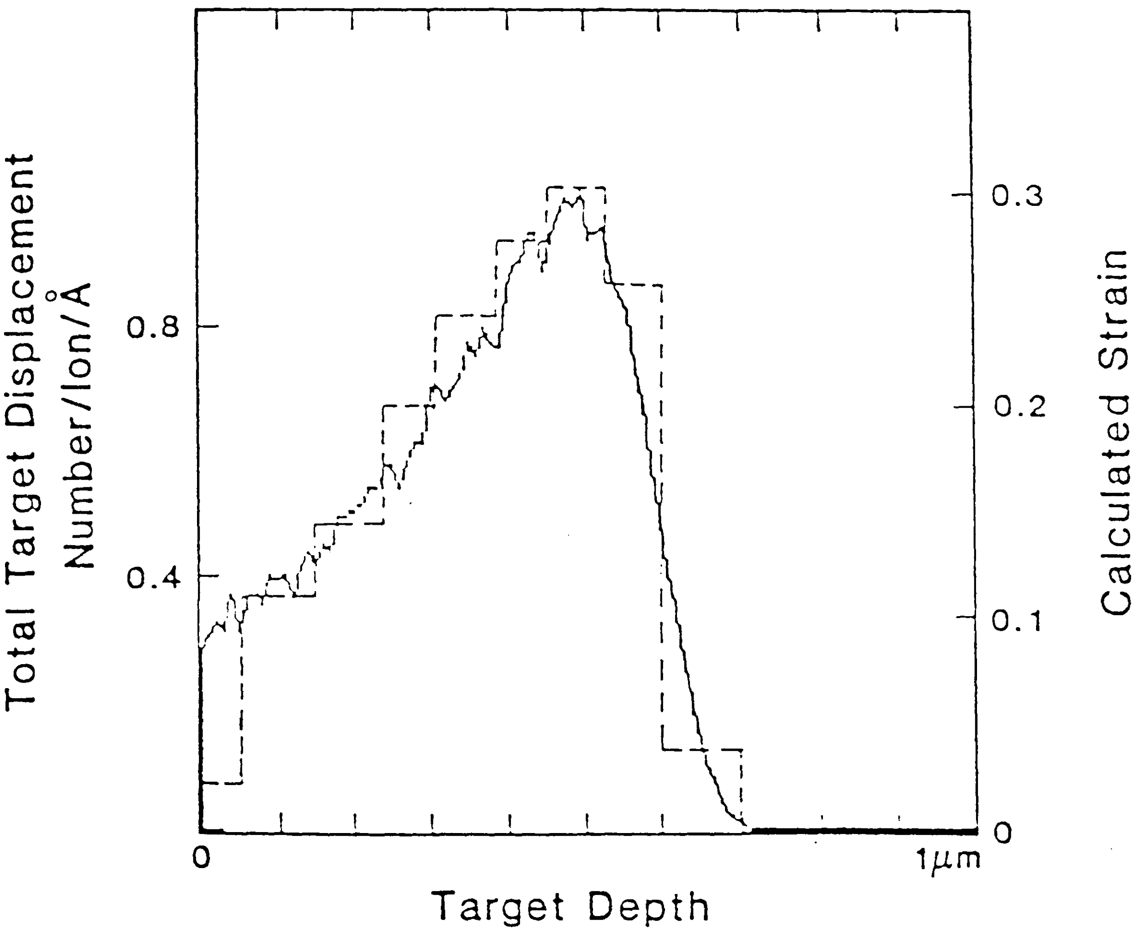
Total Target Displacement
Number/Ion/Å
0.8
0.4
0.3
0.2
0.1
0
Calculated Strain
0
1μm
Target Depth

Fig. 6.3b

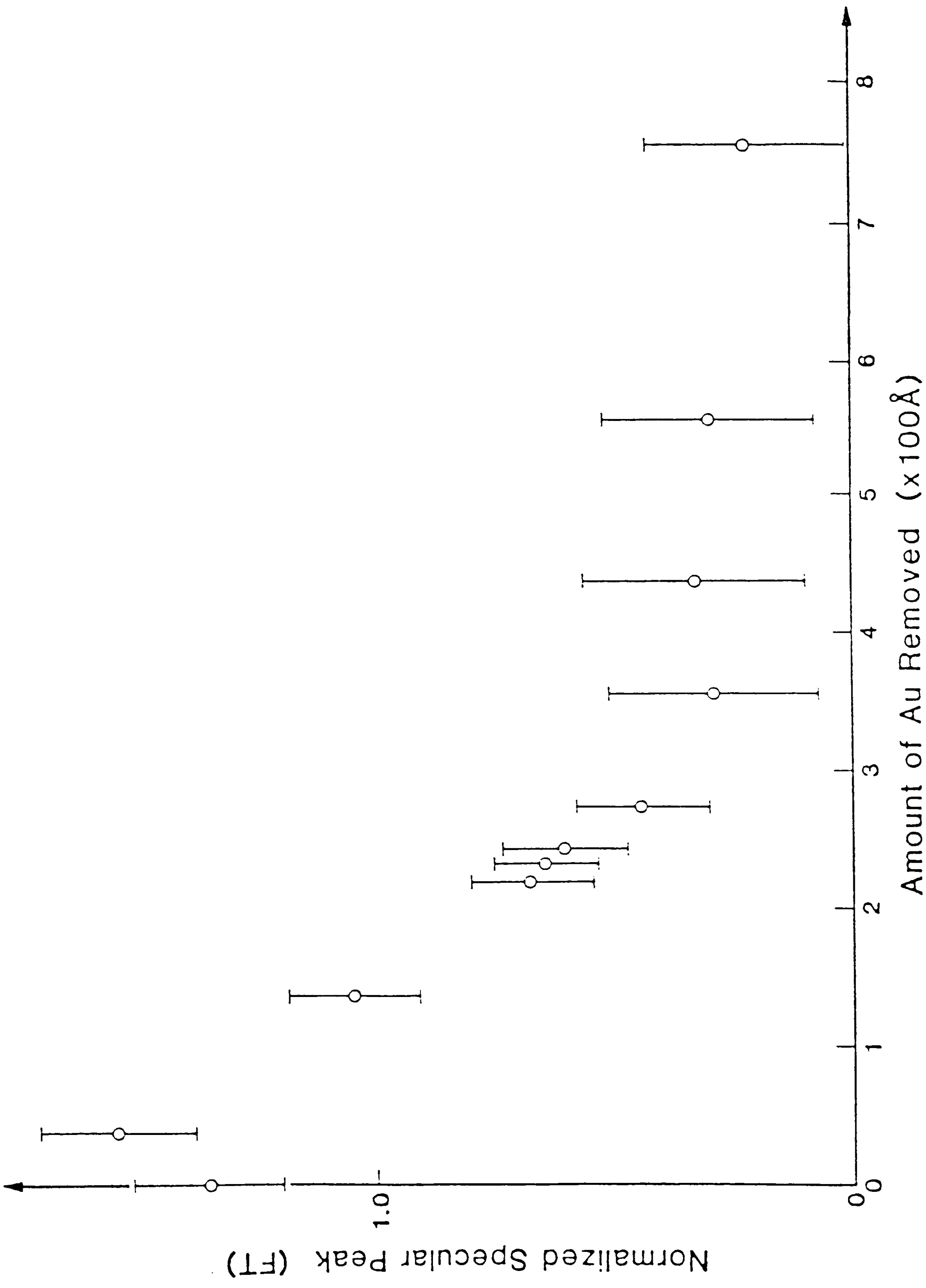
Normalized Specular Peak (FT)
1.0
0
0
1
2
3
4
5
6
7
8
Amount of Au Removed (x100Å)

Fig. 6.4a

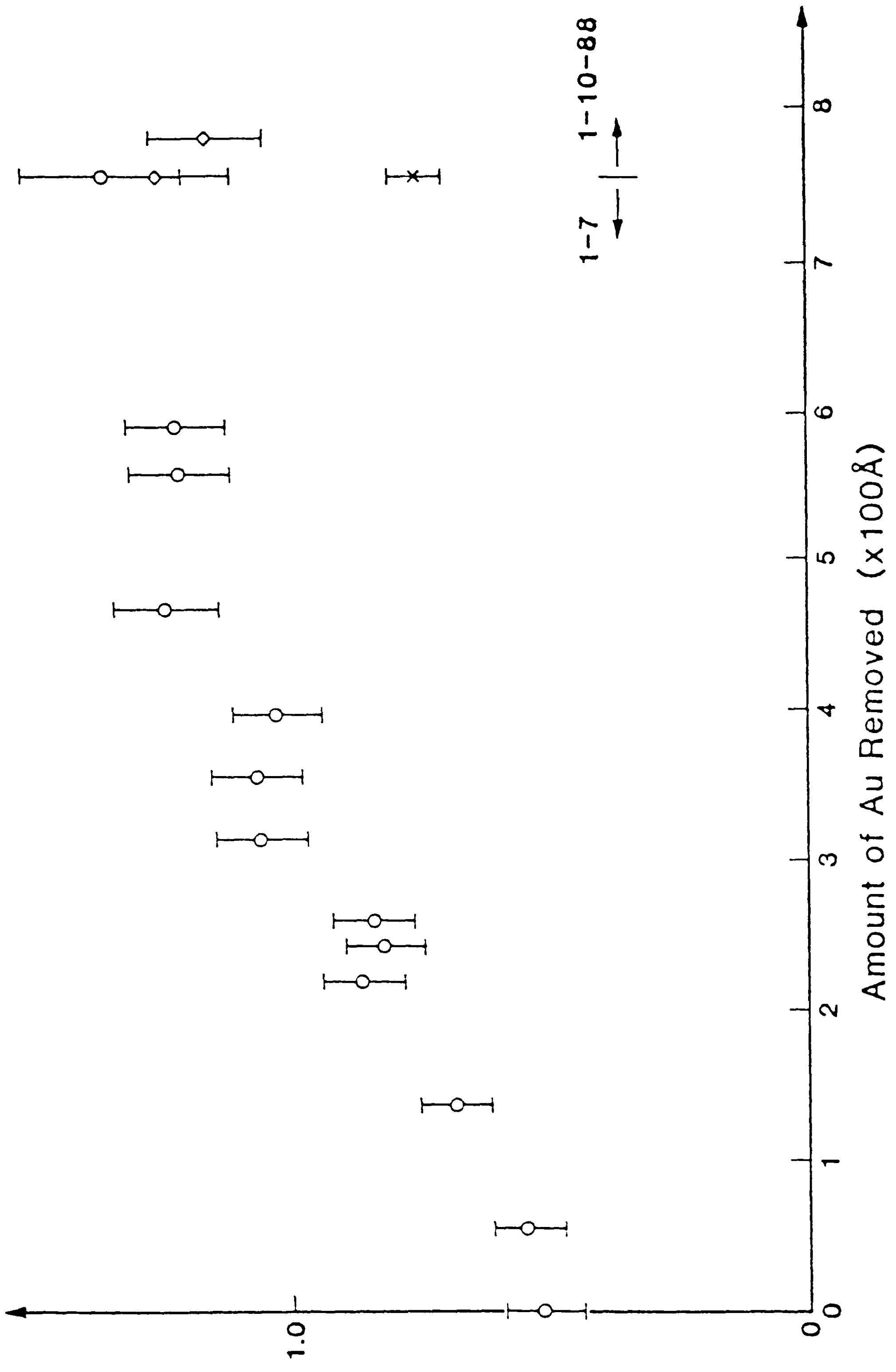
Normalized Diffuse Peak
1.0
0
0
1
2
3
4
5
6
7
8
Amount of Au Removed (x100Å)
1-7
1-10-88

Fig. 6.4b

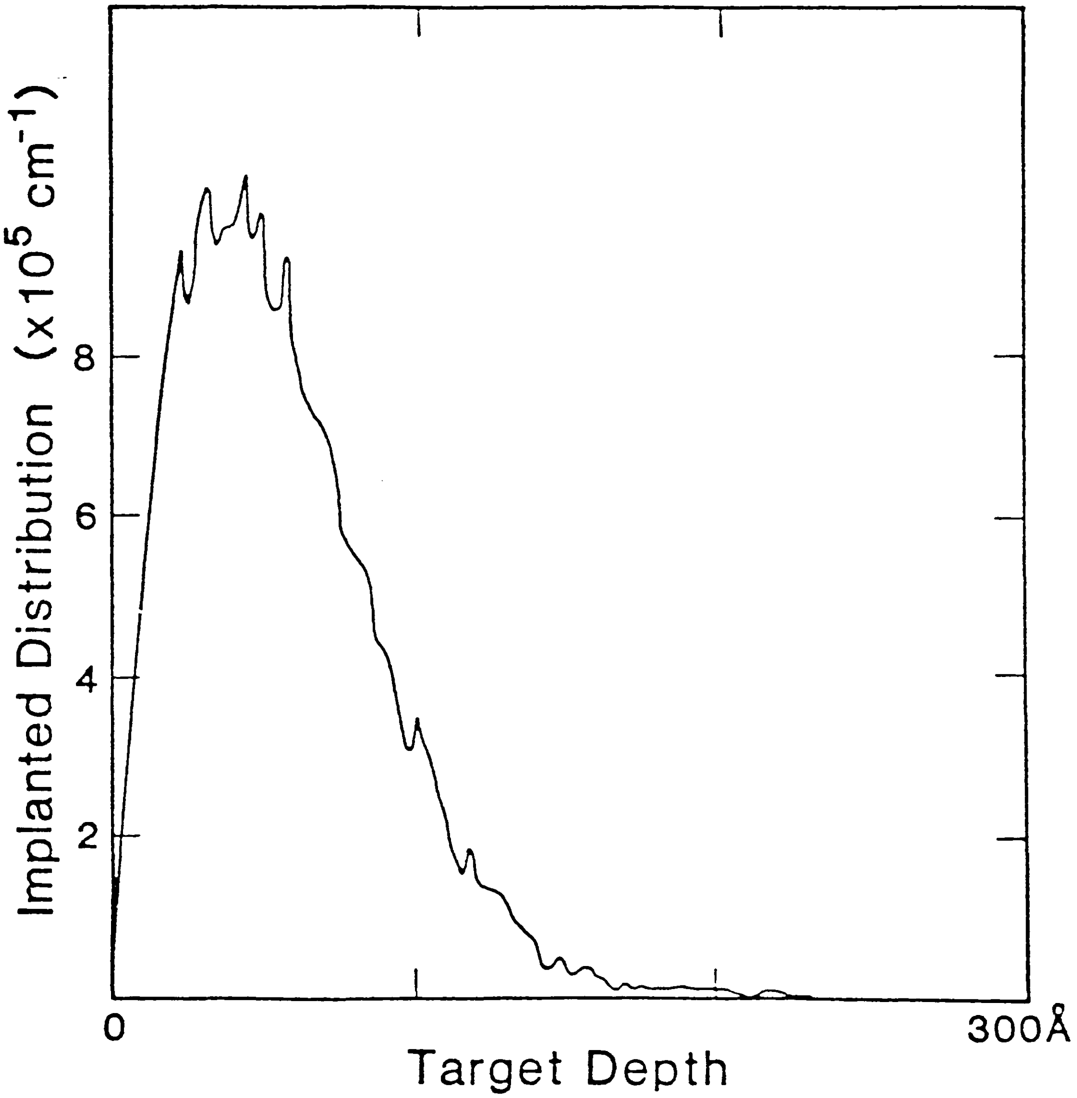

Fig. 6.5a

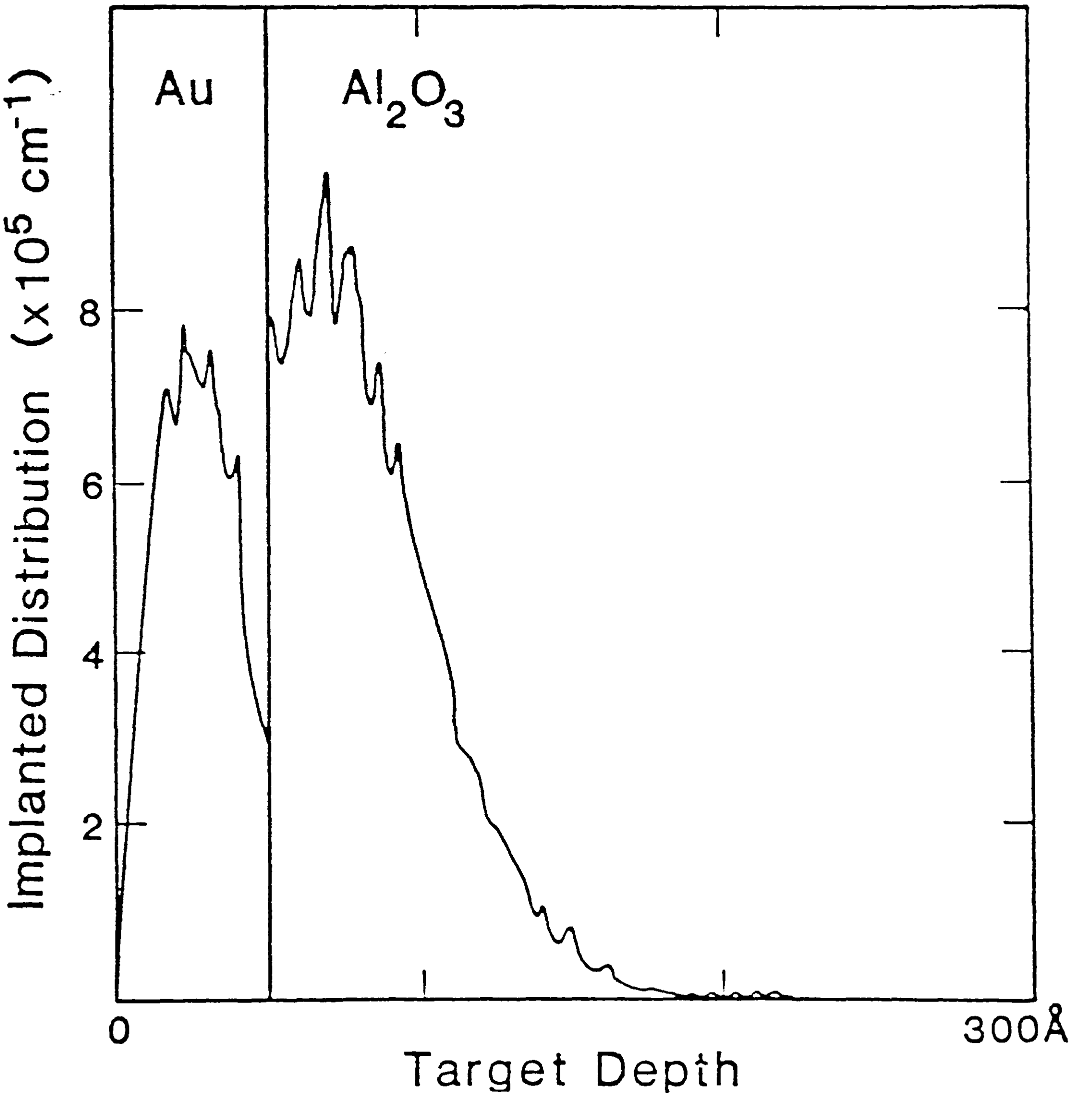
Au
Al2O3
Implanted Distribution (x10^5 cm^-1)
8
6
4
2
0
300Å
Target Depth

Fig. 6.5b

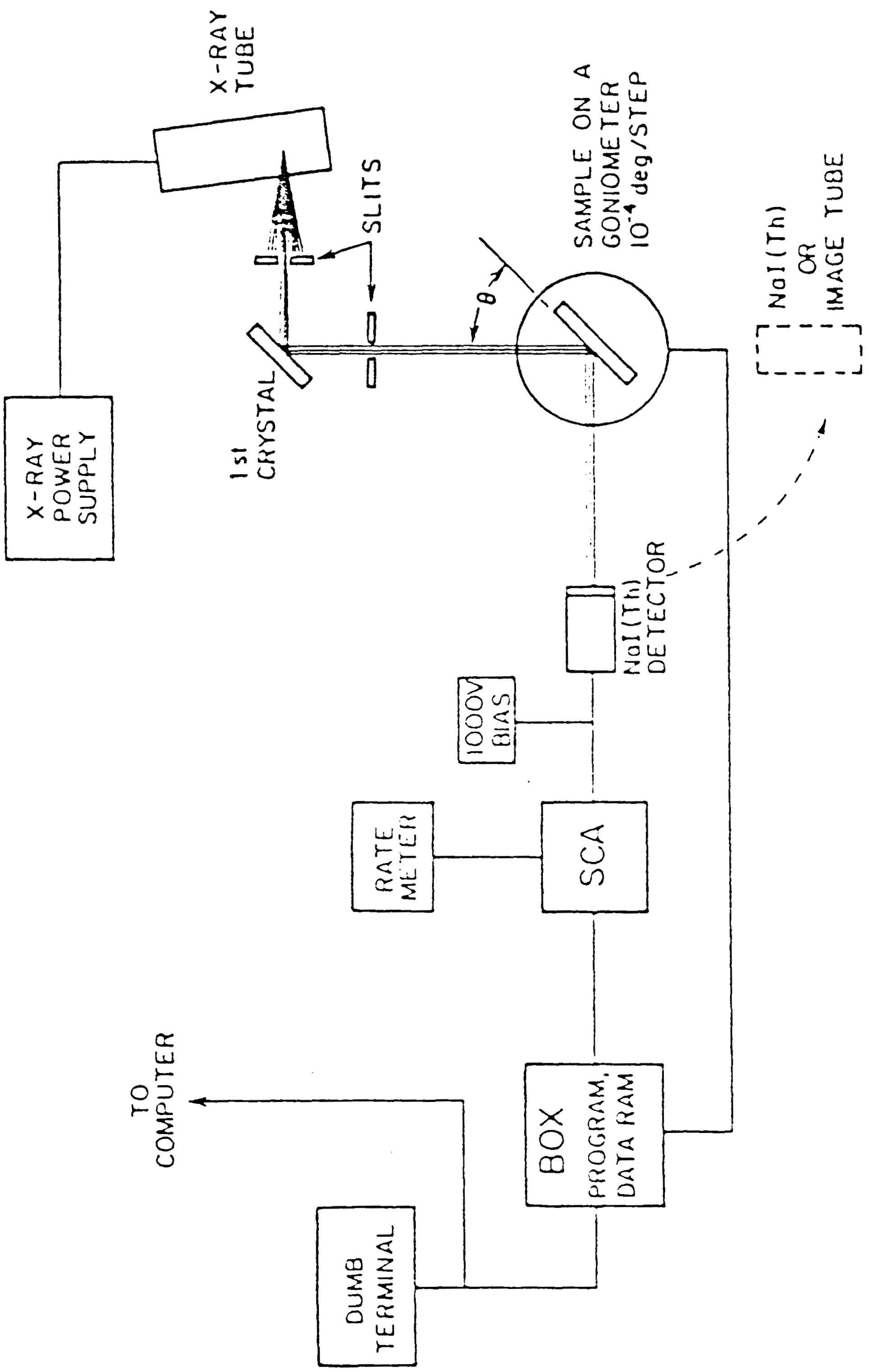
X-RAY TUBE
SLITS
SAMPLE ON A GONIOMETER 10^{-4} deg/STEP
θ
NaI(Th) OR IMAGE TUBE
1st CRYSTAL
X-RAY POWER SUPPLY
NaI(Th) DETECTOR
1000V BIAS
RATE METER
SCA
BOX PROGRAM, DATA RAM
TO COMPUTER
DUMB TERMINAL

Fig. A1.1

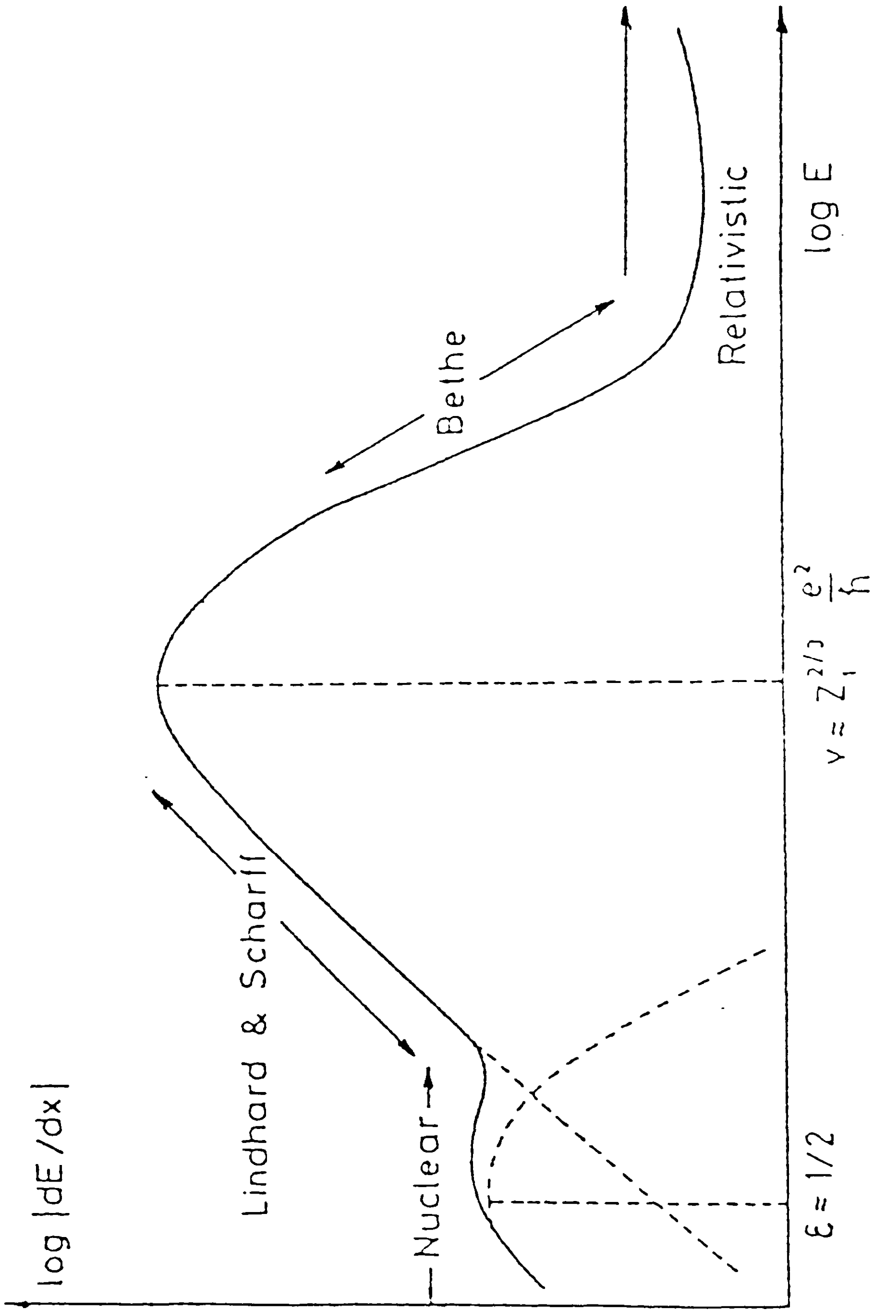
log |dE/dx|
Lindhard & Scharff
Nuclear
Bethe
Relativistic
log E
$\varepsilon = 1/2$
$v = Z_1^{2/3} \frac{e^2}{\hbar}$

Fig. A2.1

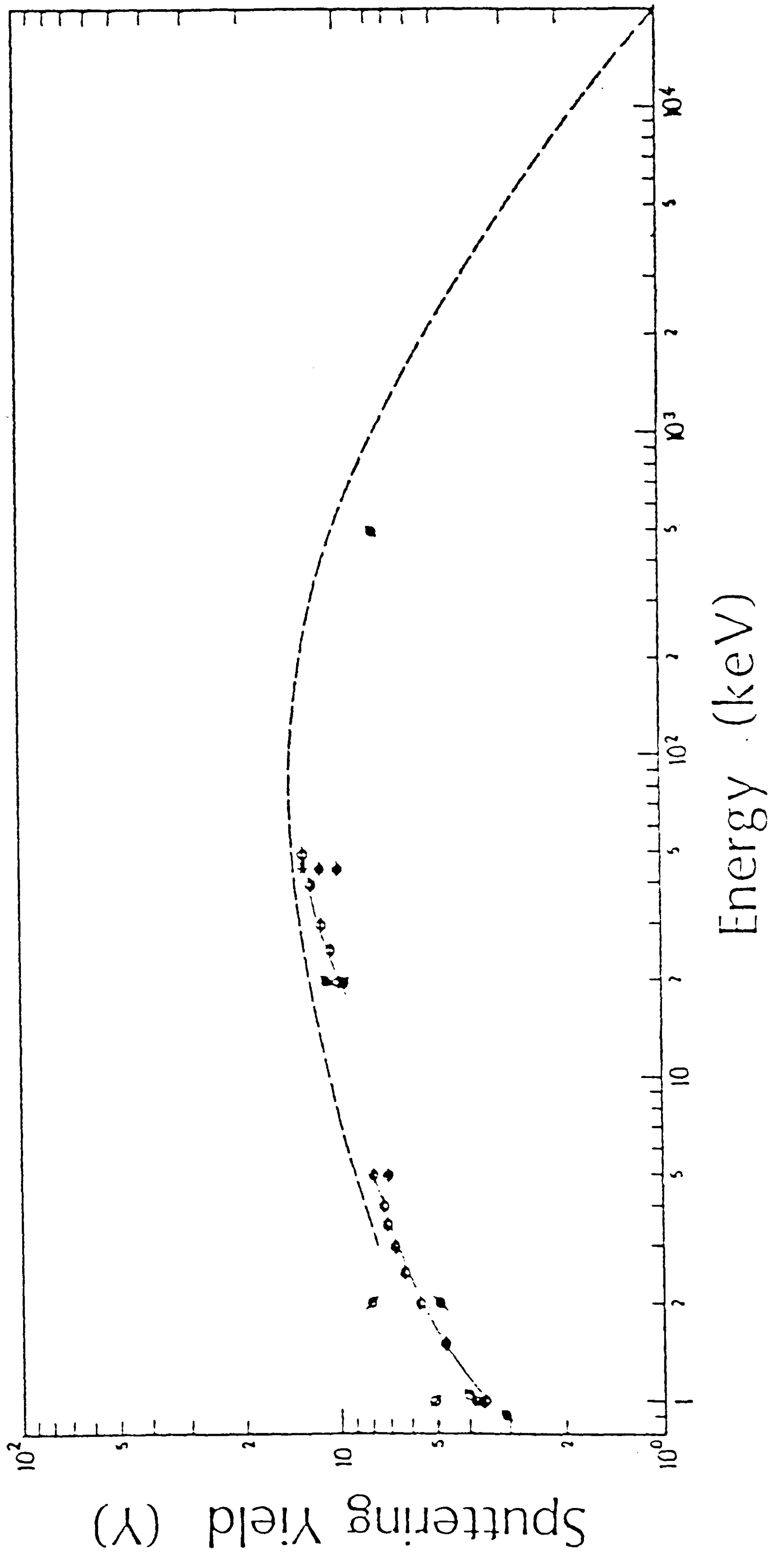
Sputtering Yield (Y)
Energy (keV)
10^0
2
5
10
2
5
10^2
1
2
5
10
2
5
10^2
2
5
10^3
2
5
10^4

Fig. A2.2

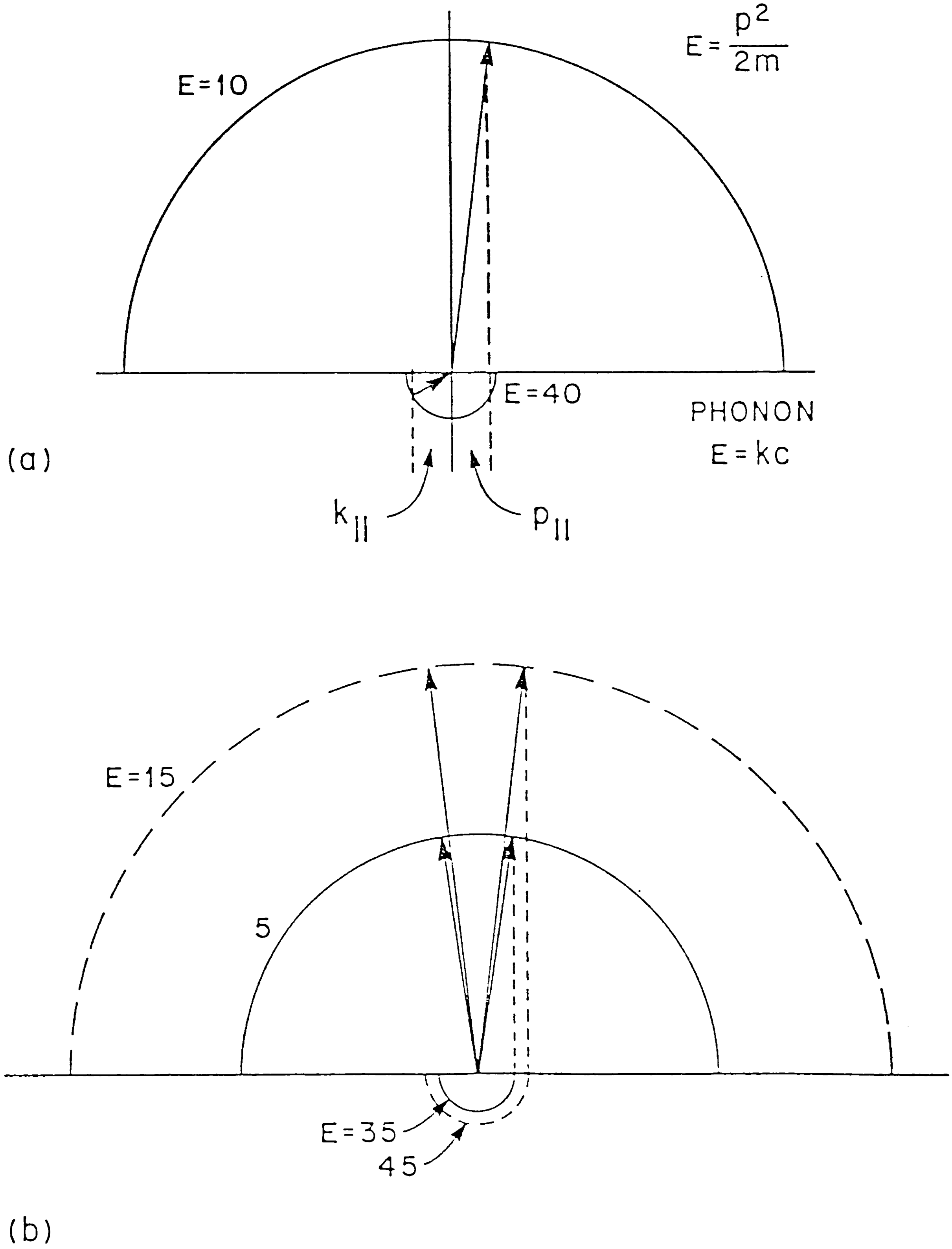

Fig. A3.1

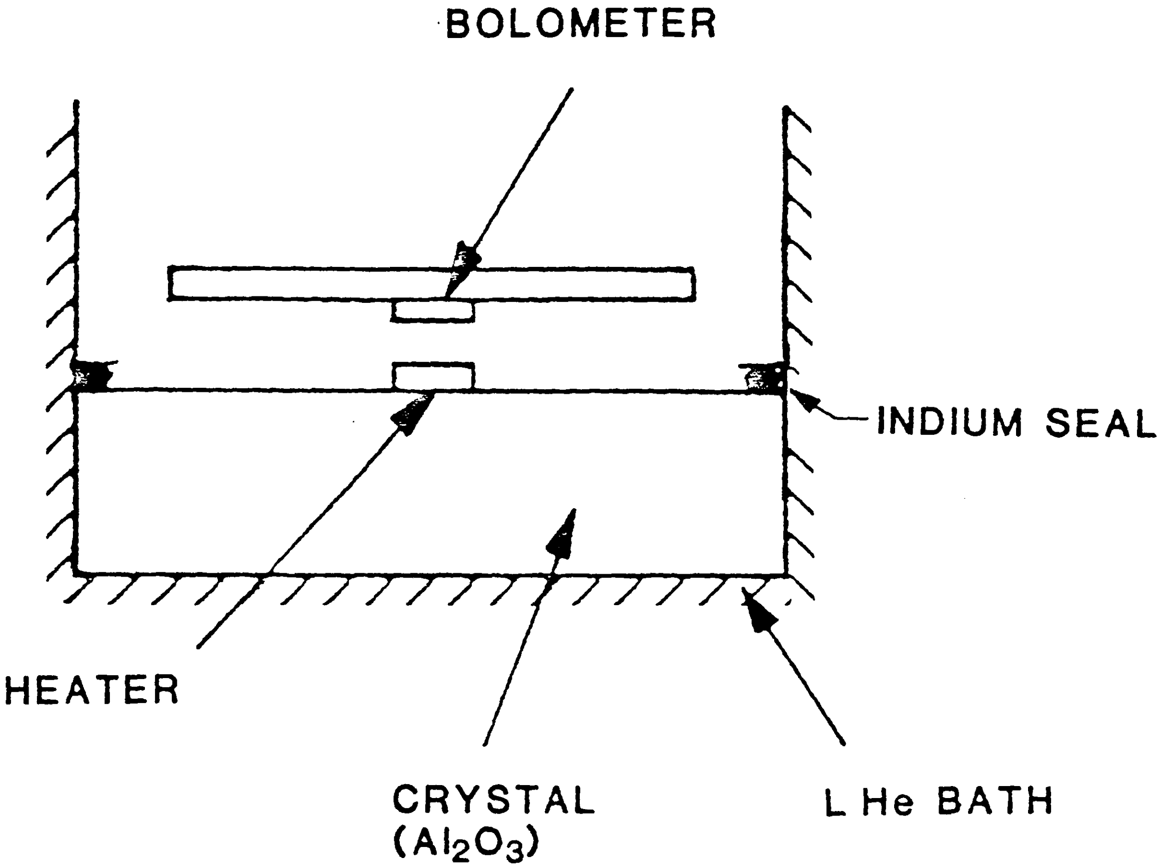

Fig. A3.2